

THE SUSI BEAM EMITTANCE COLLIMATION CHANNEL

By

Chi Zhang

A THESIS

Submitted to
Michigan State University
in partial fulfillment of the requirements
for the degree of

MASTER OF SCIENCE

Physics and Astronomy

2010

ABSTRACT

THE SUSI BEAM EMITTANCE COLLIMATION CHANNEL

By

Chi Zhang

The Superconducting Source for Ions (SuSI) is a newly designed, fully superconducting Electron Cyclotron Resonance (ECR) ion source working at 14.5 and 18 GHz microwave frequencies at the National Superconducting Cyclotron Laboratory (NSCL). Preliminary results indicate that SuSI is capable of producing ion beam currents comparable to other 18 GHz sources[1].

In parallel to the increase in beam currents offered by SuSI compared to existing sources at the NSCL, a dedicated collimation channel has been designed to tailor the beam emittances to the K500 cyclotron acceptance, which is about $75 \pi \text{ mm mrad}$ [2], so as to minimize the beam losses in the cyclotron extraction channel. The collimation channel uses four collimation stages and three solenoids in between to rotate the beam transversely in phase space. Beam simulations showed that the proposed design can efficiently collimate beams from SuSI under various scenarios. The collimation channel was commissioned with SuSI in a test area in June 2009. Experimental results have confirmed the effective collimation capability observed in the beam simulations.

The collimation channel and SuSI were moved to the Coupled Cyclotron Facility (CCF) ECR area in July 2009 in replacement of the former 6 GHz Superconducting ECR ion source (SC-ECR). Since then the collimation channel has been re-commissioned and provided adequate capability for emittance collimation and ECR parameter optimization at the CCF.

ACKNOWLEDGMENT

There are many people I would like to acknowledge for their contributions in making this thesis possible.

First, I would like to extend my greatest thank you to my advisor Marc Doleans for his immeasurable guidance and support throughout my three years study and research at NSCL. The experience of working with Marc will be precious to me for my lifetime.

I would like to thank Felix Marti and Remco Zegers, who kindly joined my committee and provided me invaluable comments to this thesis. I would like to thank people in the ECR group, especially Dallas Cole, Guillaume Machicoane, Liangting Sun and Larry Tobos for their tireless assistance on the ion source and measurement instruments during the experiment. I would also like to thank Carla Benatti for helping me fine tune the thesis in the last minute.

In the end, I would like to thank my parents and my sister for their encouragement and support from the other side of the earth, and especially, Miss Yingyun Ma, who loves me, cares me, and always accompanies me. Without her, the road to where I am today would have been much tougher.

TABLE OF CONTENTS

List of Tables	vi
List of Figures	vii
1 INTRODUCTION	1
1.1 National Superconducting Cyclotron Laboratory (NSCL)	1
1.1.1 Coupled Cyclotron Facility (CCF)	1
1.1.2 Facility for Rare Isotope Beams (FRIB)	3
1.2 Background Information	6
1.2.1 Electron Cyclotron Resonance (ECR) Ion Source	6
1.2.2 Beam Dynamics Basics	8
Transfer Matrix and Beam Transport	8
Beam Emittance	11
1.3 Superconducting Source for Ions (SuSI)	19
1.4 Need For Emittance Collimation	21
2 EMITTANCE COLLIMATION CHANNEL DESIGN	28
2.1 Basic Principle	28
2.2 Collimation Channel Parameters	31
2.3 Beam Simulation	32
2.3.1 Verification of Basic Functionality	32
2.3.2 Tuning Recipe	40
2.3.3 Flexibility of Channel Design For Mismatched Beams	41
3 EMITTANCE COLLIMATION CHANNEL IMPLEMENTATION	44
3.1 Hardware Description	44
3.1.1 Solenoid	44
3.1.2 Steering Magnet	45
3.1.3 4-Jaw Slit System	46
3.1.4 Circular Aperture	51
3.1.5 Beam Diagnostics	51
Faraday Cup	51
Beam Viewer Plates	53
Allison Emittance Scanner	53
Beam Diagnostics Box	57
4 EMITTANCE COLLIMATION CHANNEL INSTALLATION AND COMMISSIONING	58
4.1 Hardware Installation	58

4.1.1	Project Phase	58
	Phase I: Commissioning In SuSI Test Area	58
	Phase II: Re-Commissioning In CCF ECR Area	59
4.1.2	Alignment of Components	59
	Alignment of the Laser	59
	Preliminary Alignment of the Middle Solenoid	63
	Preliminary Alignment of Outer Solenoids	64
	Alignment of the 6 Way Diagnostic Box	64
	Final Beam Based Alignment of the Solenoids	66
4.2	Software For Commissioning	66
4.2.1	Beam Viewer Application (BVA)	66
4.2.2	Trace 3D	69
4.2.3	Allison Emittance Scanner	69
	Labview Interface	72
	Post Processor	72
4.3	Beam Experiment	74
4.3.1	Steering Magnet Calibration	74
4.3.2	Solenoid Modeling	77
4.3.3	Experimental Test of Solenoid Model	85
4.3.4	Beam Collimation Process	86
	Typical Tuning Procedure	86
	Argon Beam Result	89
	Krypton Beam Result	89
4.3.5	Emittance Collimation Channel For ECR Tuning	100
	Motivation	100
	Example	100
5	CONCLUSION	105
	Bibliography	107

LIST OF TABLES

3.1	Basic parameters of the solenoid used in SuSI collimation beam line .	45
4.1	Best result for the two field level cases	81
4.2	Summary of the two equivalent solenoid models.	82

LIST OF FIGURES

Images in this thesis are presented in color

1.1	Current Layout of NSCL	2
1.2	Proposed layout of FRIB	4
1.3	Conceptual schematic design of FRIB	5
1.4	Basic layout of ECR ion source	7
1.5	An example of ECR resonance surface of ARTEMIS-B	9
1.6	Natural reference coordinate system.	9
1.7	A system transporting particles through N elements.	11
1.8	Geometric meaning of Twiss parameters	15
1.9	Example of emittance filamentation	17
1.10	Geometric representation of the rms ellipse	18
1.11	A cross-sectional view of SuSI	20
1.12	Images for different charge states of a Krypton beam on a beam viewer after the selecting magnet.	24
1.13	Transverse emittances for $^{84}\text{Kr}^{9+}$	25
1.14	Transverse emittances for $^{84}\text{Kr}^{13+}$	26

1.15	Transverse emittances for $^{84}\text{Kr}^{17+}$	27
2.1	Illustration of the designed collimation channel	32
2.2	90 degree xy space rotation of the channel	33
2.3	Emittances in xx' and yy' phase spaces through the collimation channel	34
2.4	Overall 115 degree phase advance of the channel	36
2.5	Particle tracking through the collimation channel	37
2.6	RMS normalized emittances through the collimation channel illustrating the four cuts	38
2.7	RMS emittances and normalized brightness at the end of the collimation channel with different apertures	39
2.8	Channel tuning recipe	40
2.9	RMS emittances and normalized brightness calculated for $^{40}\text{Ar}^{7+}$ beams injected with different α	42
2.10	RMS emittances and normalized brightness calculated for $^{40}\text{Ar}^{7+}$ beams injected with different β	43
3.1	Engineering model and photo of solenoid	45
3.2	Engineering model of the steering magnet.	46
3.3	4-Jaw slits system with faraday cup.	47
3.4	Local control box, one for each jaw of the 4-Jaw slits system, installed on the beam line railing.	48
3.5	Example of the current distribution of the beam measured by the 4-Jaw slit system	49
3.6	Example of the 4D phase space scan by the 4-Jaw slit systems	50
3.7	Isometric and cross-sectional view of the aperture system	52
3.8	Engineering model of the faraday cup	53

3.9	Picture of a beam viewer plate, where dots of 20 mm separation can be seen as well.	54
3.10	Scheme of the Allison emittance scanner box	55
3.11	Mechanical drawing of the Allison emittance scanner	55
3.12	Local control box of the Allison emittance scanner installed on the beam line railing.	56
3.13	Picture of the 6 way and 8 way diagnostic box with instruments installed	57
4.1	Engineering model of the collimation channel installed in SuSI test area.	60
4.2	Engineering model of the collimation channel installed in the CCF ECR area with achromatic transport beamline.	61
4.3	The laser was positioned behind the analyzing magnet	62
4.4	Alignment of the laser	63
4.5	Alignment target mounted on the entrance and exit flanges of the middle solenoid with aperture systems connected	64
4.6	Alignment target mounted on the entrance flange of the first solenoid and the exit flange of the last solenoid	65
4.7	Alignment target mounted on the entrance and exit flanges of the 6 way diagnostics box connected to the first solenoid	65
4.8	Beam based alignment of the first solenoid	67
4.9	Basic image acquisition scheme of Beam Viewer Application.	68
4.10	Layout of Beam Viewer Application	70
4.11	An example of beam simulation using Trace3D.	71
4.12	Labview interface of the Allison emittance scanner.	73
4.13	Image of emittance scan generated by Post Processor	74
4.14	Result of steering magnet calibration	76

4.15 Solenoid field region set up in POISSON	78
4.16 Solenoid equivalent model simulation beamline set up.	83
4.17 Field profile from POISSON and equivalent hard-edge solenoid model	84
4.18 Checking solenoid xy rotation with a vertical slice of beam	85
4.19 Checking solenoid xy rotation with a horizontal slice of beam	86
4.20 Response curves of solenoid compared with simulations	87
4.21 Emittances of the $^{40}\text{Ar}^{7+}$ beam measured with $625\pi\text{-mm}\cdot\text{mrad}$ channel acceptance	90
4.22 Emittances of the $^{40}\text{Ar}^{7+}$ beam measured with $156\pi\text{-mm}\cdot\text{mrad}$ channel acceptance	91
4.23 Emittances of the $^{40}\text{Ar}^{7+}$ beam measured with $56\pi\text{-mm}\cdot\text{mrad}$ channel acceptance	92
4.24 Emittances of the $^{40}\text{Ar}^{7+}$ beam measured with $25\pi\text{-mm}\cdot\text{mrad}$ channel acceptance	93
4.25 Beam brightness of $^{40}\text{Ar}^{7+}$ at the end of the collimation channel with different channel acceptances	94
4.26 Emittances of the $^{84}\text{Kr}^{14+}$ beam measured with $625\pi\text{-mm}\cdot\text{mrad}$ channel acceptance	95
4.27 Emittances of the $^{84}\text{Kr}^{14+}$ beam measured with $156\pi\text{-mm}\cdot\text{mrad}$ channel acceptance	96
4.28 Emittances of the $^{84}\text{Kr}^{14+}$ beam measured with $56\pi\text{-mm}\cdot\text{mrad}$ channel acceptance	97
4.29 Emittances of the $^{84}\text{Kr}^{14+}$ beam measured with $25\pi\text{-mm}\cdot\text{mrad}$ channel acceptance	98
4.30 Beam brightness of $^{84}\text{Kr}^{14+}$ at the end of the collimation channel with different channel acceptances	99
4.31 Emittances of the $^{84}\text{Kr}^{10+}$ beam measured with $625\pi\text{-mm}\cdot\text{mrad}$ channel acceptance	101

4.32	Emittances of the $^{84}\text{Kr}^{10+}$ beam measured with 56 π -mm-mrad channel acceptance	102
4.33	Measurement of current of $^{40}\text{Ar}^{7+}$ beam at end of collimation with different baffle positions	104

Chapter 1

INTRODUCTION

1.1 National Superconducting Cyclotron Laboratory (NSCL)

The National Superconducting Cyclotron Laboratory (NSCL) is a world leader in rare isotope research located on the campus of Michigan State University (MSU).

1.1.1 Coupled Cyclotron Facility (CCF)

Currently NSCL operates two cyclotrons, the K500 and K1200 cyclotrons. The K500 cyclotron was the world's first cyclotron using superconducting technology[3], and the K1200 cyclotron is the highest-energy continuous beam accelerator in the nation, and can provide ion beams with energy up to 200 MeV per nucleon[4]. In 2001, the two stand-alone cyclotrons were configured as the Coupled Cyclotron Facility (CCF) with the K500 used as the injector to the K1200[5], and since then the injection beam line optics has been further optimized to improve the efficiency of the facility[6]. A full list of the primary beams available at the CCF can be found on the NSCL website[7]. The current layout of NSCL is shown in Figure 1.1.

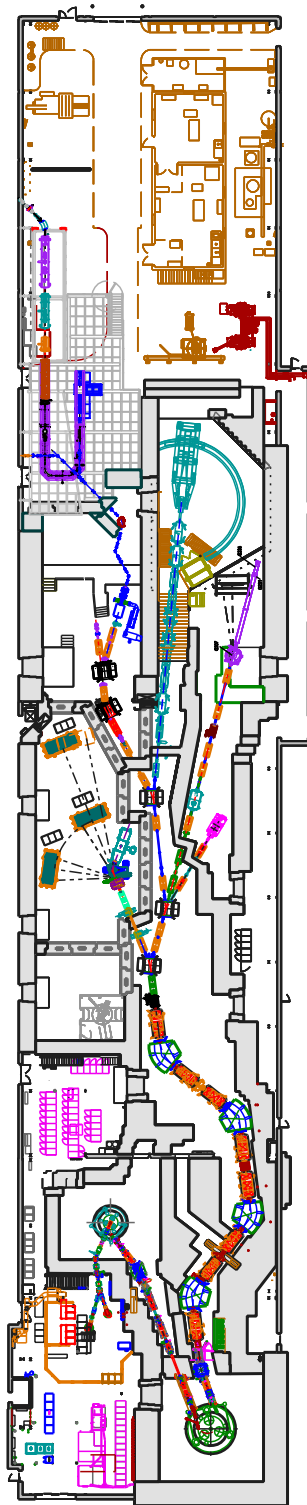


Figure 1.1: Current Layout of NSCL

The NSCL is currently constructing a new reaccelerated beam facility, ReA3[8], to be the world's first organization that provides stopped and low-energy rare isotope beams. Fast rare isotopes from the CCF will be stopped in a gas stopping systems, charge bred in an Electron Beam Ion Trap (EBIT) and reaccelerated in a compact superconducting linac. Beams coming from ReA3 will have energies ranging from 0.3 to 6 MeV per nucleon: 3 MeV/nucleon maximum for heavy ions such as uranium, and 6 MeV/nucleon for lighter ions. ReA3, expected to be completed in 2010 and available for first radioactive ion beam experiments in 2011, will provide the reacceleration capability for the next-generation Facility for Rare Isotope Beams (FRIB) to be built at MSU, and enable the community to develop programs and techniques with reaccelerated beams years before FRIB's operation.

1.1.2 Facility for Rare Isotope Beams (FRIB)

In December 2008, the Department of Energy (DOE) selected MSU to design and build a research facility for creating and utilizing rare isotope beams, the Facility for Rare Isotope Beams (FRIB). Figure 1.2 shows the proposed layout of the facility.

FRIB will use a superconducting heavy-ion driver linac to deliver stable beams of energy greater than 200 MeV/nucleon at beam power up to 400 KW to produce rare isotopes. Experiment will be possible with rare isotope beams at velocities similar to beams in the driver linac, at near zero velocity after stopping in a gas cell, or at intermediate velocity (0.3 to 12 MeV/nucleon) through reacceleration[9]. A conceptual schematic design of FRIB is shown in Figure 1.3. The project to design and establish FRIB started in May 2009, and is expected to be completed in 2018.

The proposed front end of this new facility uses two fully superconducting Electron Cyclotron Resonance (ECR) ion sources similar to Superconducting Source for Ions (SuSI) and an emittance collimation system equivalent to the one presented in this thesis.

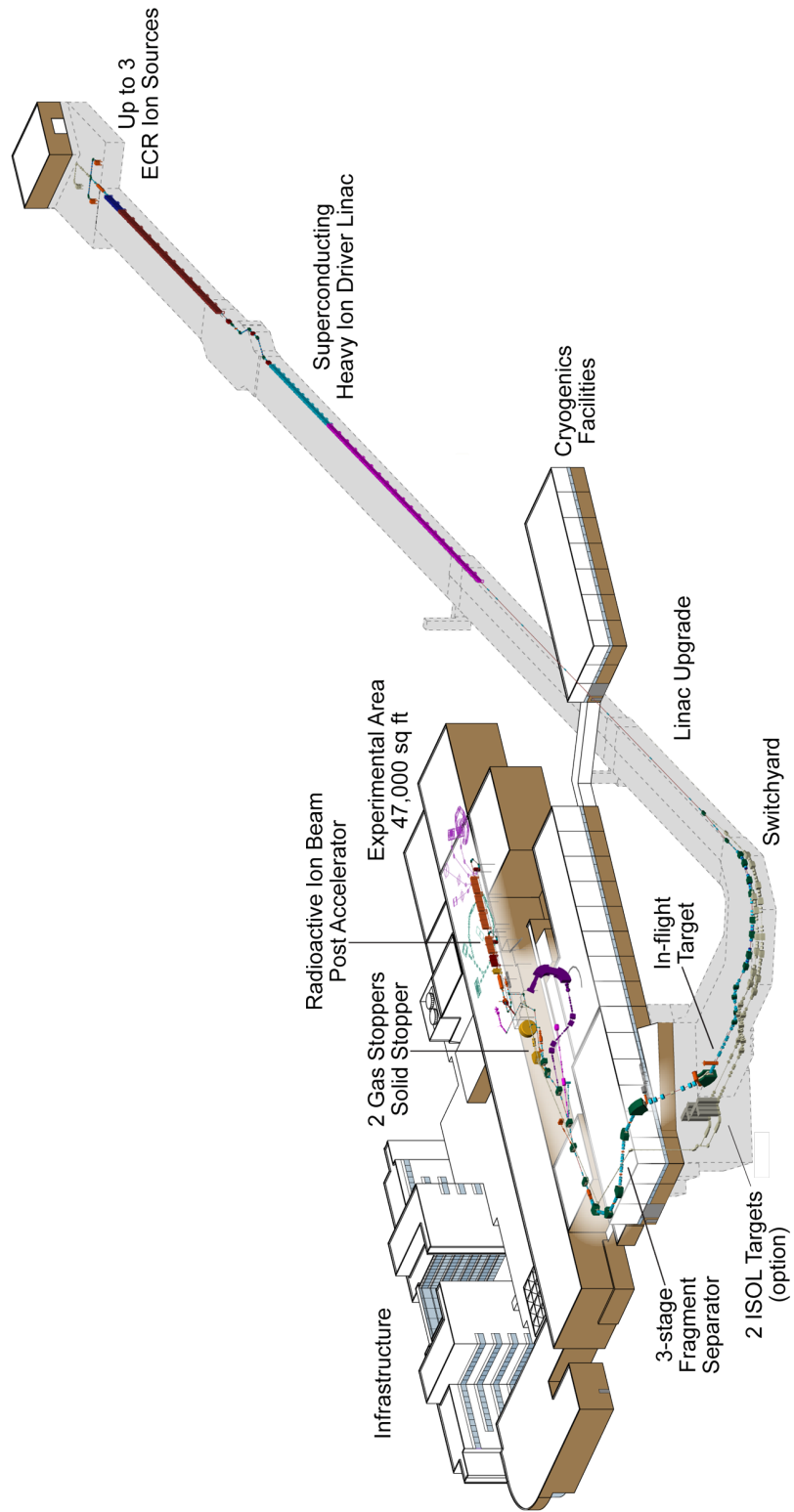


Figure 1.2: Proposed layout of FRIB

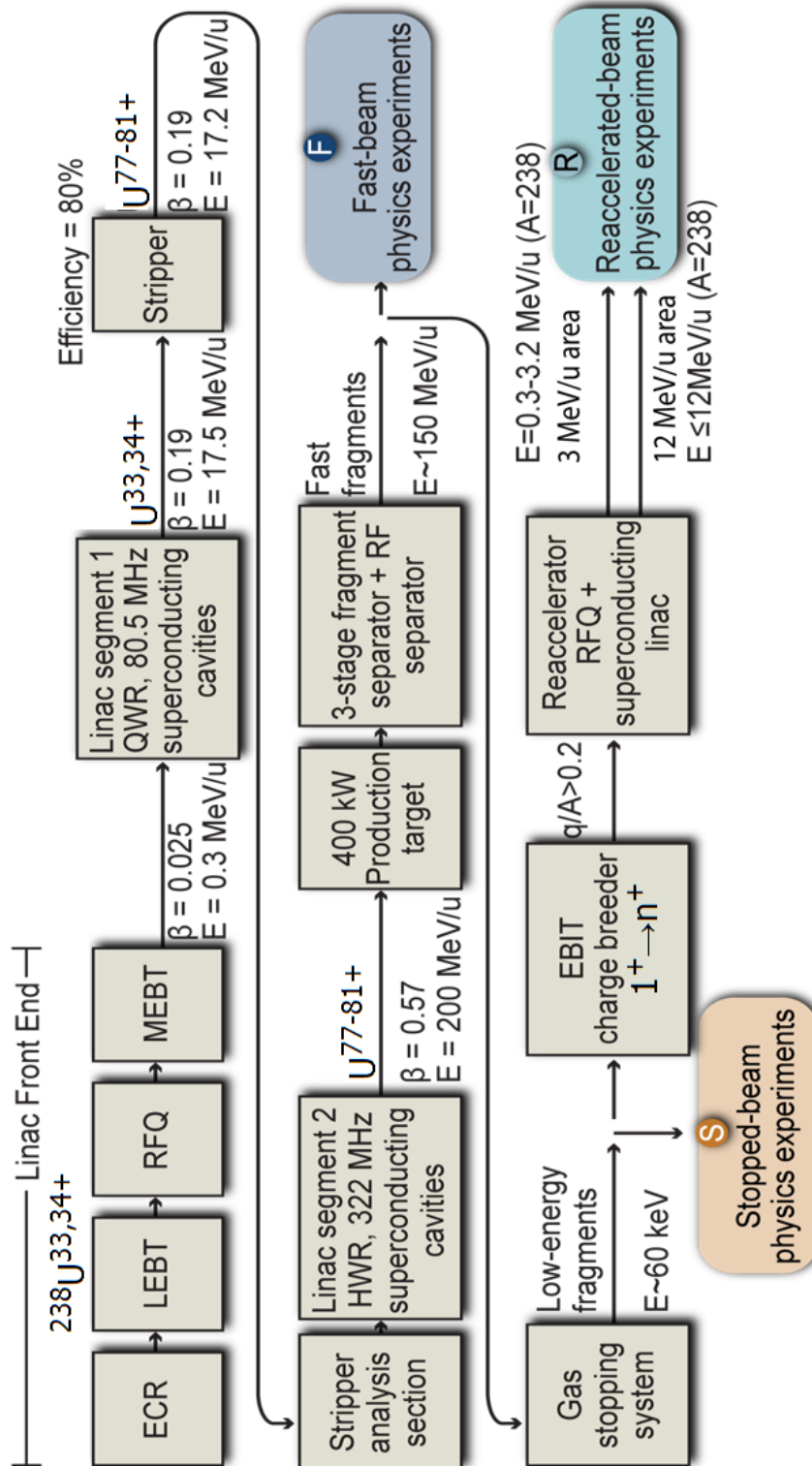


Figure 1.3: Conceptual schematic design of FRIB. The block diagram represents the items within FRIB technic scope.

1.2 Background Information

1.2.1 Electron Cyclotron Resonance (ECR) Ion Source

Electron Cyclotron Resonance (ECR) ion sources use electrons driven by microwaves to ionize elemental atoms, and have the capability to produce highly charged ion beams.

ECR ion sources have several advantages over other ion sources, including:

- the ability to deliver continuous beams of highly charged ions;
- easy to handle and operate over long periods of time;
- excellent long-term stability and reproducibility;
- low material consumption due to its low pressure (about 10^{-4} mbar) in operation suited for the production of expensive or radioactive elements[10].

The basic layout of an ECR ion source is shown in Figure 1.4.

When electrons move in a magnetic field, they gyrate due to the Lorentz force.

The gyration frequency, also called cyclotron frequency ω_{cyc} , is

$$\omega_{cyc} = \frac{eB}{m_e} ,$$

where e and m_e are the charge and mass of electron, and B is the magnetic field.

When a microwave is added, the electrons are accelerated if the electron cyclotron resonance condition is fulfilled:

$$\omega_{RF} = \omega_{cyc} = \frac{eB}{m_e} , \tag{1.1}$$

where ω_{RF} is the angular frequency of the microwave. Elements can then be ionized step by step through the electron impact ionization process and a plasma of electrons

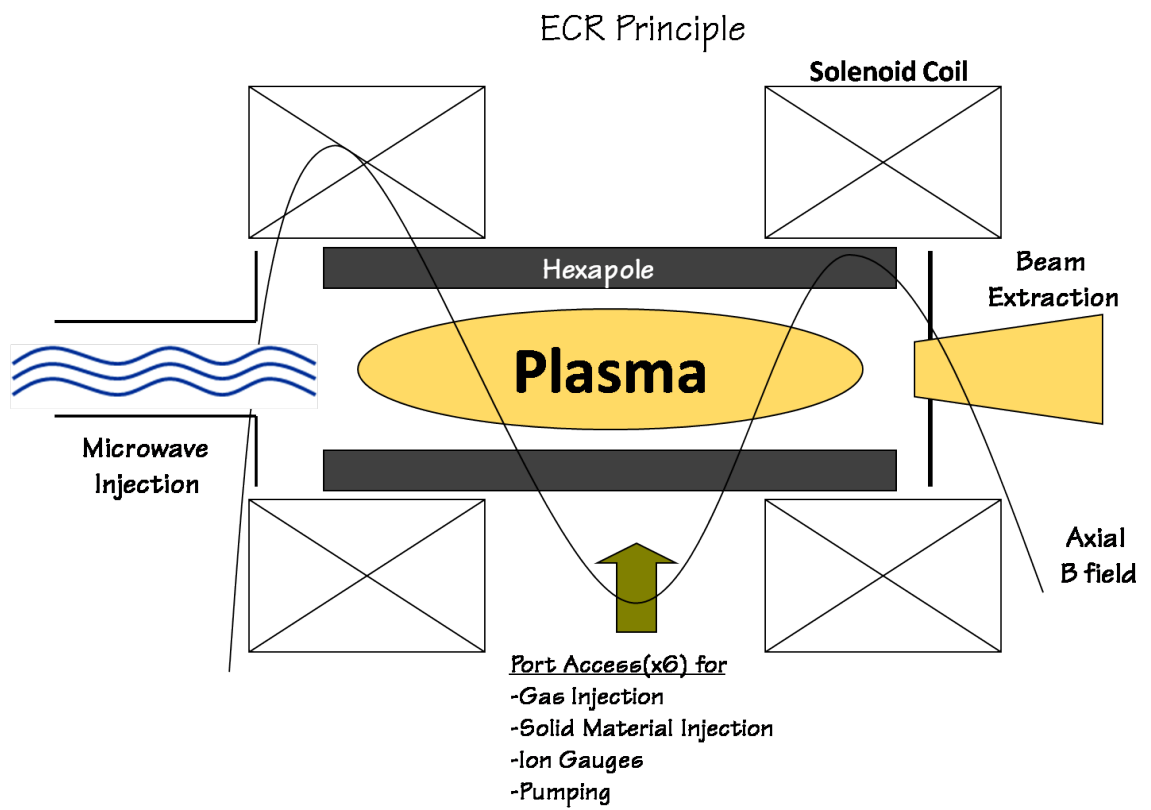


Figure 1.4: Basic layout of ECR ion source[11].

and ions is formed. Gas and metal elements both can be used as source material. Gases are injected into the ion source directly, while metals must be injected into the ion source after vaporization in an oven.

The plasma electrons are confined by a magnetic field which has its minimum strength at the center and increases radially. This magnetic field configuration is called minimum-B-configuration, and can be achieved by a superposition of an axial mirror field (so-called "magnetic bottle") produced by solenoids or permanent magnets and the radial magnetic field of a multipole magnet. As a result, a closed resonance surface is created where the electron cyclotron resonance condition is fulfilled. Figure 1.5 shows an example of the ECR resonance surface of Advanced Room Temperature Ion Source - B (ARTEMIS-B), an offline room temperature ECR ion source built at NSCL[12].

The massive ions are not accelerated in the plasma. They are confined by the space charge force of the electrons rather than the magnetic field. By applying a high voltage, the ions can be extracted from the ion source.

1.2.2 Beam Dynamics Basics

In this section, the basics of beam transport theory and beam emittance will be introduced for readers not familiar with accelerator physics.

Transfer Matrix and Beam Transport

In accelerator physics, the natural reference coordinate system is an orthogonal, right-handed coordinate system $(\hat{x}, \hat{y}, \hat{z})$ that follows the path of a reference particle. It is usually chosen to minimize the mathematical complexity and to maximize physical clarity for the description of the charged particle beam dynamics (Figure 1.6).

In this moving reference system, the position of a particle can be written as a 6

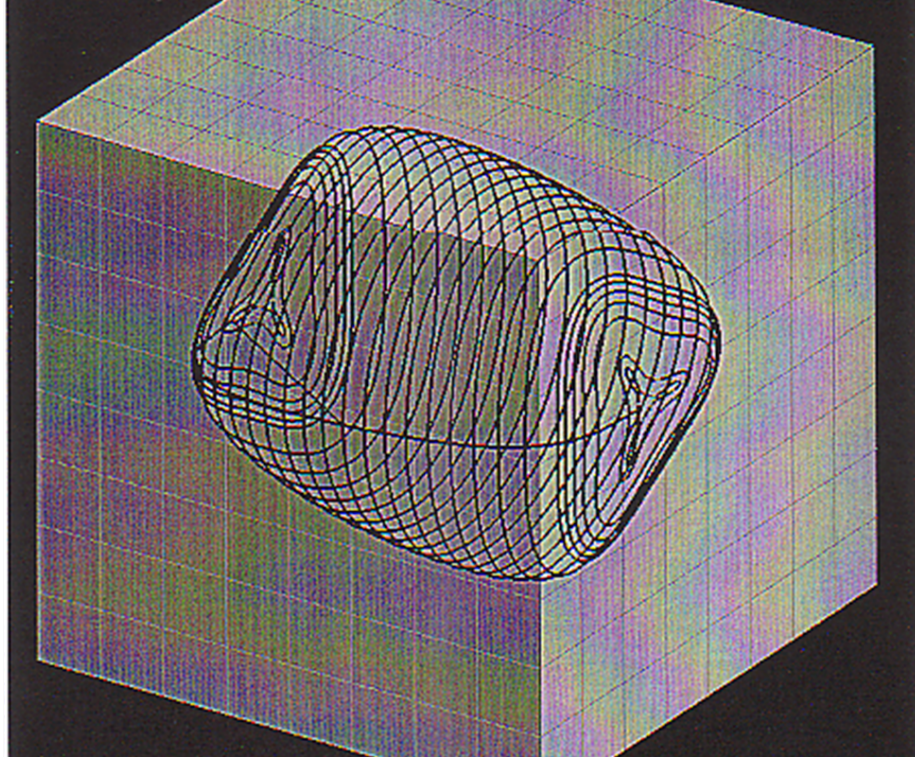


Figure 1.5: An example of ECR resonance surface of Advanced Room TEMperature Ion Source - B (ARTEMIS-B), an offline room temperature ECR ion source built at NSCL for the purpose of research.

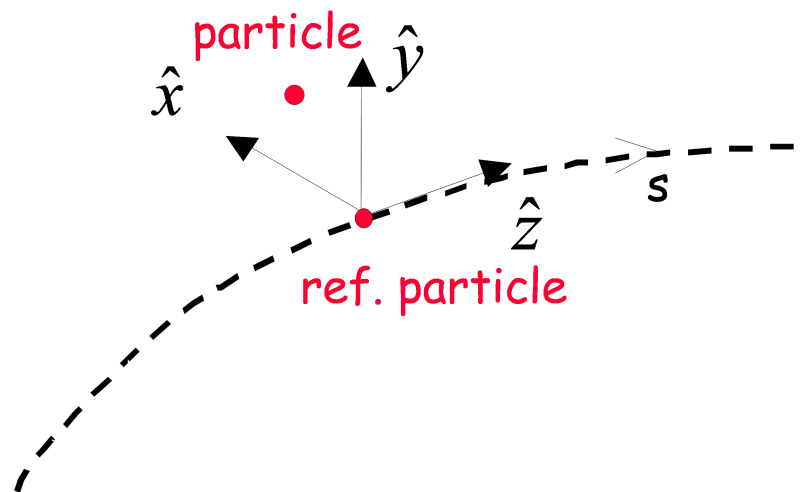


Figure 1.6: Natural reference coordinate system.

dimensional vector

$$U = \begin{pmatrix} x \\ x' \\ y \\ y' \\ z \\ \delta \end{pmatrix},$$

where δ is defined as the relative difference between the momentum of particle under consideration and that of the reference particle, $\delta = (p - p_{ref})/p_{ref}$, and the primes denote the derivatives with respect to s .

For linear transport from location s_0 to s_1 , the 6D vector transforms as

$$U_{s_1} = R_{s_0|s_1} U_{s_0}, \quad (1.2)$$

where $R_{s_0|s_1}$ is a 6×6 matrix whose elements depend on the transport elements between s_0 and s_1 . The R matrix is referred to as the transfer matrix between location s_0 and s_1 . The general expression for a transfer matrix R is

$$R = \begin{pmatrix} R_{11} & R_{12} & \cdots & R_{16} \\ R_{21} & R_{22} & \cdots & R_{26} \\ \vdots & \vdots & \ddots & \vdots \\ R_{61} & R_{62} & \cdots & R_{66} \end{pmatrix}.$$

It is usually convenient to look at the matrix using 2×2 block matrices

$$R = \begin{pmatrix} R_{xx} & R_{xy} & R_{xz} \\ R_{yx} & R_{yy} & R_{yz} \\ R_{zx} & R_{zy} & R_{zz} \end{pmatrix}.$$

The off-diagonal blocks indicate the coupling between planes during transport. In the absence of coupling, the matrix is block-diagonal:

$$R = \begin{pmatrix} R_{xx} & 0 & 0 \\ 0 & R_{yy} & 0 \\ 0 & 0 & R_{zz} \end{pmatrix} .$$

For a system that transports particles through N elements with transfer matrices $R_1 \cdots R_N$, as shown in Figure 1.7, the overall transfer matrix for that system is given by the product

$$R = R_N \cdots R_2 R_1 .$$

Recalling the matrix manipulation rule, the transpose of R is given by

$$R^T = R_1^T R_2^T \cdots R_N^T ,$$

and the inverse

$$R^{-1} = R_1^{-1} R_2^{-1} \cdots R_N^{-1} .$$

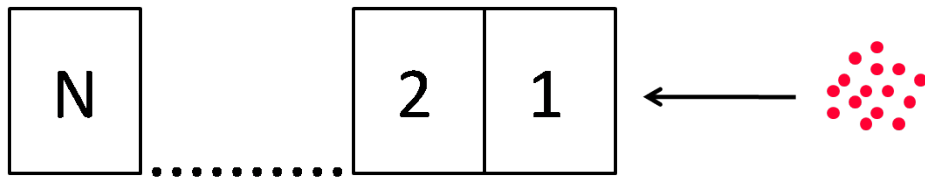


Figure 1.7: A system transporting particles through N elements.

Beam Emittance

In order to study the motion of the beam, i.e. an ensemble of particles, it is useful to characterize the ensembles by simple geometric forms, which require few descriptive

parameters. One of the most useful forms is the 6D hyperellipsoid.

The surface equation of hyperellipsoid in N dimensions is

$$U^T \sigma^{-1} U = 1 \quad (1.3)$$

where σ is a 6×6 matrix containing the coefficients of the hyperellipsoid. In the 2×2 block representation,

$$\sigma = \begin{pmatrix} \sigma_{xx} & \sigma_{xy} & \sigma_{xz} \\ \sigma_{yx} & \sigma_{yy} & \sigma_{yz} \\ \sigma_{zx} & \sigma_{zy} & \sigma_{zz} \end{pmatrix},$$

where the 3 diagonal blocks are related to the 2D projection of the hyperellipsoid on the xx' , yy' and zz' plane; the 6 non-diagonal blocks represent the coupling between planes, i.e. tilt of the hyperellipsoid projections on the 2D planes.

The volume of a hyperellipsoid in N dimensions is

$$V_N = \frac{\pi^{N/2}}{\Gamma(1 + N/2)} \sqrt{\det(\sigma)} \quad (1.4)$$

where $\det(\sigma)$ is the determinant of the σ matrix and $\Gamma(x)$ is the Gamma function having the properties that

$$\Gamma(x + 1) = x\Gamma(x)$$

$$\Gamma(0) = 1$$

$$\Gamma\left(\frac{1}{2}\right) = \sqrt{\pi}.$$

For a block diagonal matrix of the form

$$A = \begin{pmatrix} A_1 & 0 & \cdots & 0 \\ 0 & A_2 & \cdots & 0 \\ \vdots & \vdots & \ddots & \vdots \\ 0 & 0 & \cdots & A_k \end{pmatrix},$$

the determinant of the matrix is equal to the product of the determinants of each of the diagonal blocks:

$$\det(A) = \det(A_1)\det(A_2) \cdots \det(A_k) .$$

In the absence of non-diagonal coupling,

$$\sigma = \begin{pmatrix} \sigma_{xx} & 0 & 0 \\ 0 & \sigma_{yy} & 0 \\ 0 & 0 & \sigma_{zz} \end{pmatrix},$$

we have

$$V_{2D} = \pi \sqrt{\det(\sigma_{xx})} = \pi \epsilon_x ,$$

where the 2D emittance in xx' plane is defined as

$$\epsilon_x = \frac{V_{2D}}{\pi} = \frac{\sqrt{\det(\sigma_{xx})}}{\pi} .$$

It is the 2D "volume" or area of the hyperellipsoid projection on xx' plane divided

by π . Similarly, the 2D emittances in yy' and $z\delta$ plane are

$$\begin{aligned}\epsilon_y &= \frac{V_{2D}}{\pi} = \frac{\sqrt{\det(\sigma_{yy})}}{\pi} \\ \epsilon_z &= \frac{V_{2D}}{\pi} = \frac{\sqrt{\det(\sigma_{zz})}}{\pi} .\end{aligned}$$

The 4D and 6D emittances are also proportional to the volume of the hyperellipsoid in the corresponding space, defined as[13]

$$\begin{aligned}V_{4D} &= \frac{\pi^2}{2} \sqrt{\det(\sigma_{xx})\det(\sigma_{yy})} = \frac{\pi^2}{2} \epsilon_x \epsilon_y = \pi^2 \epsilon_{4D} \\ V_{6D} &= \frac{\pi^3}{6} \sqrt{\det(\sigma_{xx})\det(\sigma_{yy})\det(\sigma_{zz})} = \frac{\pi^3}{6} \epsilon_x \epsilon_y \epsilon_z = \pi^3 \epsilon_{6D} ,\end{aligned}$$

according to Equation (1.4). For DC beams, i.e. beams not bunched, with an uncorrelated σ matrix, we approximate the 4D transverse emittance as the product of the two 2D transverse emittances:

$$\epsilon_{4D} \sim \epsilon_x \cdot \epsilon_y .$$

When projected on 2D subspaces, the projections of the 6D hyperellipsoid are 2D ellipses on all 2D subspaces. The general equation of a centered ellipse can be written as

$$\gamma x^2 + 2\alpha x x' + \beta x'^2 = \epsilon_x , \quad (1.5)$$

where α , β , and γ are called Twiss parameters, which satisfy the Courant-Snyder invariant [14],

$$\beta\gamma - \alpha^2 = 1 .$$

In matrix form, the ellipse equation (1.5) can be written as

$$\begin{pmatrix} x & x' \end{pmatrix} \cdot \begin{pmatrix} \gamma & \alpha \\ \alpha & \beta \end{pmatrix} \cdot \begin{pmatrix} x \\ x' \end{pmatrix} = \epsilon_x ,$$

A more general form is:

$$U^T \sigma_{2D}^{-1} U = \epsilon_{2D} . \quad (1.6)$$

Comparing with the surface equation of the hyperellipsoid, Equation (1.3), we have

$$\sigma_{2d}^{-1} = \frac{1}{\epsilon_{2D}} \begin{pmatrix} \gamma & \alpha \\ \alpha & \beta \end{pmatrix} ,$$

and the 2D σ matrix is then

$$\sigma_{2D} = \epsilon_{2D} \begin{pmatrix} \beta & -\alpha \\ -\alpha & \gamma \end{pmatrix} .$$

The geometrical meaning of Twiss parameter is explained in Figure 1.8; β , a function of s , relates directly to beam size at that position as $\sqrt{\beta\epsilon}$.

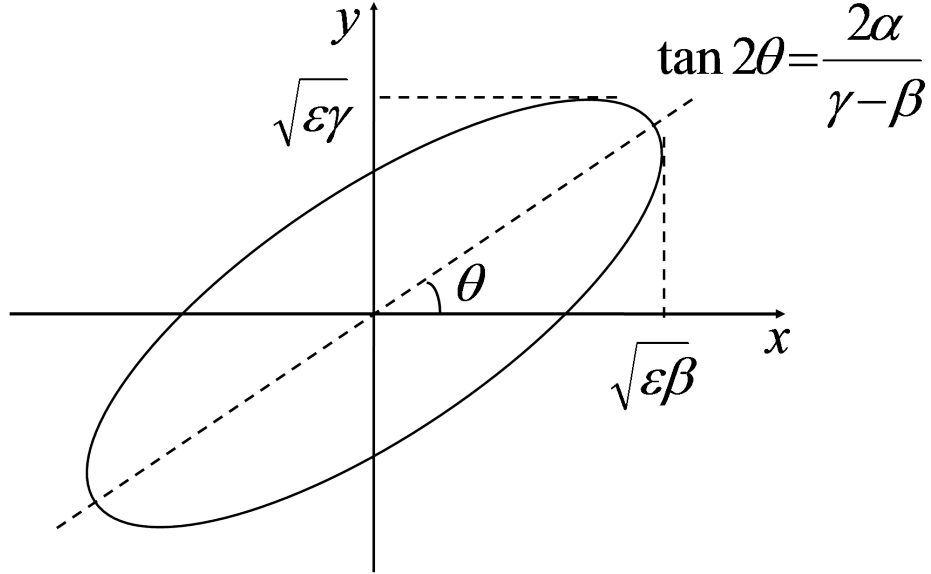


Figure 1.8: Geometric meaning of Twiss parameters[15].

As introduced in Section 1.2.2, the linear transformation of the phase space coordinates is given by Equation (1.2). By substituting this equation into the surface

equation of a hyperellipsoid (1.3), we derive the linear transformation of the hyperellipsoid:

$$\sigma_1 = R\sigma_0R^T . \quad (1.7)$$

Liouville's Theorem states that under the influence of conservative forces the density and total volume in phase space are conserved, which means that the 6D emittance of the beam will be conserved during the transport.

In the absence of acceleration and coupled optics, such as skew quadrupoles, solenoids, etc., the 2D emittance in the transverse planes will be conserved. However, when coupled optics is present, the transverse planes become coupled and the 2D emittance in each of the transverse planes is no longer conserved. At the same time, when the particles in the beam undergo acceleration or deceleration, the transverse 2D emittance will not be conserved as well; however, the normalized emittance will be conserved. The normalized emittance is defined as

$$\epsilon_{n,2D} = \beta\gamma\epsilon_{2D} ,$$

where β and γ are relativistic parameters, rather than the Twiss parameters.

Although the total 6D volume is conserved, the effective volume may not be conserved under various conditions (Figure 1.9), for example due to the presence of nonlinearities in the field configurations through which the particles are transported.

In practice, the effective volume is more important than the 6D volume, as it relates directly to the beam size. It is important to limit the beam size to avoid beam losses.

To describe the parameters of the effective volume, Lapostolle[17] and Sacherer[18] introduced rms (root-mean-square) quantities to describe the beam parameters associated with the effective volume. The 2D rms emittances are calculated from the

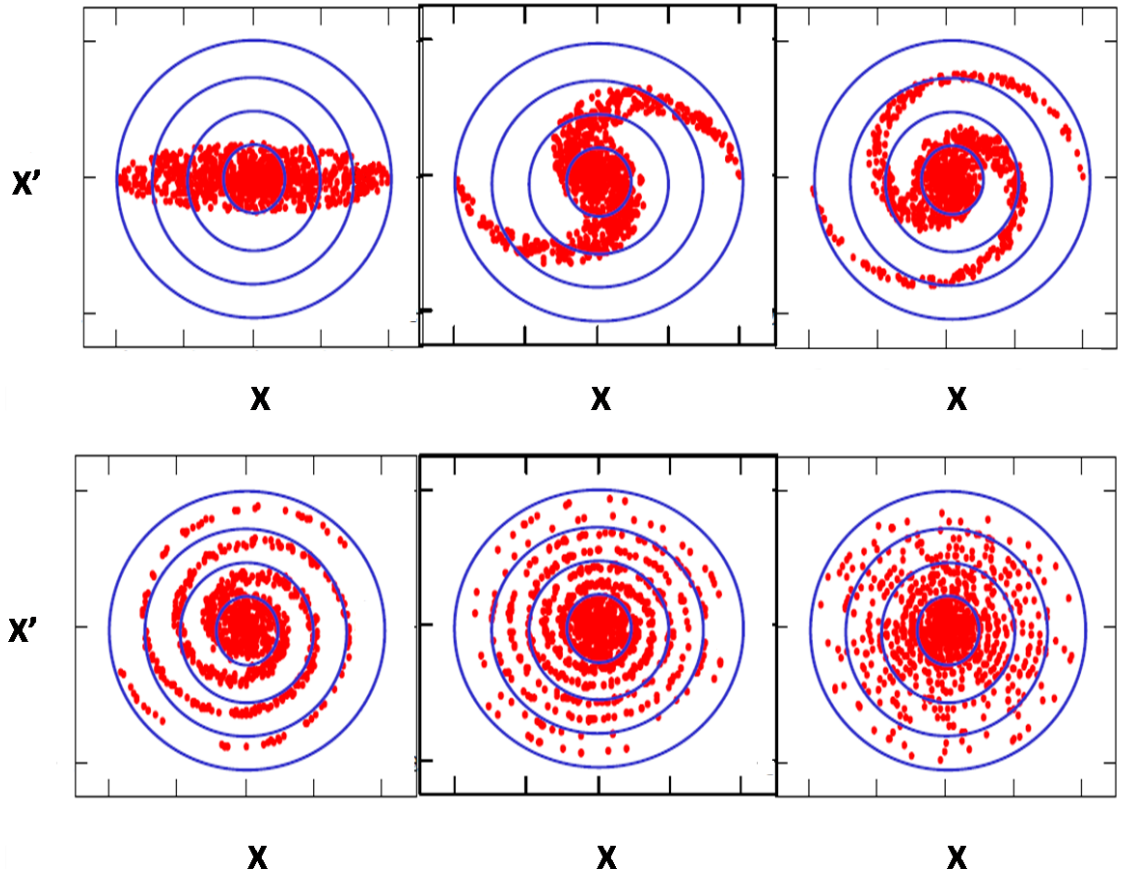


Figure 1.9: Example of emittance filamentation, where the total volume in phase space is conserved while the effective volume (footprint) is not[16].

distribution using the second order momenta

$$\epsilon_{rms} = \sqrt{\langle x^2 \rangle \langle x'^2 \rangle - \langle xx' \rangle},$$

and the rms Twiss parameters are

$$\alpha_{rms} = -\langle xx' \rangle / \epsilon_{rms}$$

$$\beta_{rms} = \langle x^2 \rangle / \epsilon_{rms}$$

$$\gamma_{rms} = \langle x'^2 \rangle / \epsilon_{rms}.$$

They satisfy the Courant-Snyder invariant $\beta_{rms}\gamma_{rms} - \alpha_{rms}^2 = 1$ as well. Figure 1.10 shows the geometrical representation of the rms ellipse.

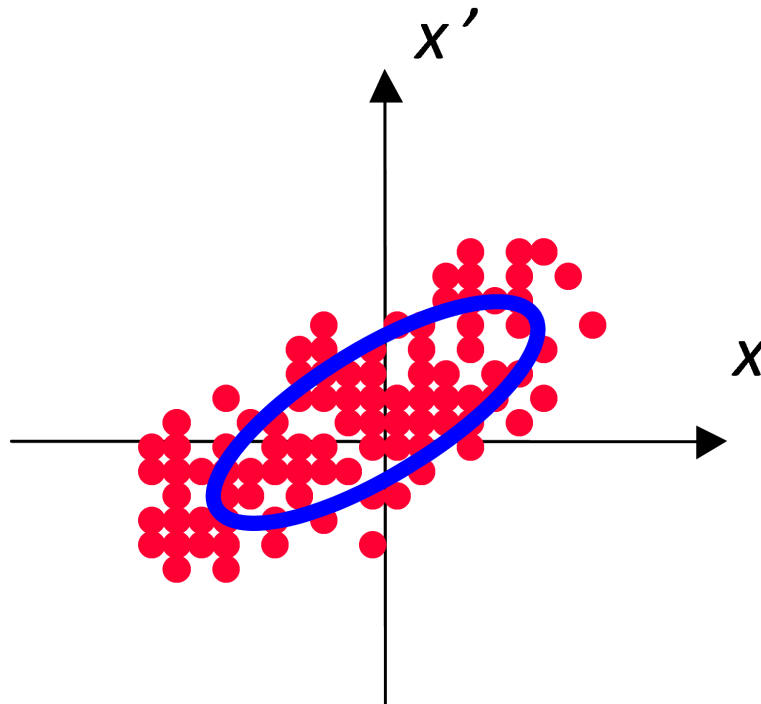


Figure 1.10: Geometric representation of the rms ellipse[15].

The effective or 100% 2D emittance that encapsulates all particles is given by

$$\epsilon_{100\%} = n\epsilon_{rms} ,$$

where n is a constant that differs with the distribution of the beam. For a beam in K-V distribution, $n = 4$; Waterbag distribution, $n = 6$; Gaussian, $n = \infty$.

1.3 Superconducting Source for Ions (SuSI)

The Superconducting Source for Ions (SuSI) is a newly designed, fully superconducting ECR ion source operated at NSCL. It is working at 14.5 and 18 GHz microwave frequency currently, and could be upgraded to 24 GHz in the future. The development of SuSI is aimed at replacing the former superconducting ion source SC-ECR and to provide higher intensity of heavy ion beams of medium charge state to the CCF. It will also provide NSCL the experience of both design and fabrication of a high performance ECR ion source for the driver linac of the future FRIB. A cross-sectional view of SuSI is shown in Figure 1.11.

According to the currently accepted semi-empirical design criteria[19], the magnetic confinement of an ECR ion source should be characterized as:

- an axial magnetic trap with $B_{inj} \approx 4B_{ECR}$ at the injection side, $B_{ext} \approx 2B_{ECR}$ at the extraction side, with a minimum magnetic field $B_{min} \approx 0.8B_{ECR}$ in the middle;
- a radial confinement magnetic field $B_{rad} \approx 2B_{ECR}$;
- the extraction magnetic field also correlates to the radial field by $B_{ext} \approx 0.9B_{rad}$.

The resonant magnetic field value B_{ECR} can be obtained according to Equation (1.1);

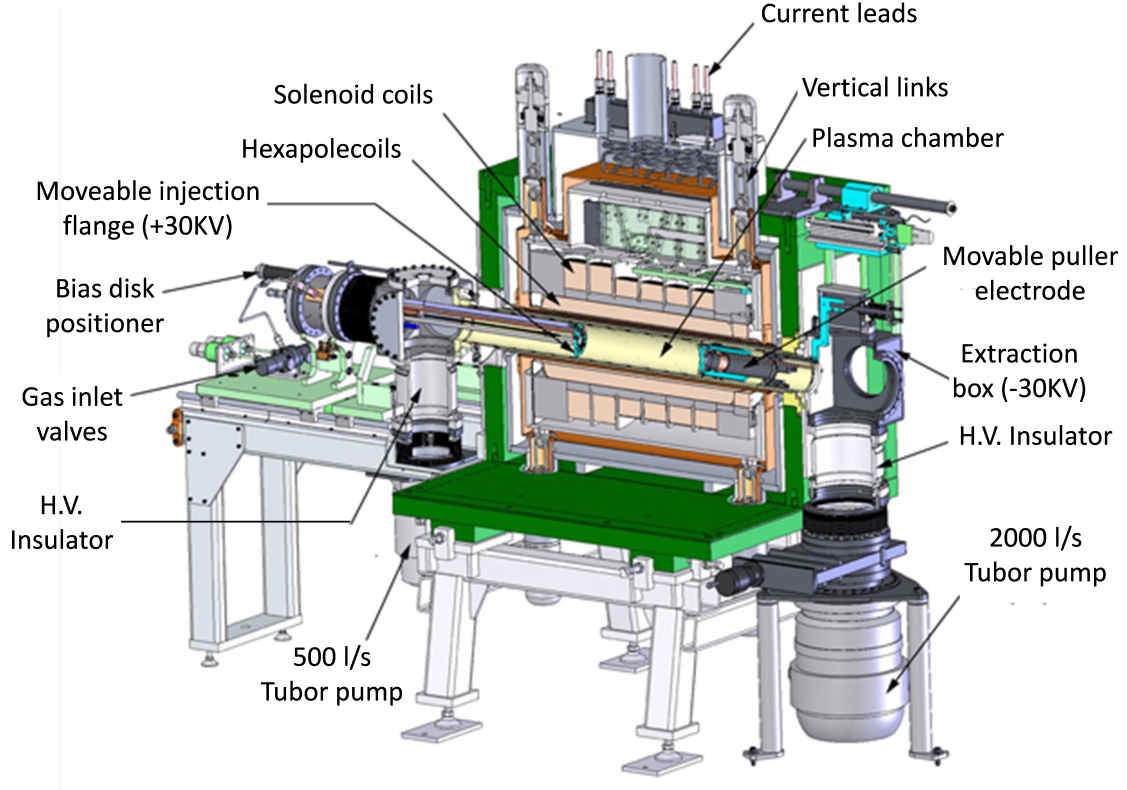


Figure 1.11: A cross-sectional view of SuSI

for 18 GHz microwave frequency, $B_{ECR} = 0.64$ T.

To reach this magnetic field for 18 GHz microwave frequency in a plasma chamber of 100 mm diameter, a superconducting magnetic system was chosen. The system has the advantage of having a tunable radial magnetic field with no risk of demagnetization of the permanent magnets which are used in a room temperature hexapole system for the radial confinement, etc.[20].

In SuSI, the flexible magnetic field concept was introduced[21, 22]. In this concept, the axial magnetic field profile of SuSI can be adjusted by 6 independent solenoids; as a result, both the gradient around the position where the magnetic field has its minimum and the position of the maximum magnetic field (with respect to the fixed plasma electrode) can be optimized. Beam studies at RIKEN have shown that such optimization could lead to an increase in intensity of extracted beam[23]. The injec-

tion assembly is mounted on a movable baffle that can change the injection flange over 10 cm so as to change the length of the plasma chamber between 40 and 50 cm giving a plasma volume between 3.1 and 3.9 liters. The injection flange includes a bias disk, which can be changed by 2 inches relative to the injection flange, an oven and 2 waveguides for dual injection of 14 and 18 GHz microwave.

Results obtained so far for the production of medium charge state beams for various gaseous and metallic elements with SuSI were shown to be on par with other similar ECR sources[24].

1.4 Need For Emittance Collimation

Although the current of the beam coming from the source satisfies the requirement of injection into the CCF, the emittance of the beam will strongly affect the efficiency of the injection as well. For efficient injection into the K500 acceptance, a beam with an emittance below $75 \pi \cdot \text{mm} \cdot \text{mrad}$ [2] is necessary. Empirical experience indicates that beam with emittances quite smaller than the K500 injection acceptance are transported more efficiently.

However, many factors in the ECR extraction system will lead to the degradation of the beam emittance.

When extracted from the ECR source, the beam acquires a strong azimuthal momentum due to the decreasing magnetic field which leads to a significant emittance increase. According to research done at Lawrence Berkeley National Laboratory (LBNL)[25], the emittance growth due to the decreasing magnetic field, i.e. the magnetic emittance, is quantified as

$$\epsilon_{rms,n}^{MAG} = 0.032 \cdot r^2 \cdot B_0 \cdot \frac{1}{A/Q} . \quad (1.8)$$

$\epsilon_{rms,n}^{MAG}$ is the normalized rms 2D magnetic emittance in $\pi \cdot \text{mm} \cdot \text{mrad}$; r the radial size of the plasma extraction electrode in mm; B_0 the axial magnetic field in T; A/Q the mass over charge ratio. As a result, the emittance of the beam coming out of the source should be greater than this magnetic emittance. However, when using the AECR-U ion source, the beam emittance is smaller than the expected magnetic emittance[26]. On the contrary, the result from the front-end tests done at Argonne National Laboratory (ANL) shows the beam emittance is greater than the expected magnetic emittance[27].

For the SuSI ECR, the radius of plasma extraction electrode is $r=4$ mm, and the axial magnetic field $B_0 = 0.64$ T. For a $^{40}\text{Ar}^{7+}$ beam extracted with 24.43 kV extraction voltage, the normalized rms 2D magnetic emittance is

$$\epsilon_{rms,n}^{MAG} \approx 0.06 \pi \cdot \text{mm} \cdot \text{mrad} ,$$

and the corresponding geometric rms magnetic emittance is

$$\epsilon_{rms}^{MAG} = \beta\gamma\epsilon_{rms,n}^{MAG} \approx 19 \pi \cdot \text{mm} \cdot \text{mrad} .$$

Assuming a Waterbag distribution, the 100% geometric emittance is then calculated,

$$\epsilon_{100\%}^{MAG} = 5\epsilon_{rms}^{MAG} \approx 95 \pi \cdot \text{mm} \cdot \text{mrad} ,$$

which is larger than the acceptance of the K500, $75 \pi \cdot \text{mm} \cdot \text{mrad}$.

In addition, the emittance of beams with lower Q/A ions can be considerably degraded by the space charge effect of the higher Q/A ions. For example, Figure 1.12 shows the images of Krypton beams with different charge states on a beam viewer after the selecting magnet obtained at SuSI. Hollow distributions can be observed for beams with lower Q/A ions, which is due to the significant repulsive forces on the core

part of the lower Q/A ions produced by the higher Q/A ions. This beam brightness degradation mechanism was investigated and explained by [28, 6]. Figure 1.13~1.15 are the corresponding horizontal (xx') and vertical (yy') emittances measured by an Allison emittance scanner for the $^{84}\text{Kr}^{9+}$, $^{84}\text{Kr}^{13+}$ and $^{84}\text{Kr}^{17+}$ beams. The phase space distributions for the $^{84}\text{Kr}^{17+}$ beam are centered on intense cores while the distributions for $^{84}\text{Kr}^{13+}$ and $^{84}\text{Kr}^{9+}$ beam appear hollow. This result is in qualitative agreement with the images observed on the beam viewer.

Beside the magnetic emittance and the space charge effect, other factors including the non-uniformity of the ECR plasma, tuning of the ECR source parameters, etc., can also impact the emittance of the beam.

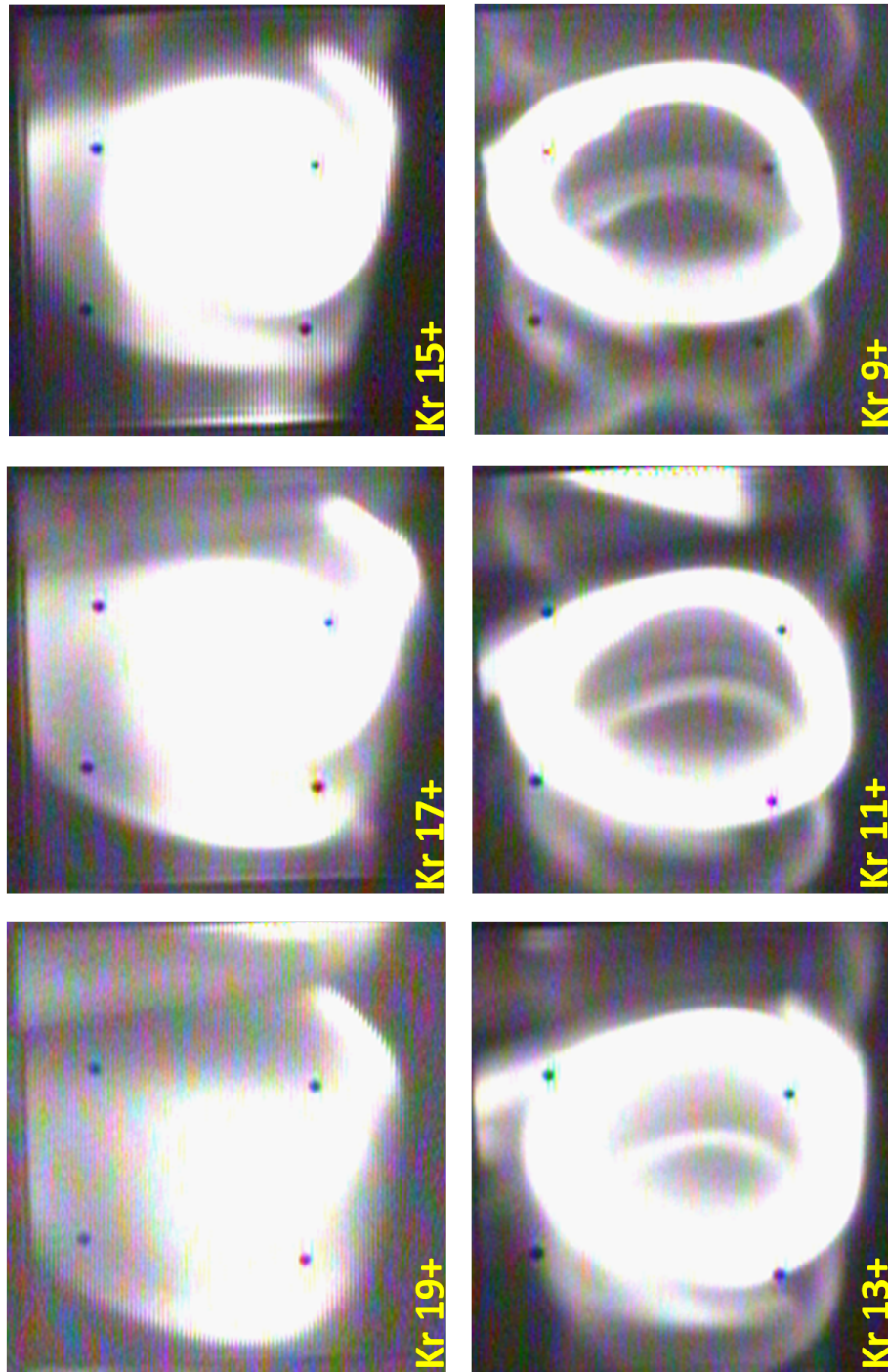


Figure 1.12: Images for different charge states of a Krypton beam on a beam viewer after the selecting magnet.

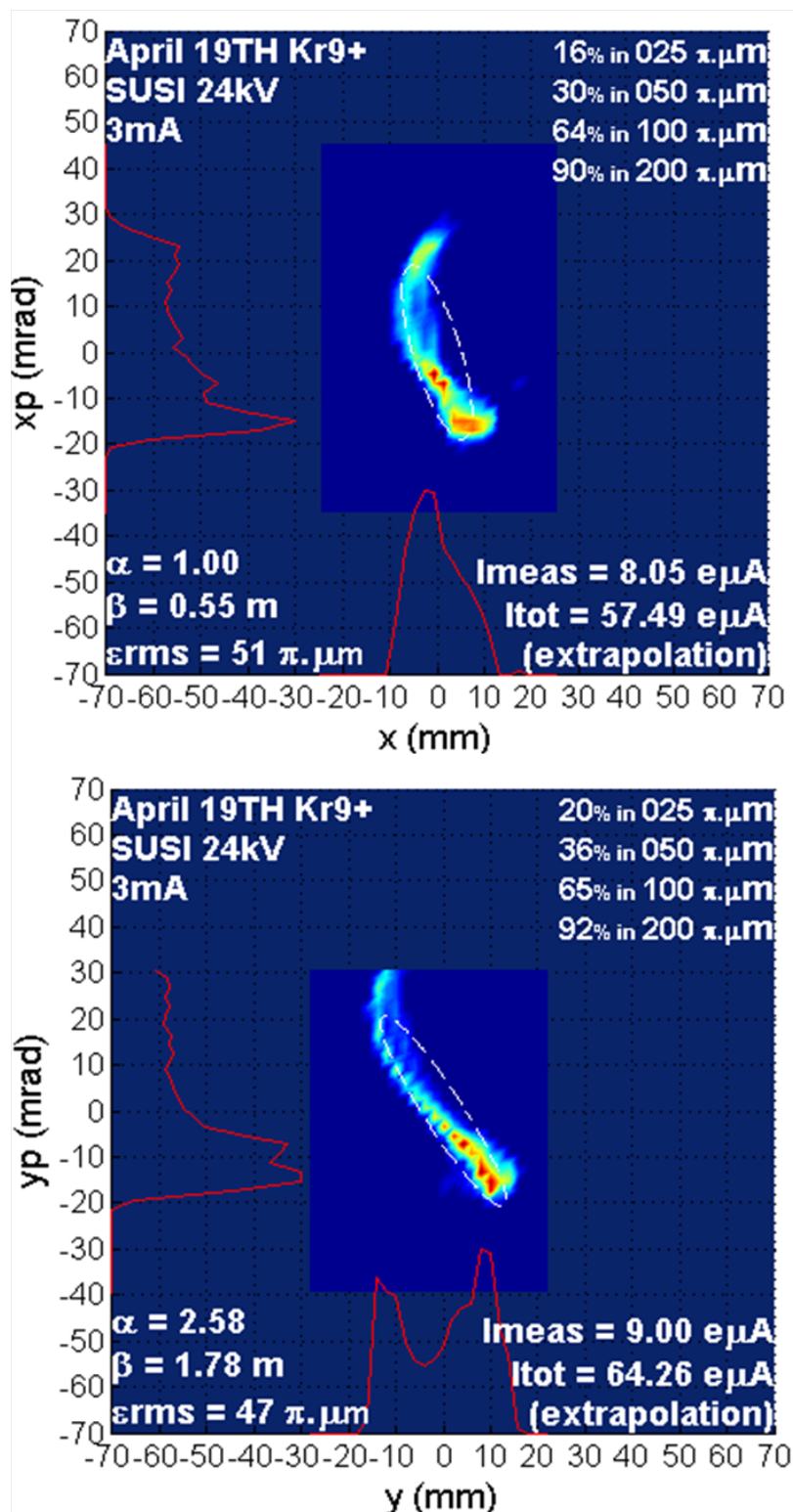


Figure 1.13: Transverse emittances for $^{84}\text{Kr}^{9+}$, where emittance are hollow.

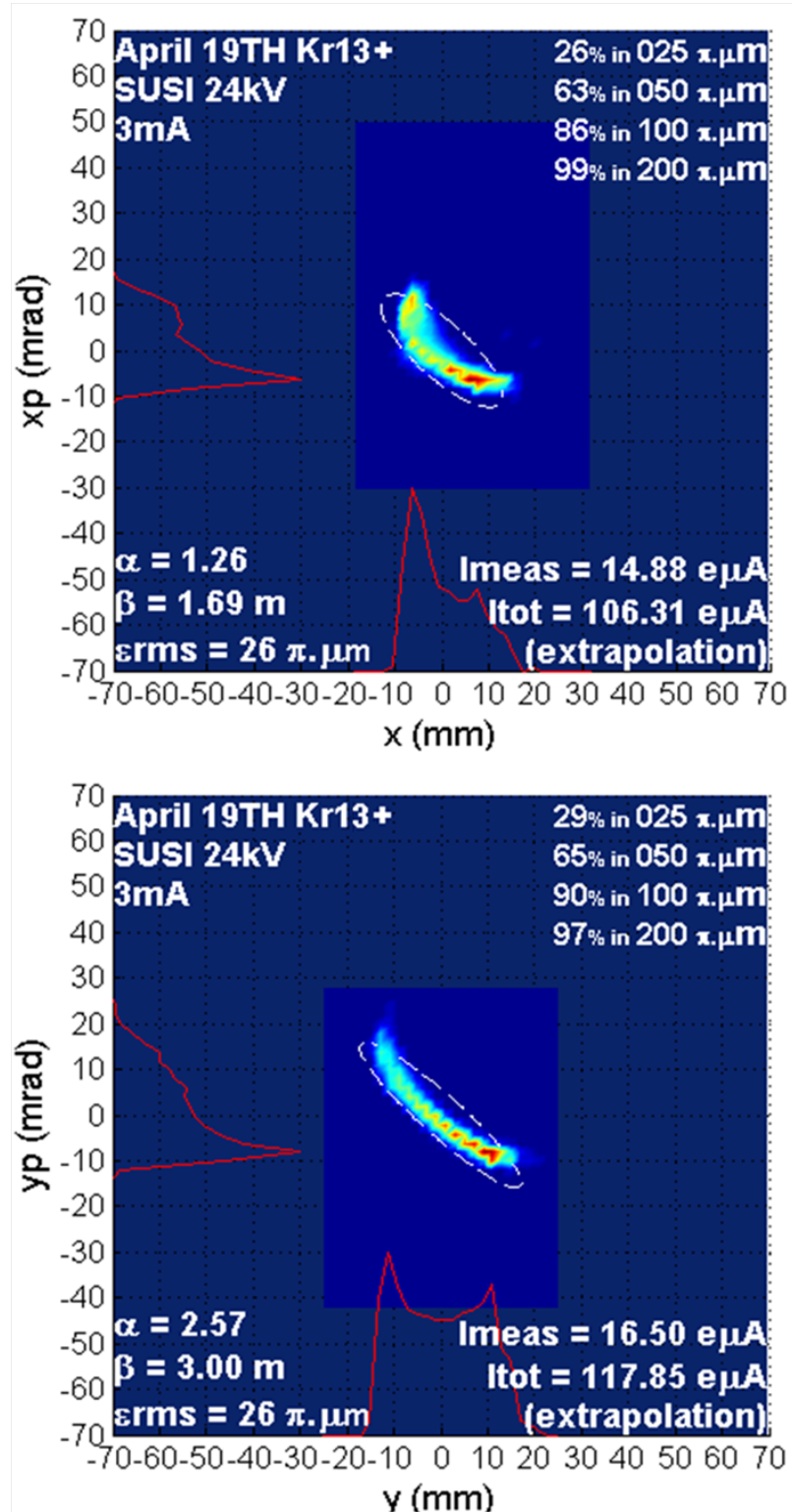


Figure 1.14: Transverse emittances for $^{84}\text{Kr}^{13+}$, where emittance are hollow.

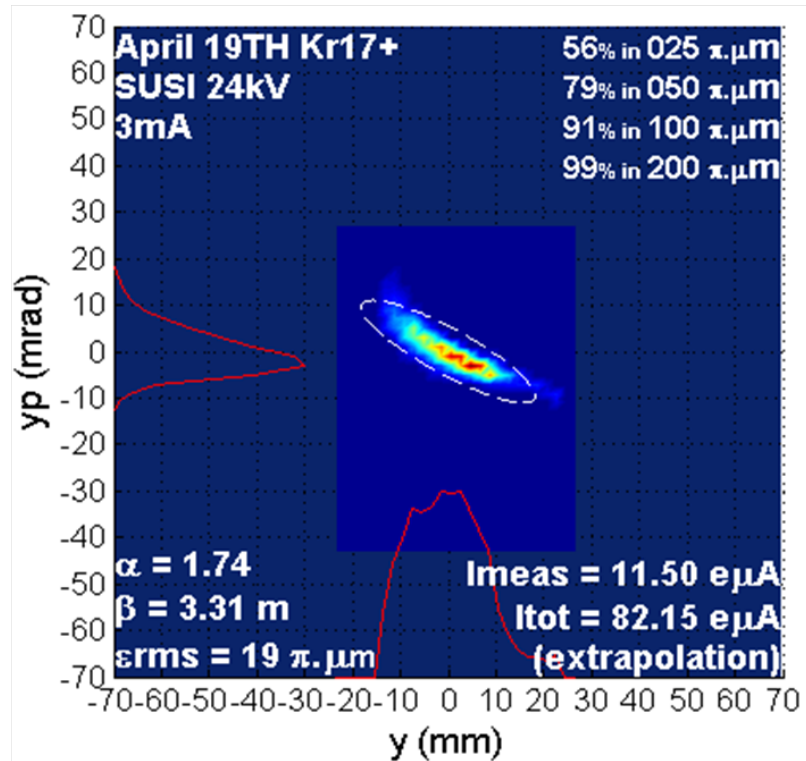
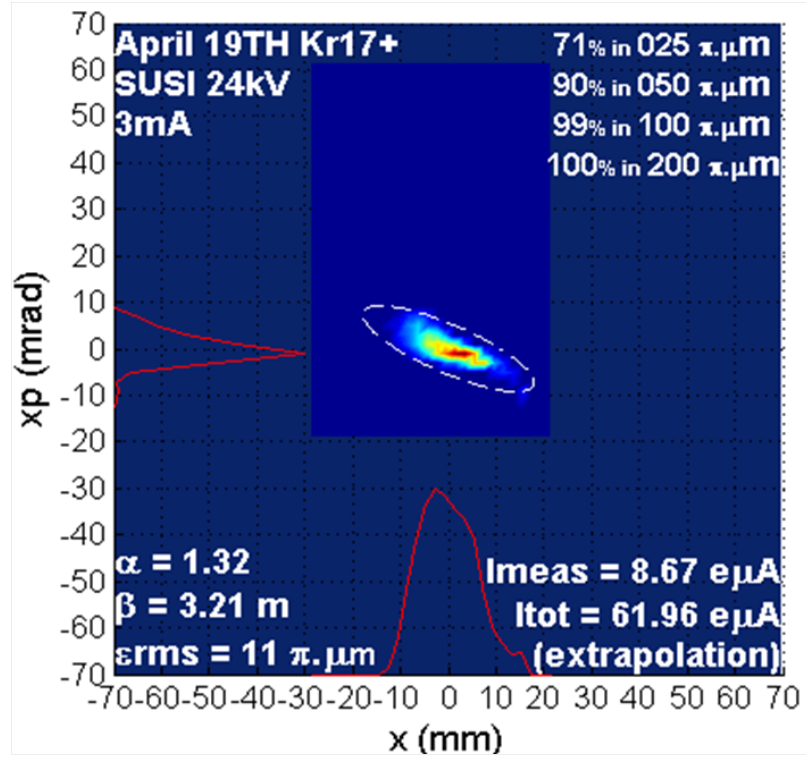


Figure 1.15: Transverse emittances for $^{84}\text{Kr}^{17+}$, where emittance are centered on intense cores.

Chapter 2

EMITTANCE COLLIMATION CHANNEL DESIGN

2.1 Basic Principle

To collimate the beam size in xx' and yy' phase spaces, we decided to utilize a scheme of multiple slits with phase space rotation in between. The basic idea is to cut the beam in xy space with slits, rotate in phase space, and repeat this process. For effective collimation, the rotation in phase space (phase advance) should be greater than 90 degrees, and more cuts are preferable for better results.

Both quadrupole lenses and solenoid lenses have the capability of rotating the beam in phase space. By looking at the inventory of our lab, we found there were several solenoids available to use. To save time and money, we decided to use these solenoids to rotate the beam in phase space instead of quadrupoles. The yoke length of these solenoids is 0.428 m.

To minimize the disruption to the ECR pit, the geometrical size of our design needed to be compatible with the available space in the pit. Therefore, we made a decision to use only three of the solenoids in the design, which restricted the cuts in

xy space to four.

The designed channel can be divided into three cells . Each cell is in the configuration of drift-solenoid-drift with slits on both sides.

In 2D, the matrix for a drift with length $D(m)$ is

$$R_{drift} = \begin{pmatrix} 1 & D & 0 & 0 \\ 0 & 1 & 0 & 0 \\ 0 & 0 & 1 & D \\ 0 & 0 & 0 & 1 \end{pmatrix},$$

and the matrix for a solenoid with length $L(m)$ and magnetic field $B(T)$ is

$$R_{solenoid} = \begin{pmatrix} C^2 & \frac{1}{k}SC & SC & \frac{1}{k}S^2 \\ -kSC & C^2 & -kS^2 & SC \\ -SC & -\frac{1}{k}S^2 & C^2 & \frac{1}{k}SC \\ kS^2 & -SC & -kSC & C^2 \end{pmatrix},$$

where $k = \frac{B}{2B\rho}$, $B\rho$ (Tm) is the magnetic rigidity of the beam, $C = \cos(kL)$, and $S = \sin(kL)$.

The transfer matrix of each cell can be then calculated as

$$R_{cell} = R_{drift} \cdot R_{solenoid} \cdot R_{drift} \cdot$$

In approximation, the phase advance in phase space (σ), eigen beta ($\bar{\beta}$), and the

phase rotation in xy space (θ_{xy}) of each cell are:

$$\sigma \approx \frac{B}{2B\rho} \sqrt{SL}, \quad (2.1)$$

$$\bar{\beta} = \frac{S}{\sigma} \approx \frac{2B\rho}{B} \sqrt{L/S}, \quad (2.2)$$

$$\theta_{xy} = k \cdot L = \frac{BL}{2B\rho}, \quad (2.3)$$

where $S = D + L + D$ is the length of the cell.

Non-diagonal blocks of the matrix of the above cell are not zero, indicating that the solenoid will introduce coupling of X and Y spaces at the exit of the cell. To eliminate the coupling, we chose a configuration for each cell such that 30 degree rotation in xy space was achieved, and an overall 90 degree xy rotation was achieved for the whole channel. Therefore, couplings in xy space are canceled out through exchanges of xy emittances. The corresponding transfer matrix is then in the form of

$$R_{total} = \begin{pmatrix} 0 & 0 & -a & -b \\ 0 & 0 & -c & -d \\ a & b & 0 & 0 \\ c & d & 0 & 0 \end{pmatrix},$$

where a, b, c and d are non-zero elements in terms of D and k.

In case of an even number of solenoids instead of odd number, the solenoids could be conveniently powered with alternated polarity so that the overall xy rotation is canceled out.

As there is a drift in each cell, the phase advance of each cell is greater than the rotation in xy space. Following Equation (2.1) and (2.3), our choice of 90 degree rotation in xy space will satisfy the criteria for effective collimation, as stated at the beginning.

The key design elements are summarized below:

- each cell is in the configuration of drift-solenoid-drift, 3 cells in total,
- each cell has a 30 degree xy rotation, 90 degrees in total,
- eigen beta $\bar{\beta} = 1.05$ m for each cell.

2.2 Collimation Channel Parameters

With respect to the key design elements listed above, the channel parameters were then calculated according to Equation (2.1), Equation (2.2), and Equation (2.3), for $^{40}\text{Ar}^{7+}$ beam with magnetic rigidity $B\rho = 0.538$ T·m. These channel parameters are summarized below:

- yoke length of each solenoid $L_{sol} = 0.428$ m,
- length of drift on each side of cell $L_{drift} = 0.141$ m,
- length of each cell $L_{cell} = 0.710$ m,
- overall length of channel $L_{channel} = 2.130$ m,
- magnetic field needed in solenoids $B = 0.132$ T ,
- phase advance $\sigma = 38$ degrees per cell,
- rotation in xy space $\theta_{xy} = 30$ degrees per cell,
- eigen beta $\bar{\beta} = 1.05$ m per cell.

A sketch of the design is shown in Figure 2.1.

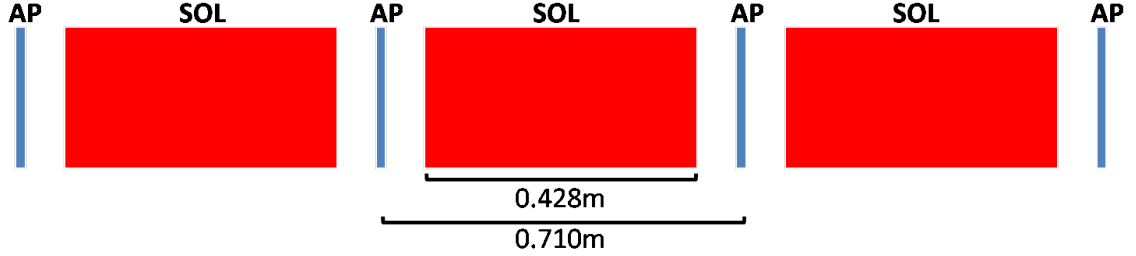


Figure 2.1: Illustration of the designed collimation channel. The channel consists of 3 solenoids (SOL) and 4 apertures (AP). The cell consists of one solenoid and two drifts on both end, equaling 0.710 m in length each. The designed collimation channel has a total length of 2.310 m.

2.3 Beam Simulation

To validate our design, we performed simulations of the beam with a simulation code written in Matlab. A $^{40}\text{Ar}^{7+}$ beam extracted from the ECR source with 24.43 kV extraction voltage was used in the simulation. The corresponding energy of the beam was $E=428$ KeV/nucleon and the magnetic rigidity was $B\rho = 0.0538$ T·m.

2.3.1 Verification of Basic Functionality

To check the rotation in xy space, we tracked the envelopes of the Argon beam; The envelopes were round in xx' and yy' phase spaces, but with asymmetric emittances through the channel(Figure 2.2). Compared to the envelope at the entrance of the first cell, the envelope at the exit of the channel confirms a 90 degree rotation in xy space. The corresponding exchange in X and Y emittances is observed when looking at the emittances through the channel (Figure 2.3).

To check the phase advance in phase space, we tracked the envelopes of a mismatched $^{40}\text{Ar}^{7+}$ beam through the channel. The results of the simulation are shown in Figure 2.4, where beam envelopes are shown in xx' , yy' and xy spaces respectively at the entrance and exit of the three successive solenoid cells. As stated in the channel

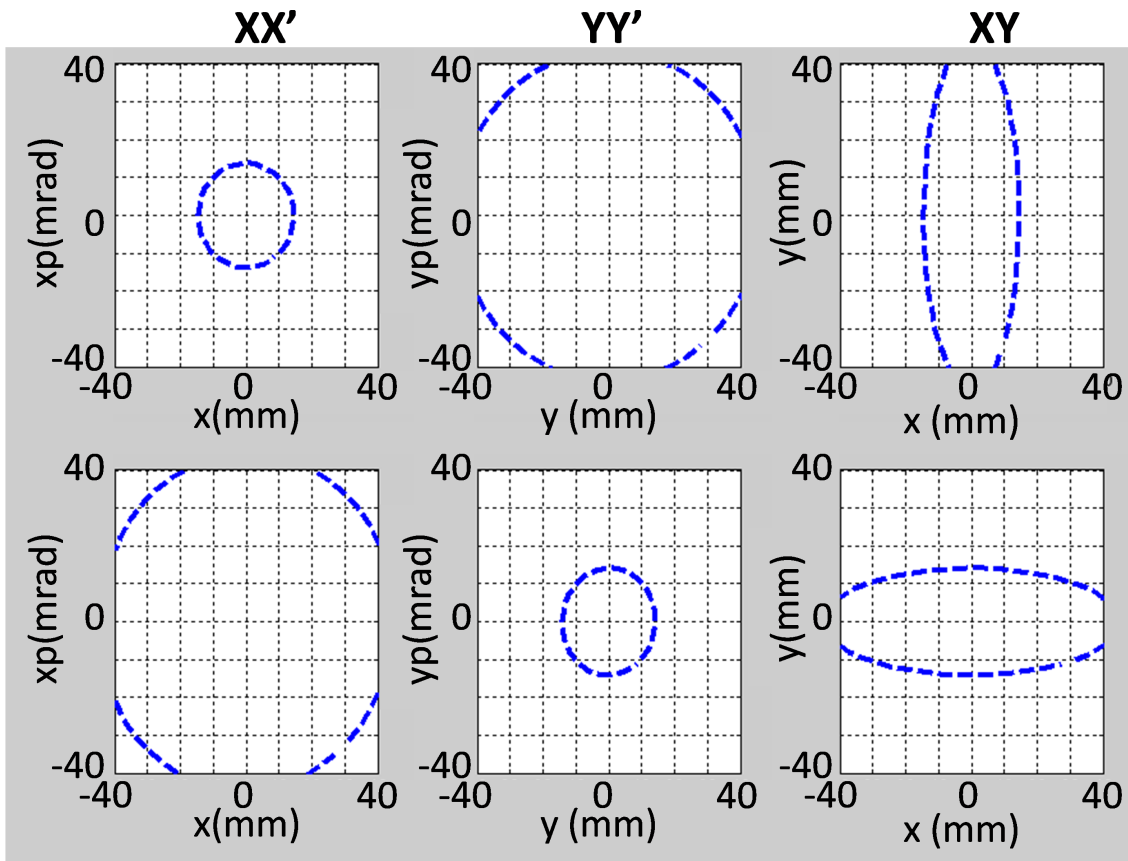


Figure 2.2: Overall 90 degree rotation in xy space was confirmed by tracking a beam with asymmetric X and Y emittances. Beam envelopes are shown in xx' , yy' and xy spaces respectively at the entrance and exit of the three successive solenoid cells. The X and Y emittances have been exchanged and the 90 degree rotation in xy space can also be observed.

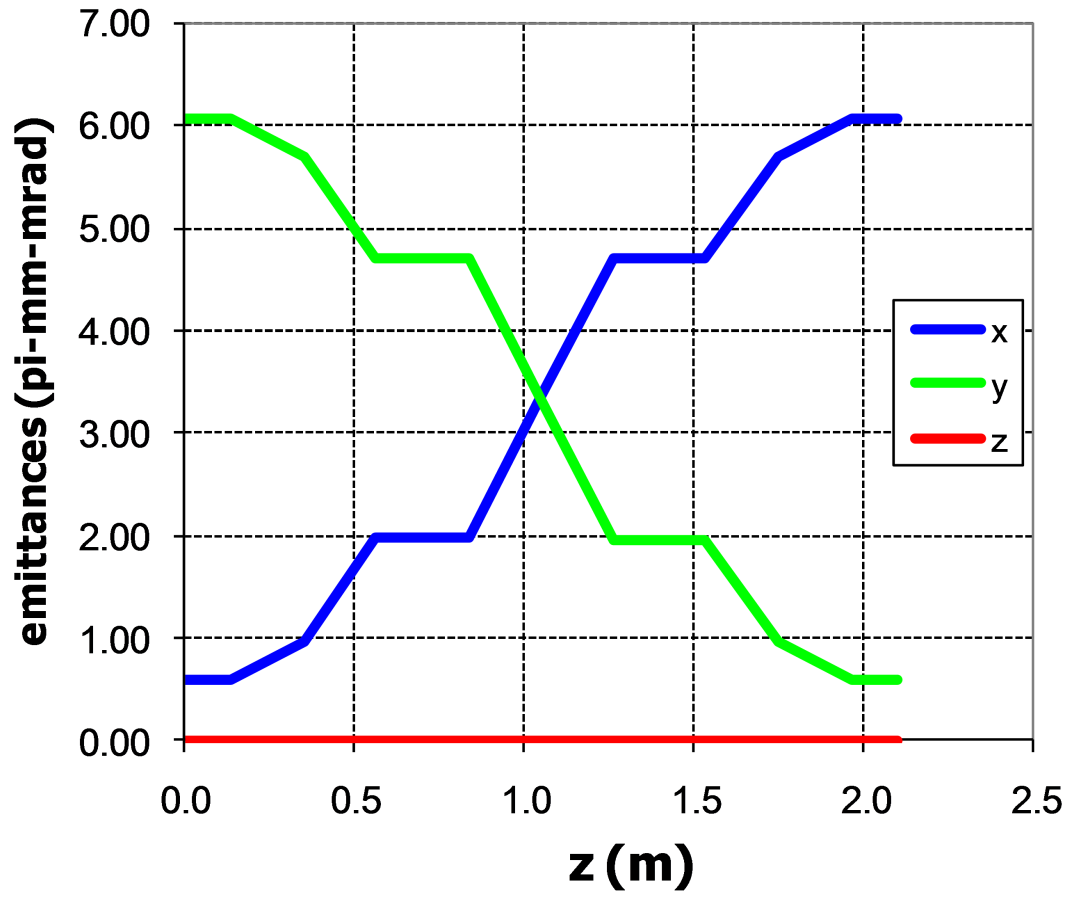


Figure 2.3: Emittances in xx' and yy' phase spaces through the collimation channel. The emittance exchange was observed.

parameter, a 38 degree rotation in phase space for each of the cells, and an overall 115 degree rotation in total are achieved.

To check the collimation process, we tracked the Argon beam with $200 \pi\text{-mm}\cdot\text{mrad}$ vertical and horizontal emittances and negligible longitudinal emittance through the channel. 5000 particles in a 6D Waterbag distribution with initial Twiss parameters ($\alpha = 0, \beta = 1.05 \text{ m}$) were used. All the solenoids were set at $B=0.131 \text{ T}$ and all apertures had 15 mm width, which corresponded to an overall 90 degree xy space rotation, average beta of 1.047 m, and an acceptance of $56 \pi\text{-mm}\cdot\text{mrad}$ from Equation (2.4). The result of the simulation is shown in Figure 2.5, where particles (blue dots) and beam envelopes without collimation (dashed ellipses) are both presented for comparison. Shown are particles and beam envelopes in xx', yy' and xy spaces at the entrance and after the four successive collimators. Clearly, the collimation process is successful, and a round beam was extracted from the channel. The RMS normalized emittances along the channel are shown in Figure 2.6, illustrating the four cuts.

With the same beam, i.e. transverse Twiss parameter of ($\alpha = 0, \beta = 1.05 \text{ m}, \epsilon = 200 \pi\text{-mm}\cdot\text{mrad}$) and negligible longitudinal emittance, we checked the collimation process with different aperture openings, ranging from 5 mm to 40 mm, with 10000 particles. In each aperture case, 2D RMS emittances $\epsilon_{xx'}$ and $\epsilon_{yy'}$ and 4D RMS emittance $\epsilon_{xx'yy'}$ were calculated for particles that pass successfully through the channel. The transmission rate and the brightness, which is defined as $N_{particles}/\epsilon_{xx'yy'}$, were calculated. Results are shown in Figure 2.7. Clearly the emittance decreases when the apertures are closed, while the brightness increases, illustrating the capability to effectively collimate the beam to different emittances according to equation (2.4) while increasing the beam quality.

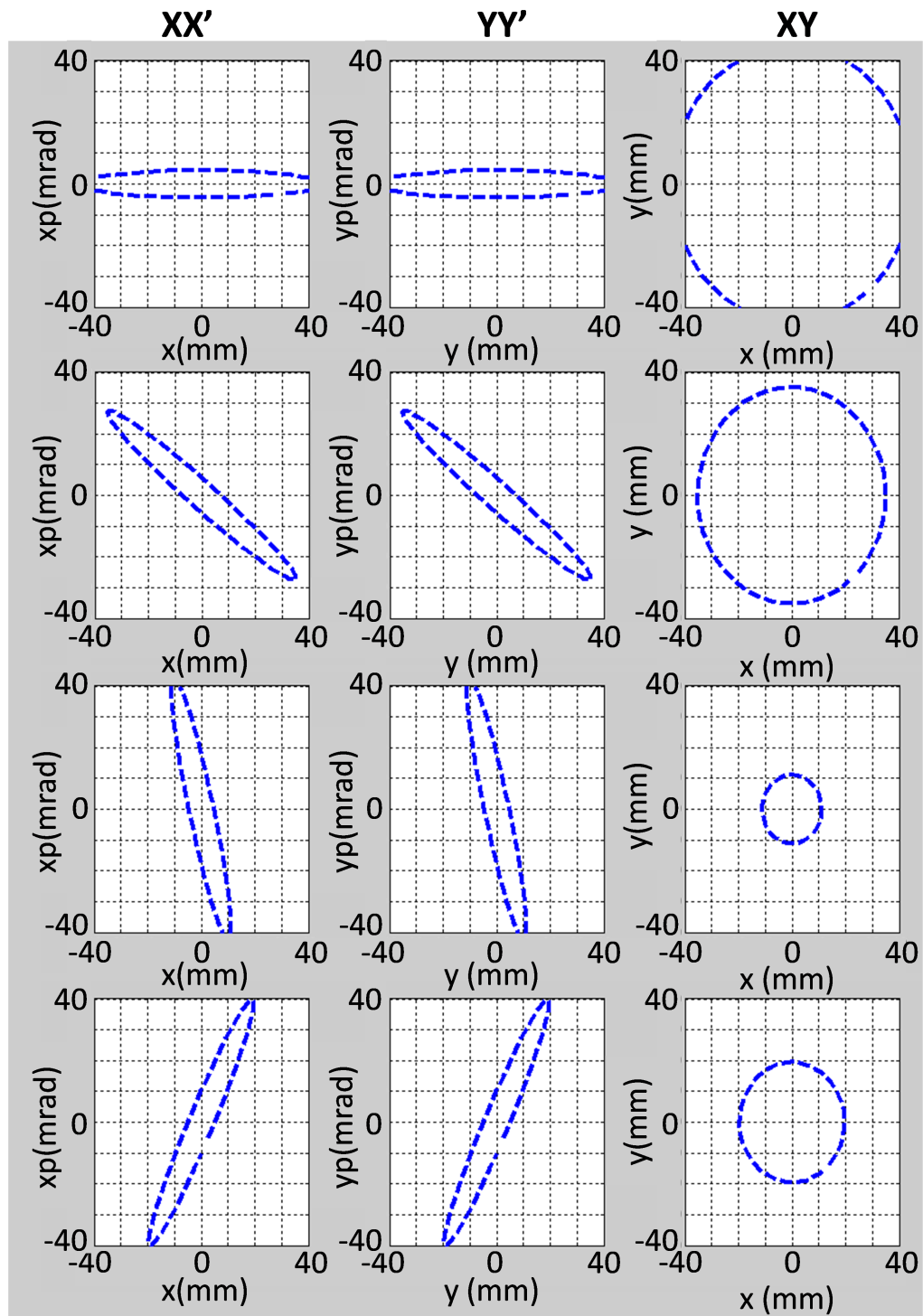


Figure 2.4: Overall 115 degree phase advance confirmed by a mismatched beam. Beam envelopes are shown in xx' , yy' and xy spaces respectively at the entrance and exit of the three successive solenoid cells.

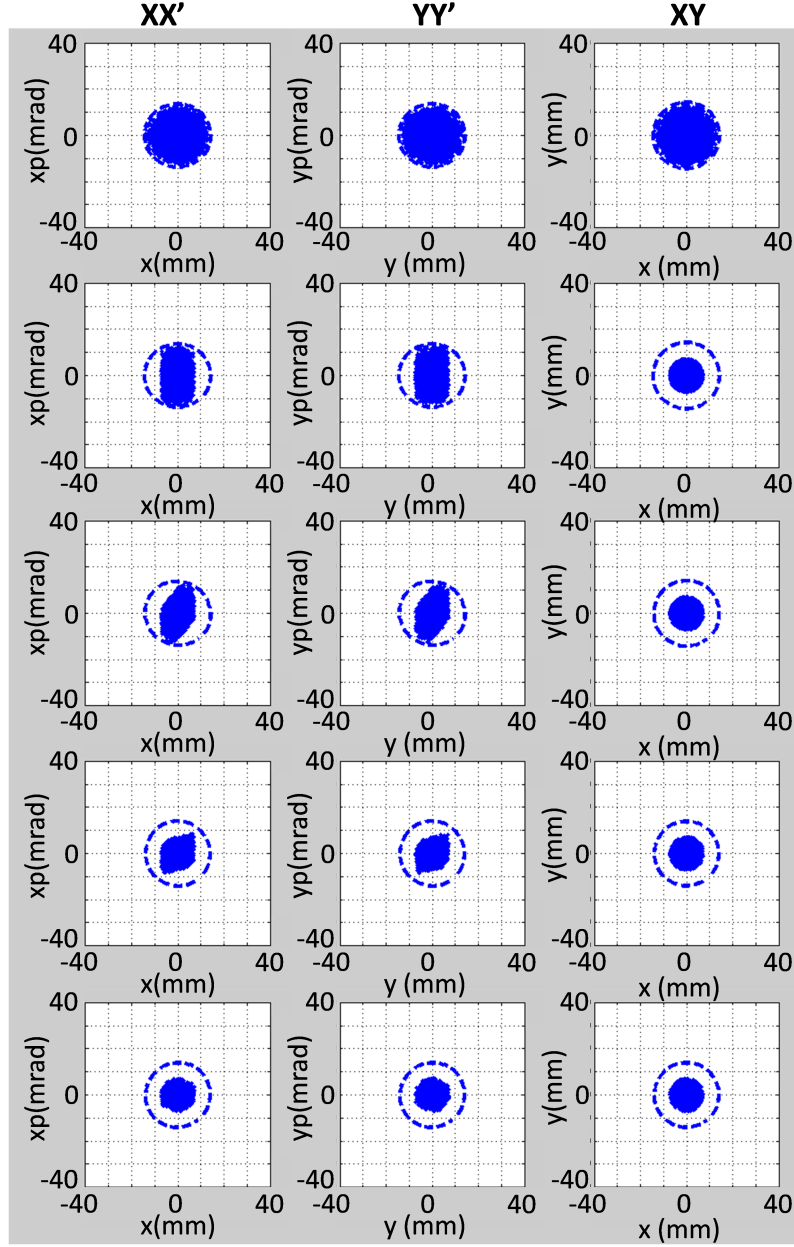


Figure 2.5: Particle tracking through the collimation channel. 5000 $^{40}\text{Ar}^{7+}$ particles with ECR extraction voltage 24.4 kV ; 6-D waterbag distribution was used. Initial Twiss parameters for both horizontal and vertical directions were $(\alpha = 0, \beta = 1.05 \text{ m}, \epsilon = 200 \pi \cdot \text{mm} \cdot \text{mrad})$, with negligible longitudinal emittance. All the solenoids were set at 0.131 T field level and all apertures 15 mm width, which corresponded to an overall 90 degree xy space rotation and an acceptance of $56 \pi \cdot \text{mm} \cdot \text{mrad}$. Particles (blue dots) and beam envelope without collimation (dashed ellipses) are both presented for comparison, and are shown in xx' , yy' and xy spaces respectively at the entrance and after the four successive collimators. The collimation process could be clearly observed.

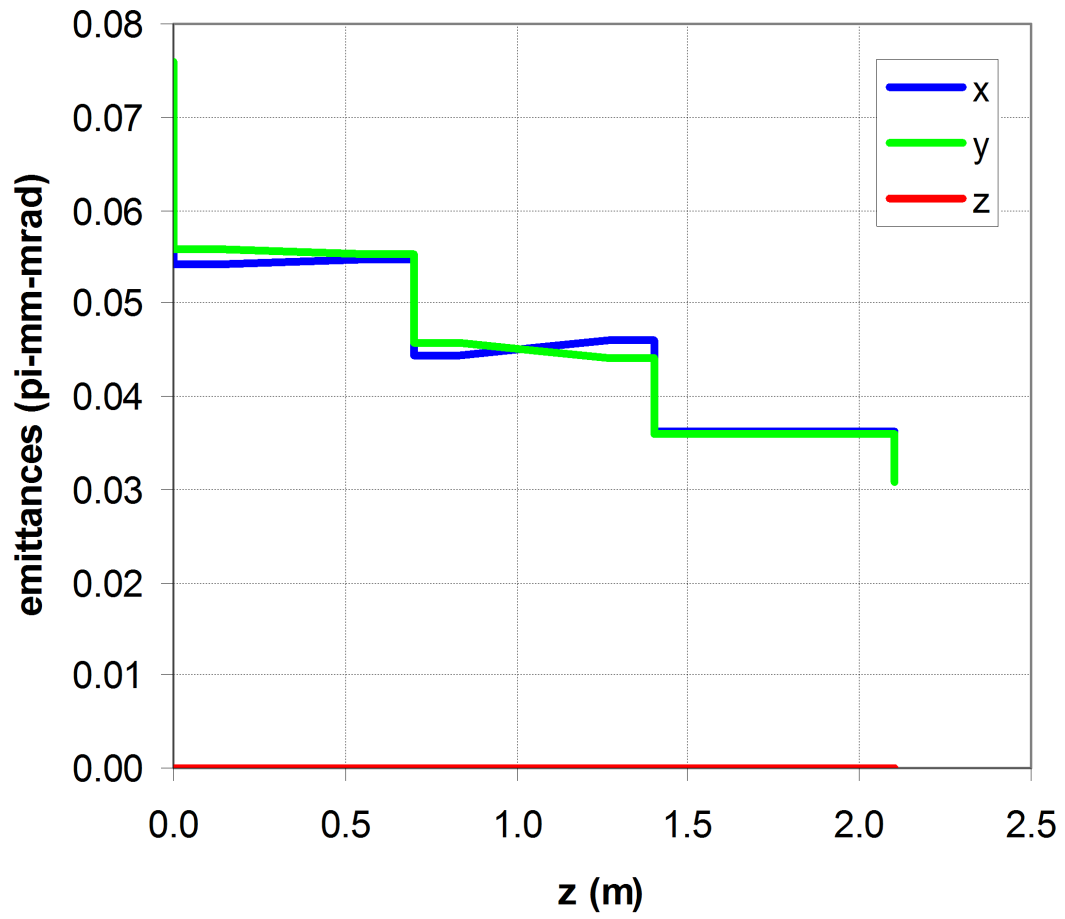


Figure 2.6: RMS normalized emittances through the collimation channel illustrating the four cuts.

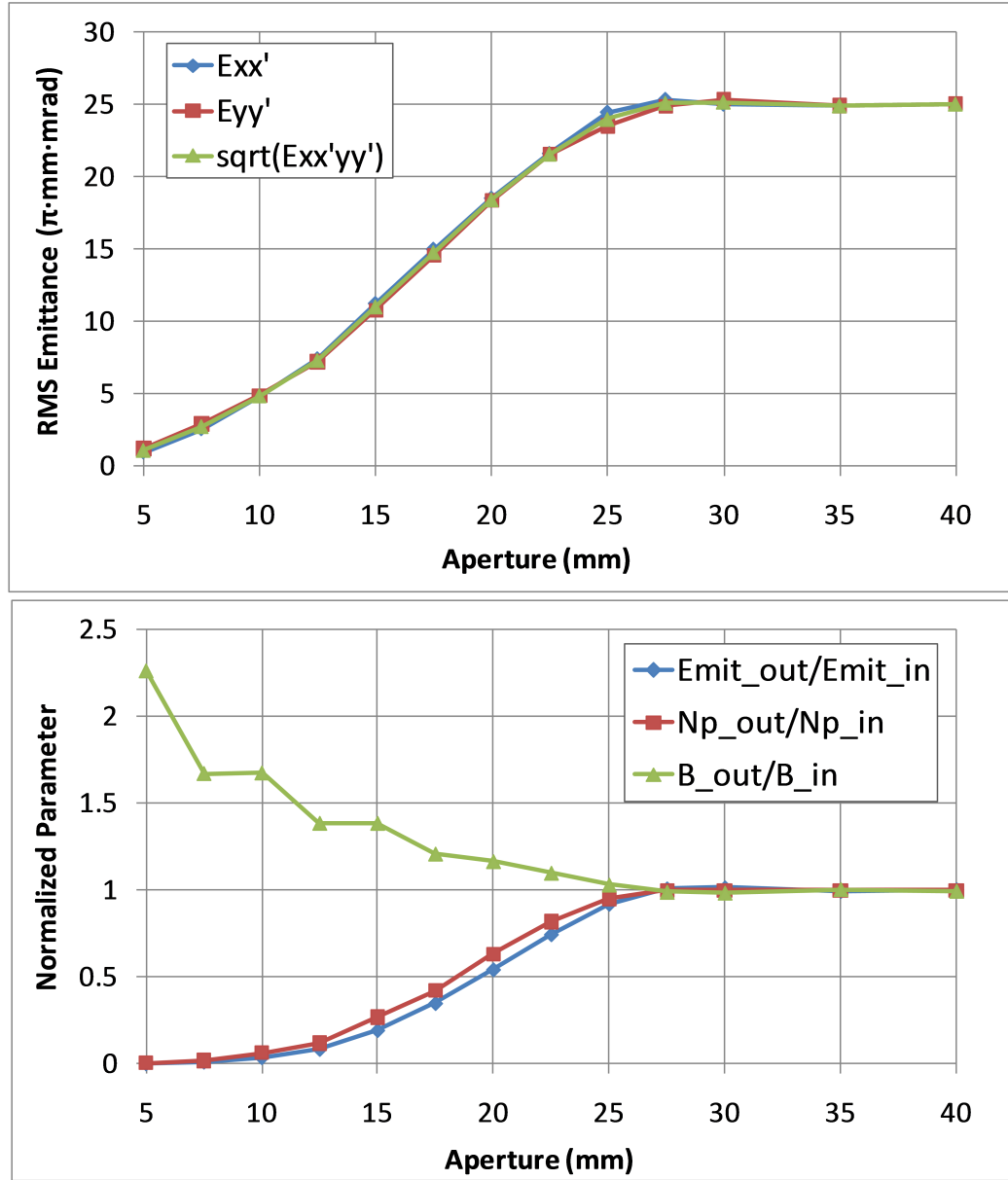


Figure 2.7: RMS emittances (top) and other normalized parameters (bottom) of Argon beam at the end of the collimation channel with different apertures. In the top plot, 2D beam RMS emittances $\epsilon_{xx'}$ (blue) and $\epsilon_{yy'}$ (red) and square root of 4D RMS emittance $\epsilon_{xx'yy'}$ (green) are displayed for particles that survived through the channel; in the bottom, normalized ratios of input and output emittances (blue), number of particles (red), and brightness (green) through the channel for each aperture are displayed. Clearly, we can see that 2D and 4D emittances decrease as the apertures shrink, while brightness increases, demonstrating the capability to effectively collimate beam to different emittances while increasing the beam quality.

2.3.2 Tuning Recipe

The designed channel has a clear tuning procedure: first, set the current of solenoids so that a beam with a given magnetic rigidity ($B\rho$) achieves a 90 degree xy space rotation; second, set the four apertures to the desired opening. Under the premise that the beam is matched to the channel, the emittance at the end of the channel (A) will be:

$$A = \frac{D^2}{4\bar{\beta}}, \quad (2.4)$$

where $\bar{\beta}$ is the average β function of the channel, and D is the full width of the aperture opening. The desired emittances at the end are then regarded as the acceptance of the channel.

We have made a simple spreadsheet (Figure 2.8) to facilitate the tuning process. In the left hand side table, the current of the solenoid, selecting magnet upstream and the bending magnets downstream are calculated by inputting the charge state and mass of the ions, and the corresponding extraction voltage of SuSI. In the table on the right, the aperture openings and the corresponding channel acceptances are listed, according to Equation (2.4).

Q	7	Correspondance between apertures setting and collimation channel acceptance: Apertures =Slits= 7.5 mm - Acceptance = 14 pi.mm.mrad Apertures =Slits= 10 mm - Acceptance = 25 pi.mm.mrad Apertures =Slits= 15 mm - Acceptance = 56 pi.mm.mrad Apertures =Slits= 25 mm - Acceptance = 156 pi.mm.mrad Apertures =Slits= 50 mm - Acceptance = 625 pi.mm.mrad
A	40	
V_ECR	24.43 kV	
Q005DS	119.2 A	
I_Solenoids	69.1 A	
Q17DS-Q25DS	168.9 A	
Brho	0.0538 T-m	

Figure 2.8: Channel tuning recipe. In the table on the left, the charge state and mass of the ion and the extraction voltage of SuSI are inputs. The current for all the solenoids, selecting magnet upstream (Q005DS) and the bending magnets downstream (Q17DS and Q25DS) are then calculated. In the table on the right, the corresponding emittances-which are also channel acceptances-are listed with different aperture openings according to Equation (2.4)

2.3.3 Flexibility of Channel Design For Mismatched Beams

The designed channel has the flexibility to collimate beams that are not matched to the channel. However, the collimation efficiency for mismatched beams is not optimum if the above mentioned tuning recipe, i.e. setting all solenoids to the same field level and apertures to the same opening, is used.

To show the drop of the efficiency, a simulation of 10000 Ar^{7+} particles and a $56 \pi \cdot \text{mm} \cdot \text{mrad}$ channel acceptance was done. 2D RMS emittances in xx' and yy' spaces, square root of 4D RMS emittance in $xx' yy'$, transmission rate and the brightness were calculated at the end of collimation channel for different input beam Twiss parameters; α and β were varied respectively, while the constant one was set to the matched value. Results are shown in Figure 2.9 for varying alpha and Figure 2.10 for varying beta. In both cases, the emittance at the end of the channel was within the channel acceptance, demonstrating the capability of collimation for mismatched beams. However, only the beam injected with matched Twiss parameters ($\alpha = 0, \beta = 1.05 \text{ m}$) achieved the highest brightness, reflecting the most efficient collimation; the collimation efficiency for beams mismatched to the channel decreased as the beam gets more and more mismatched.

One possible way to recuperate the collimation efficiency is to tailor the channel to the beam Twiss parameters. To do so, for a desired acceptance the beam is backtracked through the channel and the apertures are modified to follow the simulated beam size at each position of the aperture.

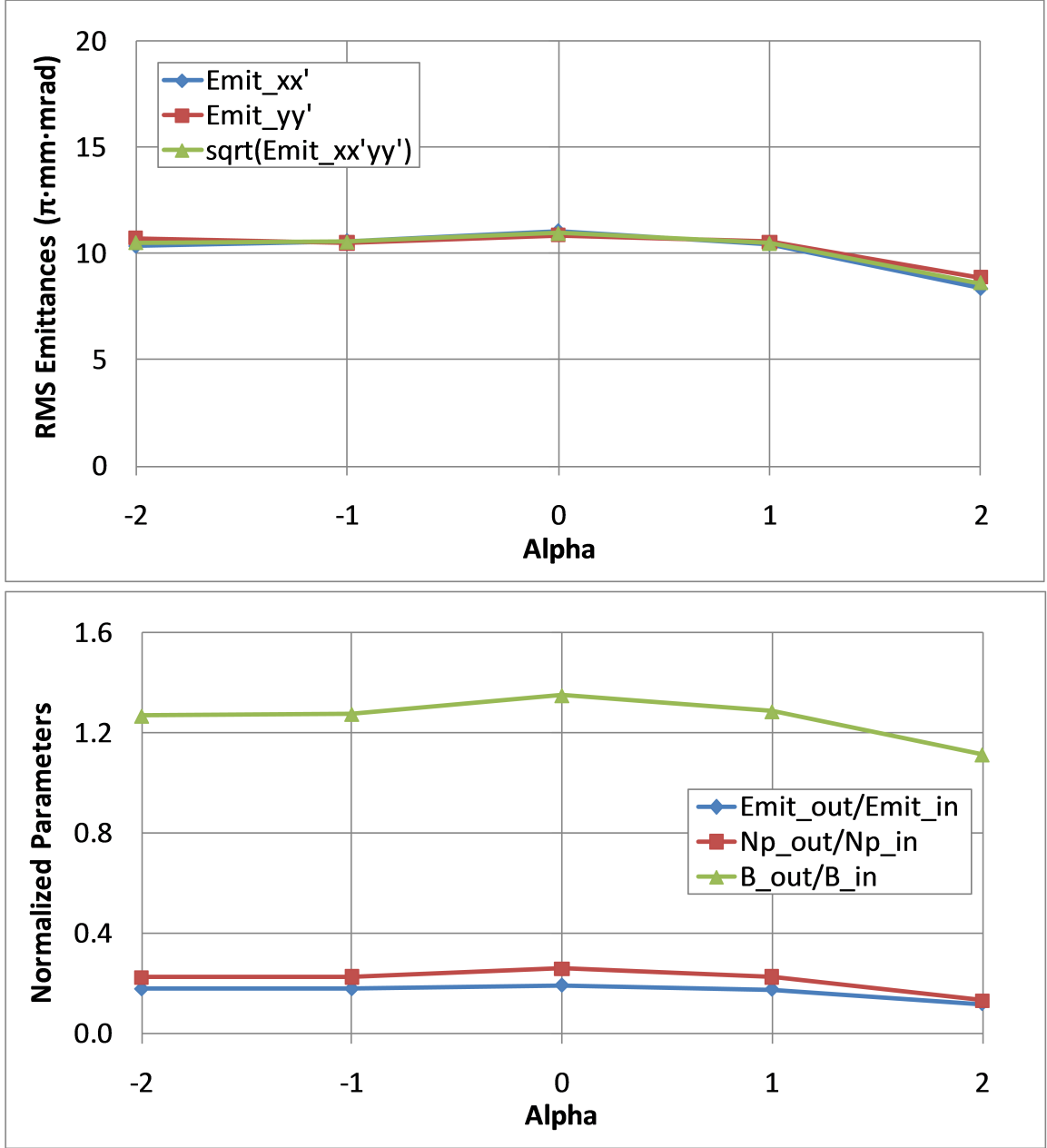


Figure 2.9: RMS emittances, normalized brightness and other normalized parameters of $^{40}\text{Ar}^{7+}$ beam injected with different α through the collimation channel with $56 \pi \cdot \text{mm} \cdot \text{mrad}$ channel acceptance. β was set to 1.05 m. 2D beam RMS emittances $\epsilon_{xx'}$ (blue) and $\epsilon_{yy'}$ (red) and square root of 4D RMS emittance $\epsilon_{xx'yy'}$ (green) are displayed in the upper plot, where the emittances are all within the channel acceptance; normalized ratios of input and output emittances (blue), number of particles (red), and brightness (green) through the channel are displayed in the lower plot, where the beam injected with matched Twiss parameters ($\alpha = 0, \beta = 1.05 \text{ m}$) had the highest brightness.

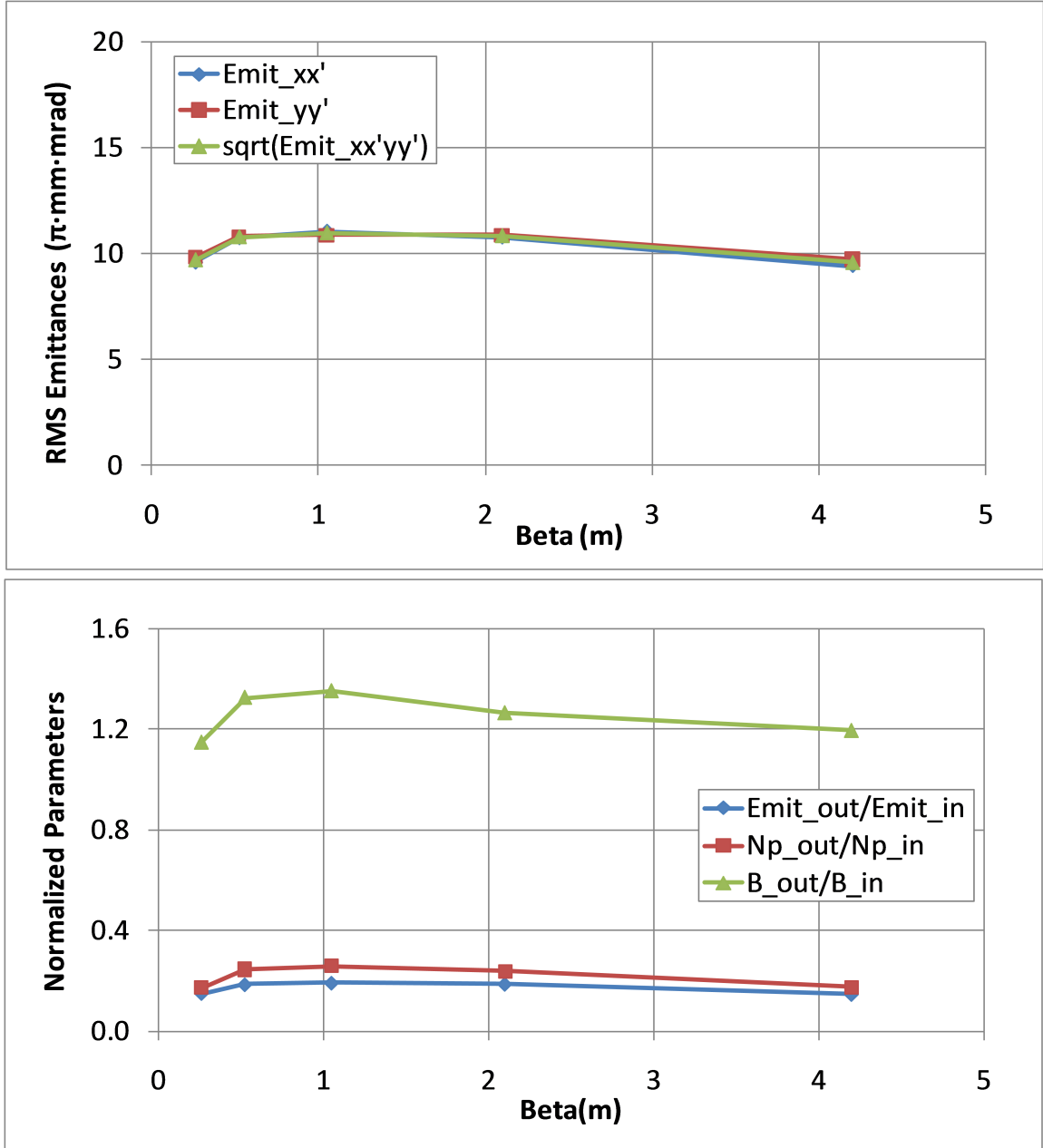


Figure 2.10: RMS emittances, normalized brightness and other normalized parameters of $^{40}\text{Ar}^{7+}$ beam injected with different β through the collimation channel with $56 \pi \cdot \text{mm} \cdot \text{mrad}$ channel acceptance. α was set to 0. 2D beam RMS emittances $\epsilon_{xx'}$ (blue) and $\epsilon_{yy'}$ (red) and square root of 4D RMS emittance $\epsilon_{xx'yy'}$ (green) are displayed in the upper plot, where the emittances are all within the channel acceptance; normalized ratios of input and output emittances (blue), number of particles (red), and brightness (green) through the channel are displayed in the lower plot, where the beam injected with matched Twiss parameters ($\alpha = 0, \beta = 1.05 \text{ m}$) had the highest brightness.

Chapter 3

EMITTANCE COLLIMATION CHANNEL IMPLEMENTATION

3.1 Hardware Description

3.1.1 Solenoid

Three identical solenoids are used in the collimation channel to rotate the beam in transverse phase spaces progressively with successive collimation performed in between. Preferably, each solenoid rotates the phase spaces by 30 degrees. Each of the solenoids has a flange to flange length of 25 inches, with a yoke of 17 inches. The beam tube is 2 inches in size radially. The solenoid has in total 12 layers of winding, and each layer has 55 turns of copper wire, resulting in 660 turns in total. The basic parameters of these solenoids are summarized in Table 3.1. An engineering model and a picture are shown in Figure 3.1. To protect the hardware, the current limit is set to 110 A for each of these solenoids.

Flange to flange length	25'' = 0.6350 m
Yoke length	17'' = 0.4318 m
Beam tube radial aperture	2'' = 0.0508 m
Total number of turns	660
Number of layers	12
Number of turns per layer	55

Table 3.1: Basic parameters of the solenoid used in SuSI collimation beam line

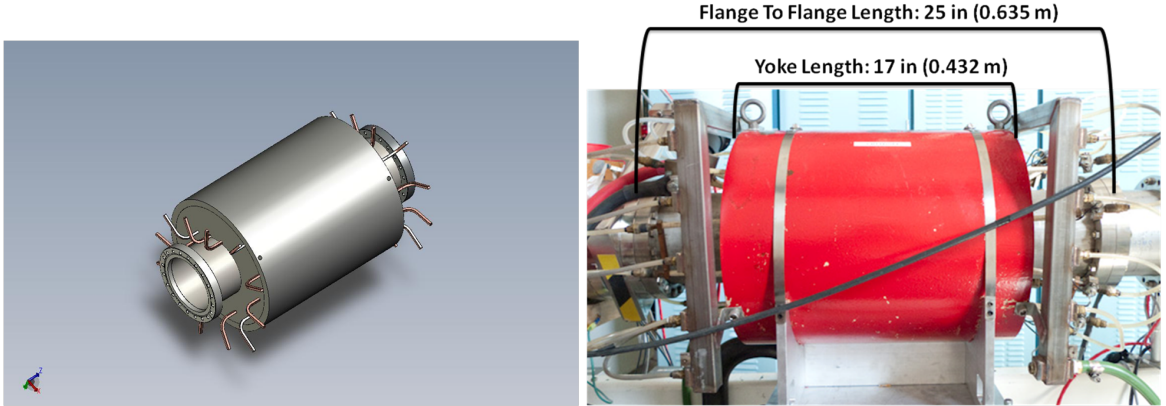


Figure 3.1: Engineering model (left) and picture (right) of the solenoid used in collimation channel.

3.1.2 Steering Magnet

Two steering magnets are used before the collimation channel on both sides of the selecting magnet to adjust the direction of the beam. Each of the steering magnets consists of four plates, and each plate is made of a steel core with two copper wire windings around it. An engineering model of the steering magnet is shown in Figure 3.2.

During operation, the opposite two plates are controlled together. The top and bottom plates will kick the beam vertically and the left and right plates will kick the beam horizontally. Prior to use, the steering magnet needs to be calibrated for beams with different magnetic rigidities, and the process is elaborated upon in Section 4.3.1.

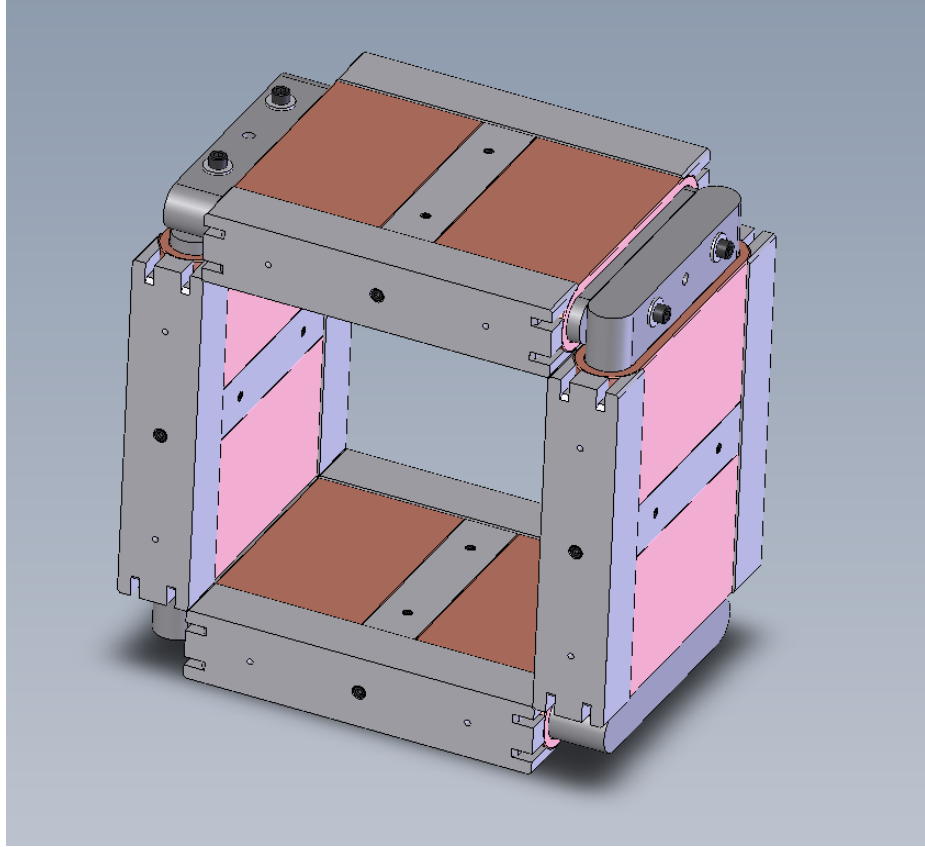


Figure 3.2: Engineering model of the steering magnet.

3.1.3 4-Jaw Slit System

Two 4-Jaw slits systems capable of creating square apertures with various sizes are used in our collimation channel. They serve as both collimator and diagnostic instruments. One is installed in the diagnostic box at the entrance of the channel, another in the diagnostic box at the exit. Each jaw is made of copper and connected to a stepper motor that can have a step size as small as 1 mm. To remove the heat from the energy loss of beam on the slits, cooling water can be circulated through each jaw. An engineering model of the 4-jaw slits system is shown in Figure 3.3. A faraday cup is also shown in this figure.

In operation, the 4 jaws are divided into horizontal and vertical sets. Therefore, square apertures of different size can be created to serve as collimators at different

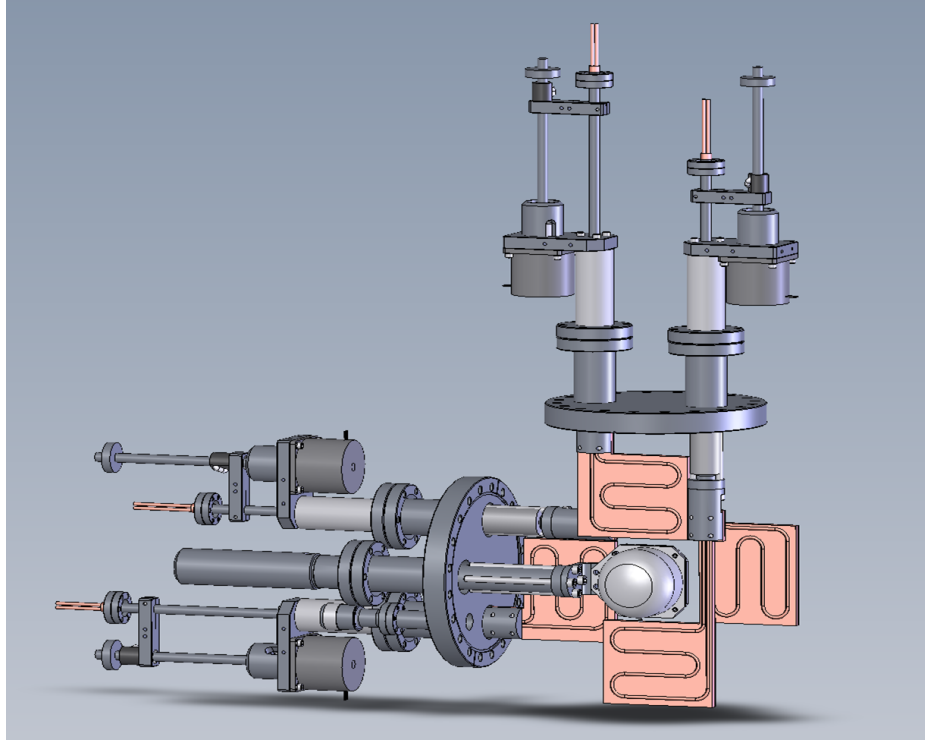


Figure 3.3: 4-Jaw slits system with faraday cup.

transverse position in the beam tube. Each jaw can move as much as 70 mm. To add flexibility to the control, local control boxes are installed on the beam line railing for each jaw, as shown in Figure 3.4

In combination with the faraday cup placed downstream of the slits, a fast measurement of the current distribution can be performed by scanning the space transversely with a square aperture created by the 4 jaws. The resolution of the scan can be altered by changing the size of the square aperture and the step size that the aperture moves. Usually it takes less than 5 minutes to perform a scan of sufficient accuracy. An example of such scan is shown in Figure 3.5, where the image on the beam viewer is also shown for comparison.

In addition, a 4D transverse phase space distribution of the beam can be measured by scanning the two sets of 4-jaw system iteratively and record the current on the faraday cup. For every xy position defined by the first 4-jaw system, a full space xy

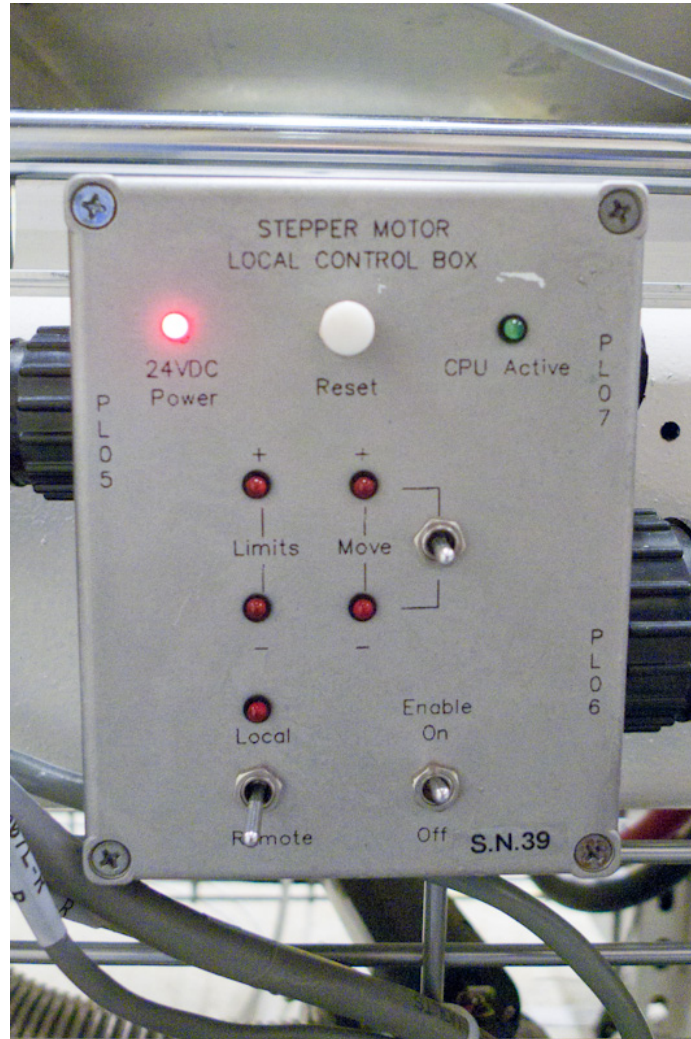


Figure 3.4: Local control box, one for each jaw of the 4-Jaw slits system, installed on the beam line railing.

scan is done at the second 4-jaw system, effectively measuring the $x'y'$ distribution of the beam for each xy location and generating a full 4D $xyx'y'$ measurement. Depending on the resolution, it usually takes more than 45 minutes to complete a full 4D scan. Figure 3.6 is an example of the 4D phase space scan, where beam distributions on each 2D projection plane of the 4D volume is shown.

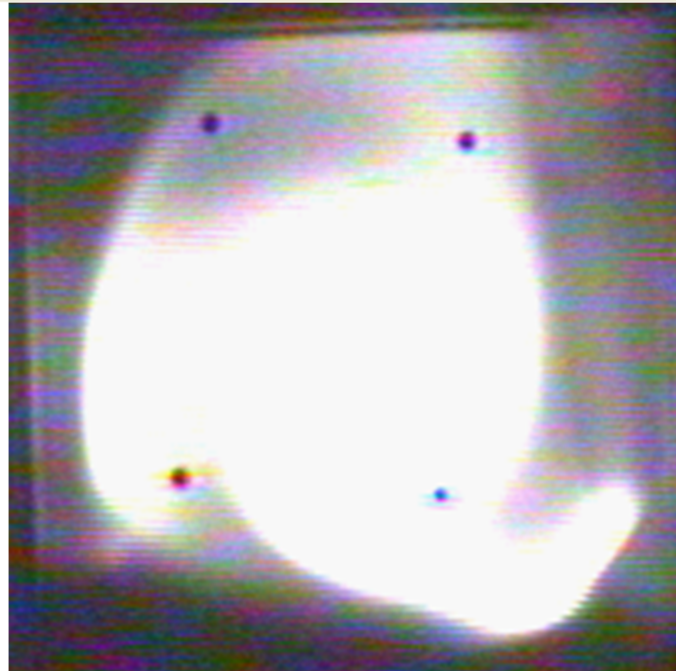
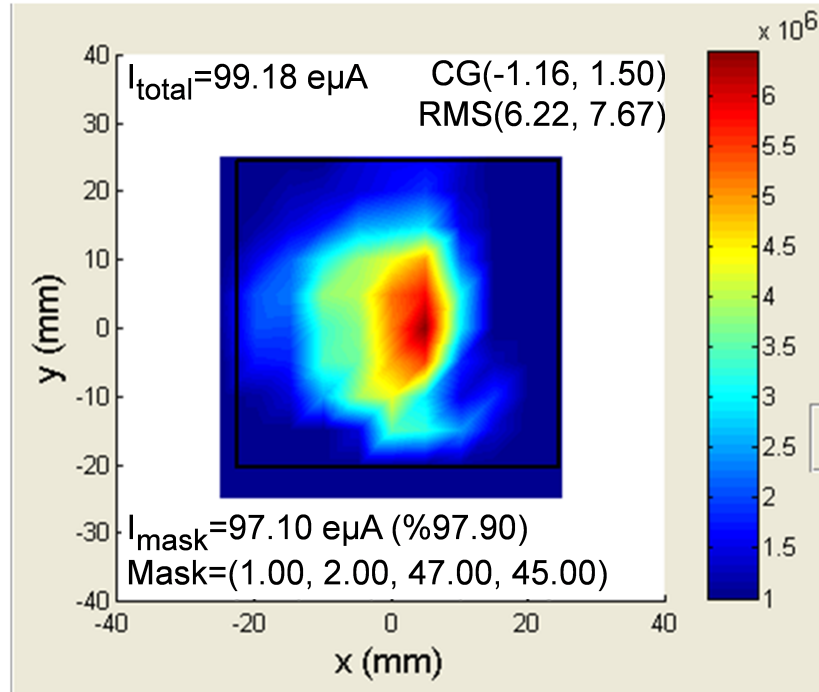


Figure 3.5: Example of the current distribution of the beam measured by 4-Jaw slit system (top). The image on the beam viewer is also shown for comparison on the bottom.

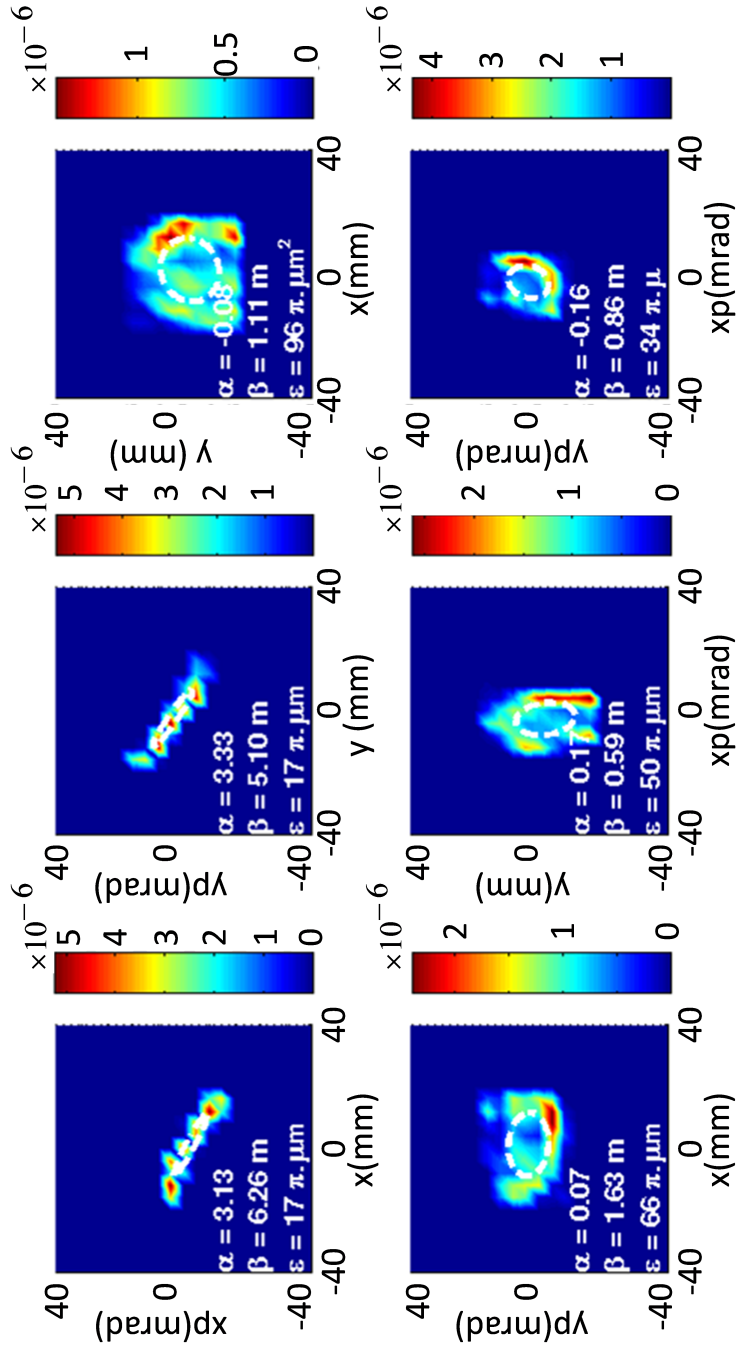


Figure 3.6: Example of the 4D phase space scan by the 4-Jaw slit systems, where beam distribution on each 2D projection plane of the 4D volume is shown. In the top row, from left to right are beam distributions in xx' , yy' and zz' spaces; in the bottom row, from left to right are beam distributions in xy' , $x'y$ and $x'y'$ spaces. The rms ellipses and rms Twiss parameters are shown as well.

3.1.4 Circular Aperture

Aperture systems that are capable of using five different aperture sizes are used as collimators. They are mounted on both sides of the middle solenoid. Aperture openings are drilled on 3 collimation plates. One fixed collimation plate, which contains an aperture with a diameter of 50 mm, is mounted at the entrance flange of the system; the four other apertures are drilled on two retractable collimation plates mounted on the aperture holders in the upper and lower cavity. One plate contains apertures with 25 mm and 15 mm in diameter, and the other contains apertures with 10 mm and 7.5 mm. Each aperture holder is connected to a pressurized air controlled multi-position cylinder, enabling the switch between the five apertures. Figure 3.7 shows an engineering model of the aperture system in isometric and cross-sectional view.

The aperture system has the advantage that the two collimation plates mounted on the aperture holders can easily be replaced with other plates that contain different aperture sizes without having to remove the central flange and affecting the alignment. This will save time and work in the future when beam collimation studies will be performed for a machine like FRIB that has a different acceptance than the CCF and will require other sets of apertures.

3.1.5 Beam Diagnostics

Several beam diagnostic instruments are employed in the channel, including faraday cups, beam viewers and Allison emittance scanners.

Faraday Cup

The faraday cup (FC) is an interceptive device for beam current measurement and is employed as one of our tools for beam diagnostics. Each FC has an opening of 2" and a depth of 1". To suppress the secondary electrons from exiting the cup, a

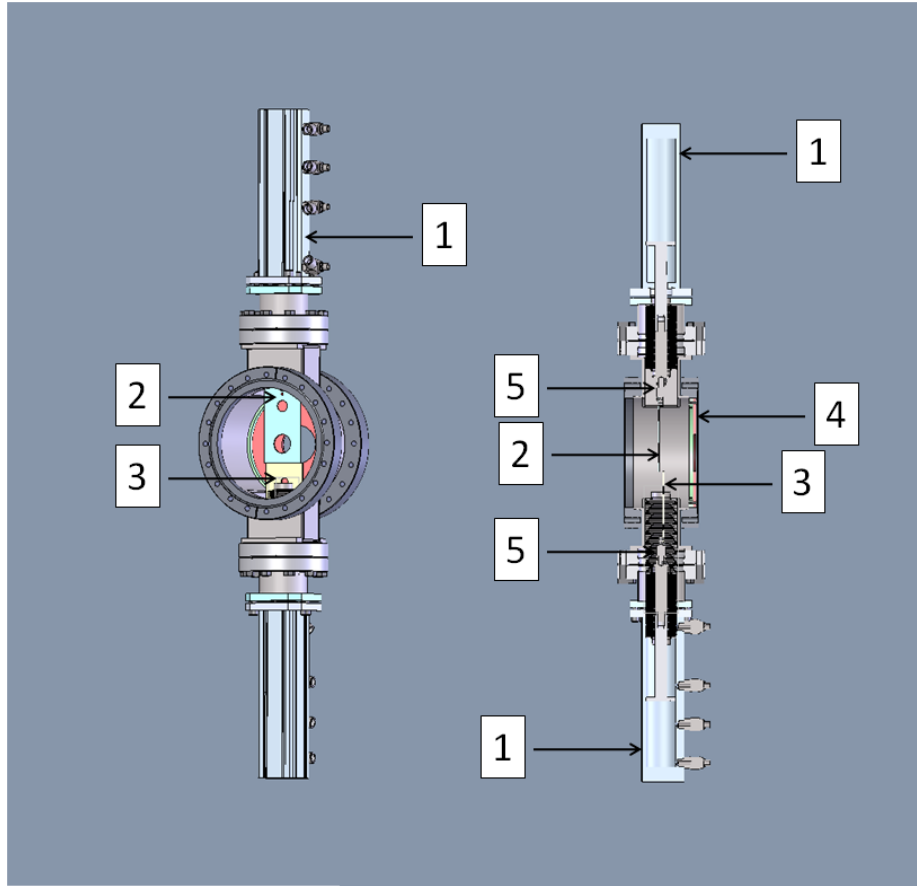


Figure 3.7: Isometric and cross-sectional view of the aperture system: (1) multi-position cylinder, (2) collimation plate containing apertures of 25 mm and 15 mm opening, (3) collimation plate containing apertures of 10 mm and 7.5 mm opening, (4) collimation plate containing apertures of 50 mm opening, (5) aperture holder.

suppressor ring is installed at the entrance of the FC with an applied voltage of -150 V. An engineering model of such a FC mounted on a motion feed is shown in Figure 3.8.

FCs are connected to analogue Keithley current meters and digitizers. In the latter, the analogue signal amplified by Keithley is converted to a digital signal that can be read by computer control software.

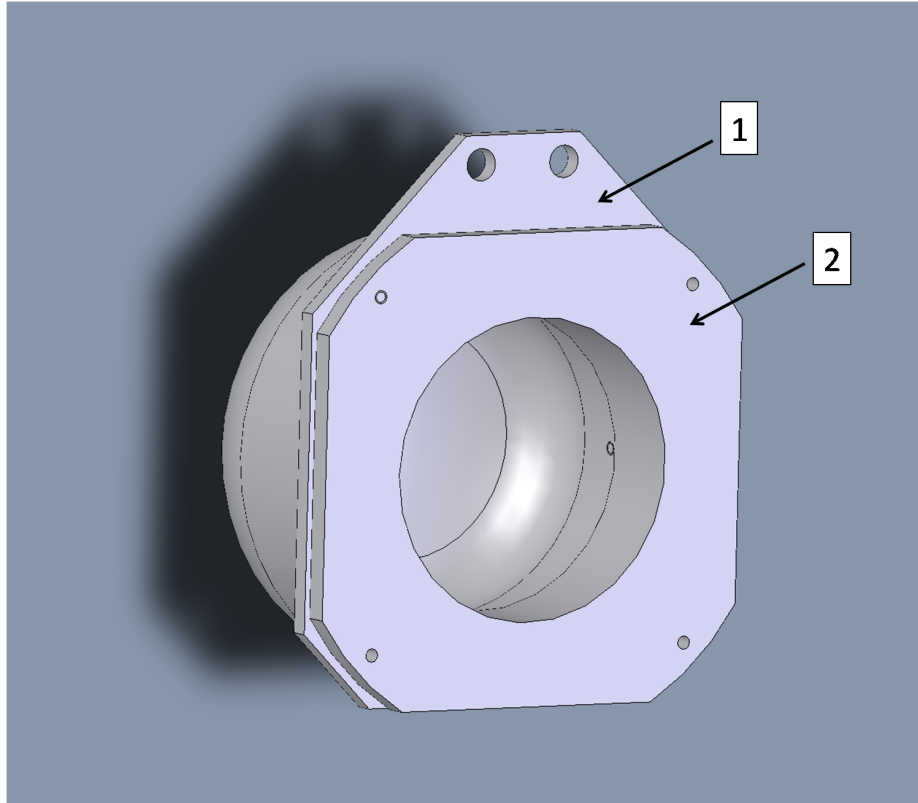


Figure 3.8: Engineering model of the faraday cup: (1) mounting plate, (2) suppressor ring.

Beam Viewer Plates

Beam viewer plates (VP) are interceptive devices used to image the shape of the beam when inserted into the beam path. The VPs are metal plates coated with potassium bromide (KBr) scintillating material. Each VP is 4" \times 4", with imprinted dots for reference. A picture of a VP is shown in Figure 3.9.

Allison Emittance Scanner

The Allison emittance scanner is an interceptive device used to measure the transverse emittance of the beam. The design of the NSCL Allison emittance scanner is based on a similar device operated at LBNL [29]. As shown in Figure 3.10, the emittance scanner box has entry and exit slits (S_1 and S_2) of 60 mm \times 0.2 mm each which are

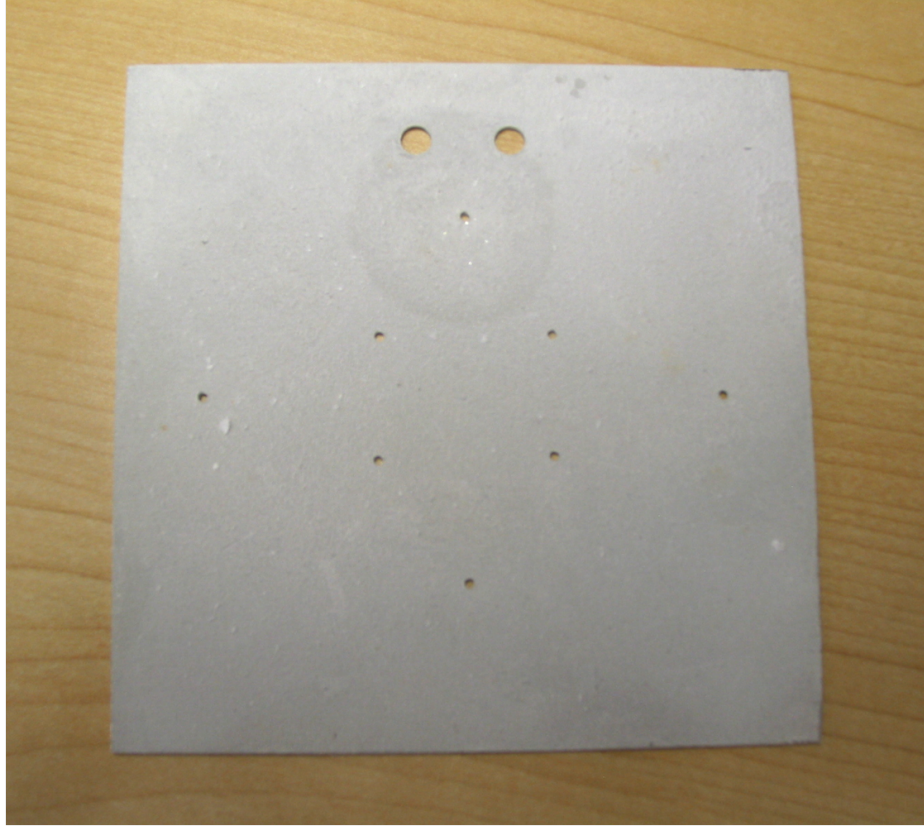


Figure 3.9: Picture of a beam viewer plate, where dots of 20 mm separation can be seen as well.

separated by a distance $D=75$ mm. Two deflecting voltage plates ($\pm V_p$) are mounted between the two slits, separated by a distance $g=12$ mm. A faraday cup is placed behind the exit slit measuring the beamlet current. Given the parameters defined above, the intrinsic position resolution is $\delta x_{int} = S_2 = 0.2$ mm, defined by the first slit, and the intrinsic angular resolution $x'_{int} = \pm \frac{S_2}{D} = \pm 2.7$ mrad.

A stepper motor drives the emittance box across the beam. At each position, the voltages on the plates are scanned to collect all beamlets at all possible angles, as shown in Figure 3.11.

The relation between the voltage on the plates (V_p) and the angle of the beamlet (x') is

$$V_p = x' \frac{2g}{D} V_{ECR} ,$$

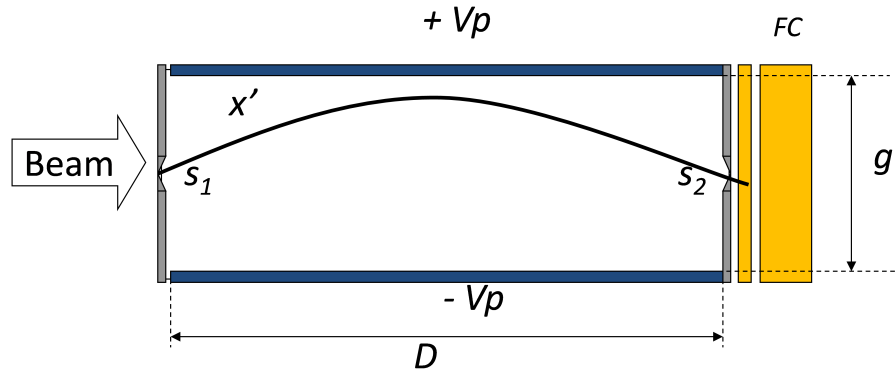


Figure 3.10: Scheme of the Allison emittance scanner box, which has entry and exit slits (S_1 and S_2) of $60 \text{ mm} \times 0.2 \text{ mm}$ each and separated by a distance $D = 75 \text{ mm}$. Two deflecting voltage plates ($\pm V_p$) are mounted between the two slits, separated by a distance $g = 12 \text{ mm}$. A faraday cup (FC) is behind the exit slits measuring beamlet current.

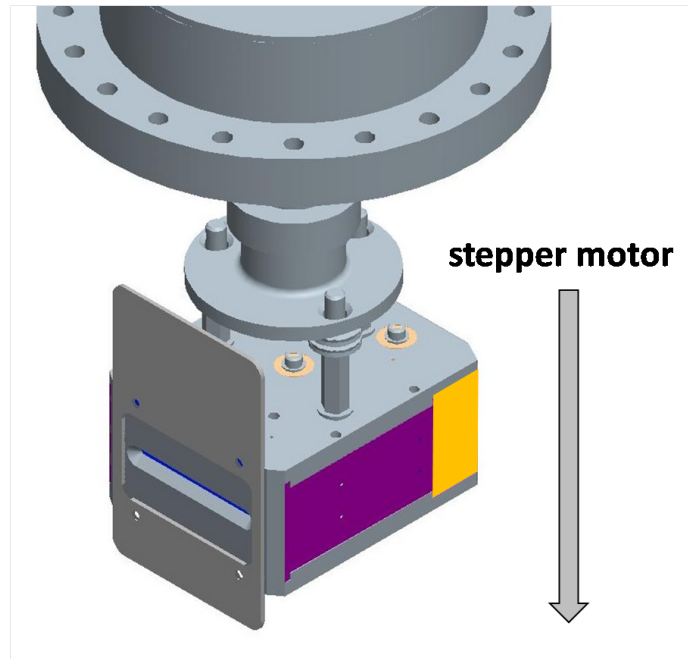


Figure 3.11: Mechanical drawing of the Allison emittance scanner. A stepper motor drives the emittance box across the beam. At each position, the voltages on the plates are scanned to collect all beamlets at all possible angles.

where V_{ECR} is the extraction voltage of the ECR ion source.

In operation, two Allison emittance scanners are placed perpendicular to each

other to enable independent measurement of the transverse phase space in x and y coordinates. The measurement uses a Labview interface and the raw data is processed by a Matlab code package called Post Processor, described in Section 4.2.3. The local control box installed on the beam line railing for each of the scanner is shown in Figure 3.12.

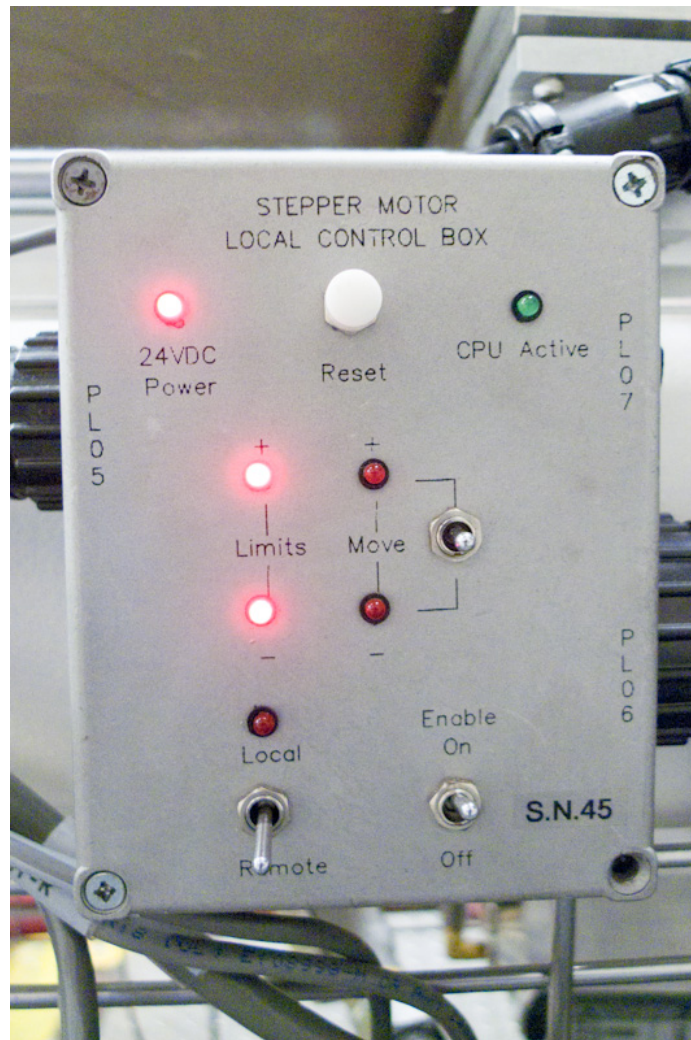


Figure 3.12: Local control box of the Allison emittance scanner installed on the beam line railing.

Beam Diagnostics Box

Two types of diagnostics boxes, a 6 way box and a 8 way box, were used in the collimation channel to house beam diagnostics.

The 6 way box installed at the entrance of the channel was used to house a 4-Jaw slits system, a beam viewer plate and camera, an ion gauge, and a faraday cup, as shown in Figure 3.13 left. The 8 way box installed at the exit of the channel was used to house the same diagnostics as in the 6 way box, and in addition, two Allison emittance scanners, as shown in Figure 3.13 right.

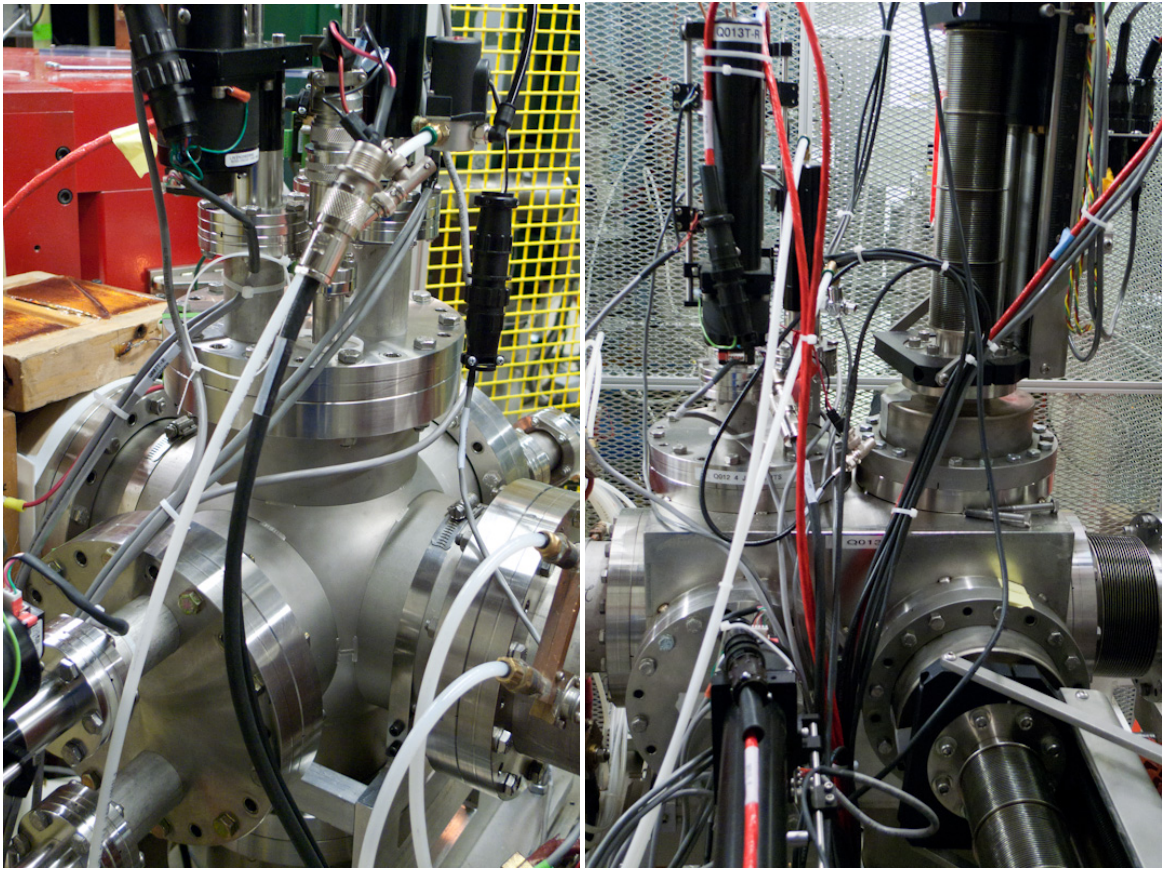


Figure 3.13: Picture of the 6 way (left) and 8 way (right) diagnostic box with instruments installed.

Chapter 4

EMITTANCE COLLIMATION CHANNEL INSTALLATION AND COMMISSIONING

4.1 Hardware Installation

4.1.1 Project Phase

The commissioning of the collimation channel consisted of two phases:

- Phase I: Commissioning in SuSI test area;
- Phase II: Re-commissioning in CCF ECR area.

Phase I: Commissioning In SuSI Test Area

In the first commissioning phase, the collimation channel was installed in the SuSI test area where the ion source SuSI was located for commissioning. Figure 4.1 is an engineering model of the collimation channel installed in the SuSI test area, where the proposed 8 way diagnostic box was replaced by two 6 way diagnostic boxes.

Phase I lasted from late May to middle July, 2009. During that period, effort was put into demonstrating the functionality of the collimation channel and in gaining experience in operating the channel associated with SuSI.

Phase II: Re-Commissioning In CCF ECR Area

In the second commissioning phase, which lasted from middle July to early November 2009, the collimation channel was moved to the CCF ECR area at the same time as SuSI was moved. Figure 4.2 is an engineering model of the collimation channel installed in the production area in combination with the achromatic transport beamline linking the collimation channel to the injection beamline of the CCF located one floor below.

During that period, effort was put into demonstrating the functionality of the achromatic transfer beamline which connects to the CCF injection beamline downstream of the collimation channel and seeking channel settings for various types of ions to be injected to CCF.

While installed in the production area, it was noticed that the magnetic field of the K1200 had non-negligible effects on the beam in the collimation channel. To mitigate such effects, one can adjust the steering magnets and shift the center of the two 4-Jaw slit systems.

4.1.2 Alignment of Components

When installing the beam line components, special attention was paid to their alignment.

Alignment of the Laser

When the alignment was done for the selecting magnet and the analyzing magnet which bends the beam 90 degrees down, a laser beam was employed as a reference

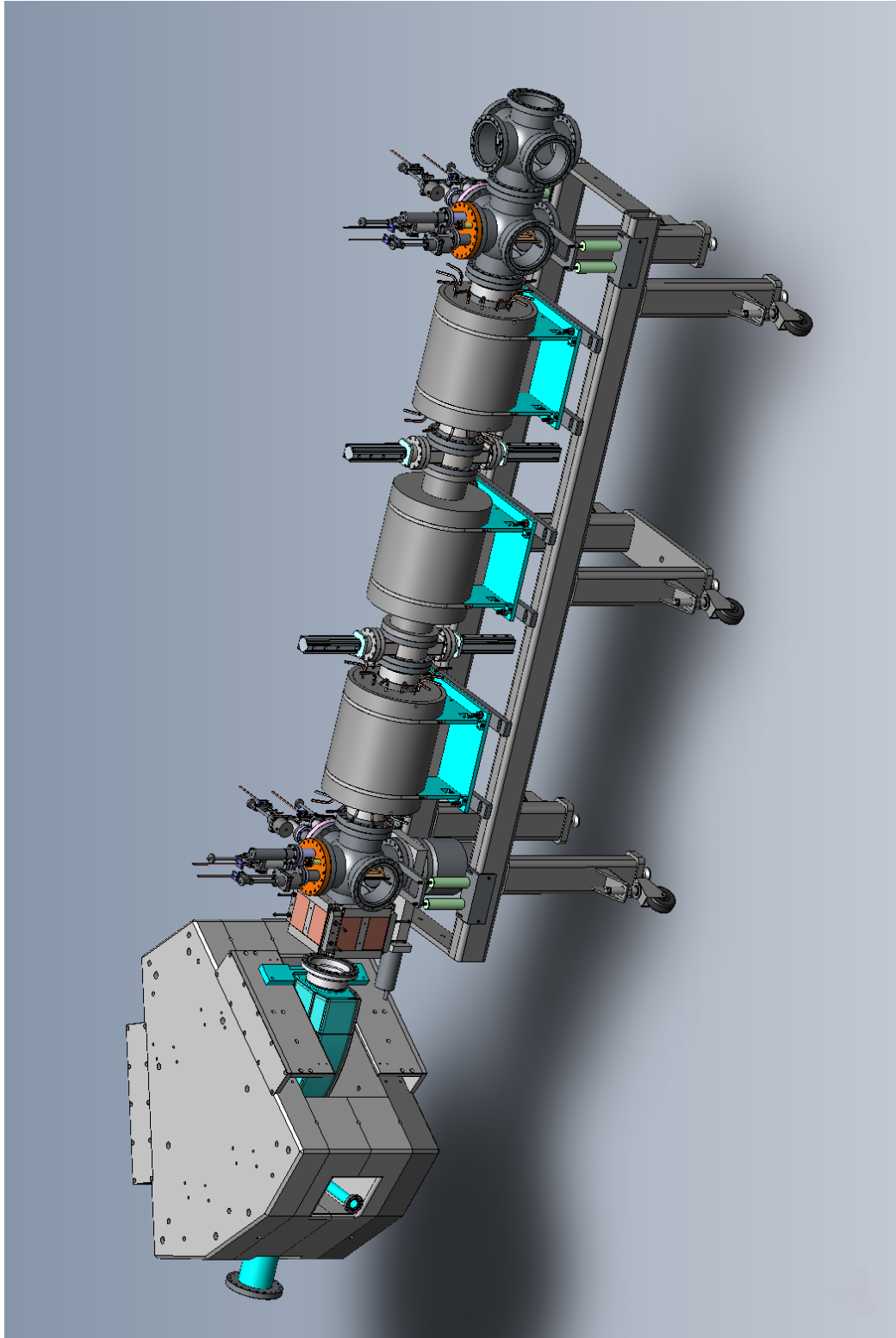


Figure 4.1: Engineering model of the collimation channel installed in SuSI test area.

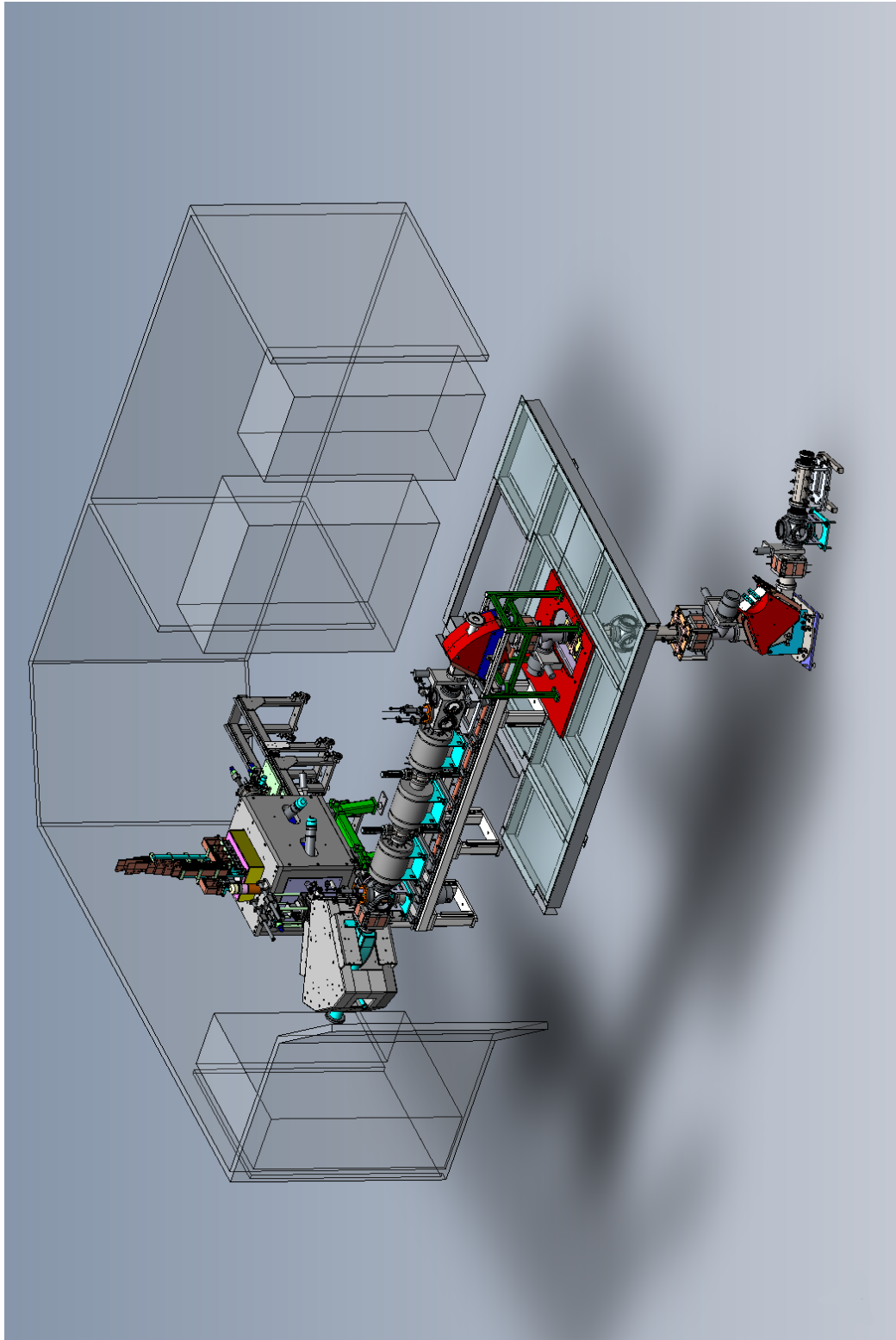


Figure 4.2: Engineering model of the collimation channel installed in the CCF ECR area with achromatic transport beamline.

for the alignment of other components.

The laser was positioned behind the analyzing magnet, and the the laser beam was aimed toward the selecting magnet (Figure 4.3). The first reference for the alignment was a target mounted on the flange of the analyzing magnet.



Figure 4.3: The laser was positioned behind the analyzing magnet, sending a laser beam back toward the selecting magnet

As the position of the beam chamber inside the selecting magnet is not precisely known, the center of its exit flange is not a good reference. A red flange cover was put on the exit flange of the selecting magnet with horizontal and vertical reference marks drawn on it. For the vertical direction, the middle seam on the side of the yoke steel, $42\frac{1}{4}$ " off the floor was used. A dot with the same height was marked on the cover to serve as the vertical reference mark. For the horizontal direction, the line

on top of the yoke steel was extended carefully with a square and the projection was marked out on the flange cover to serve as the horizontal reference mark.

The red laser dot was then aimed slightly above (about 2 mm) the center of the target on the analyzing magnet, as shown in Figure 4.4 (left), to compensate for the misalignment of the flange with respect to the beam chamber. On the other end, the red dot was adjusted to reach the plastic dot vertically and touch the line drawn, as shown in Figure 4.4 (right).

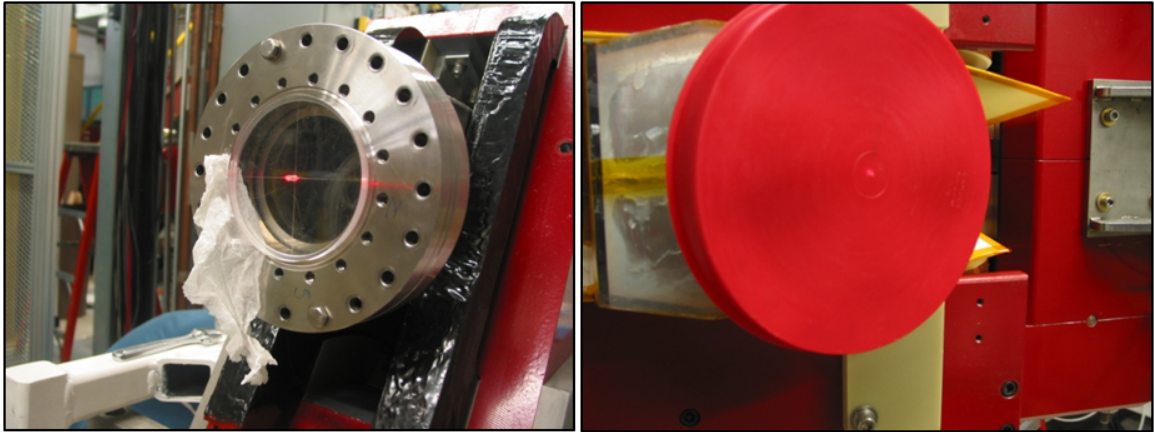


Figure 4.4: Alignment of the laser, where the red laser dot reached slightly north (about 2mm) of the center of the target on the analyzing magnet (left) . The red dot reached the plastic dot vertically and touched the line drawn on the flange cover put on the selecting magnet (right).

Then the laser beam was aligned and ready to use as a reference to align other components.

Preliminary Alignment of the Middle Solenoid

As the bore was fixed to the yoke, the alignment of the middle solenoid was done by using the two 1 mm holes of the aperture systems connected to the entrance and exit flanges of the solenoid. The yoke was first adjusted vertically and then horizontally until the laser beam passed through both 1 mm holes and the red dot appears on the red flange cover. The optimal position of the yoke was achieved when the red laser

dot was at the highest intensity on the flange cover. To check the alignment of the aperture holes with the middle solenoid flanges, the target was moved to each flange as shown in Figure 4.5, where the left picture shows the exit flange on the east side while the right one shows the entrance flange on the west side.

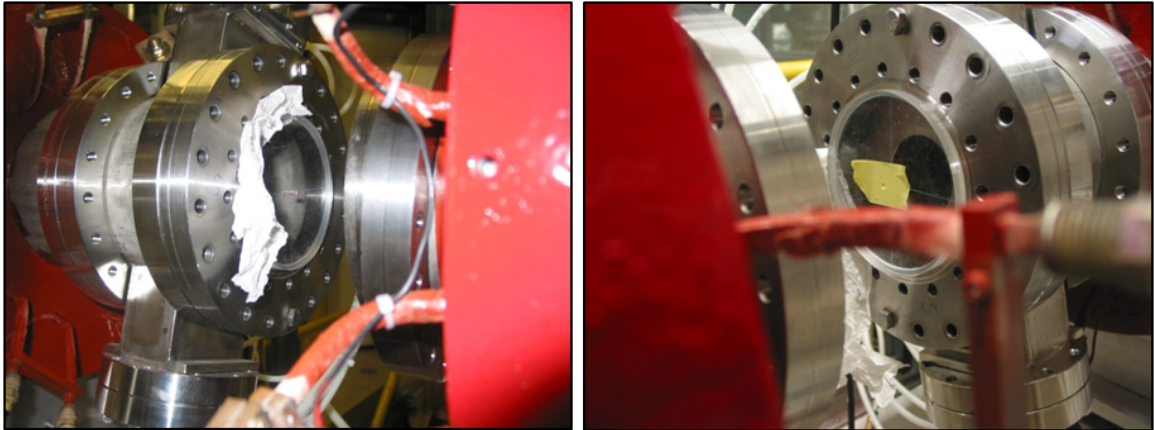


Figure 4.5: Alignment target mounted on the entrance and exit flanges of the middle solenoid with aperture systems connected. The target was mounted on the exit flange on the east side (left) and the the entrance flange on the west side (right), respectively.

Preliminary Alignment of Outer Solenoids

The other two solenoids were then attached to the central solenoid. Figure 4.6 shows the target mounted on the flanges at each end of the beam tube. The beam tube for each was disconnected from the yoke and the yoke was simply positioned to have the beam tube positioned in the middle of the gap. Final alignment of the yoke was done with a beam based alignment discussed later.

Alignment of the 6 Way Diagnostic Box

The 6 way diagnostic box was connected to the first solenoid and aligned with the help of a target as well. Figure 4.7 (left) shows the target mounted on the entrance flange of the diagnostics box. The right picture shows the target mounted on the exit

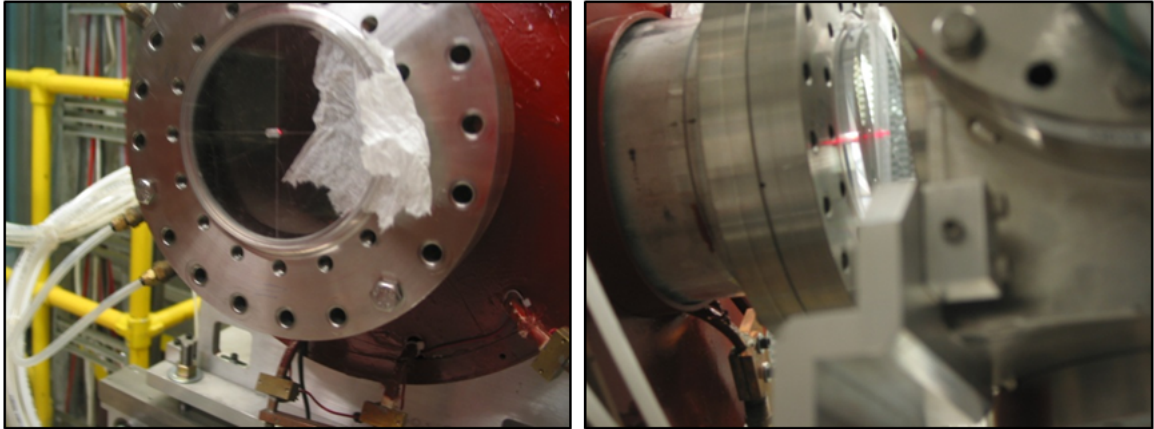


Figure 4.6: Alignment target mounted on the entrance flange of the first solenoid (left) and the exit flange of the last solenoid with little room as the diagnostic box has been installed on the channel railing (right).

flange of the diagnostics box and the laser does appear slightly lower than the target. This difference is probably due to the flange being welded too high.

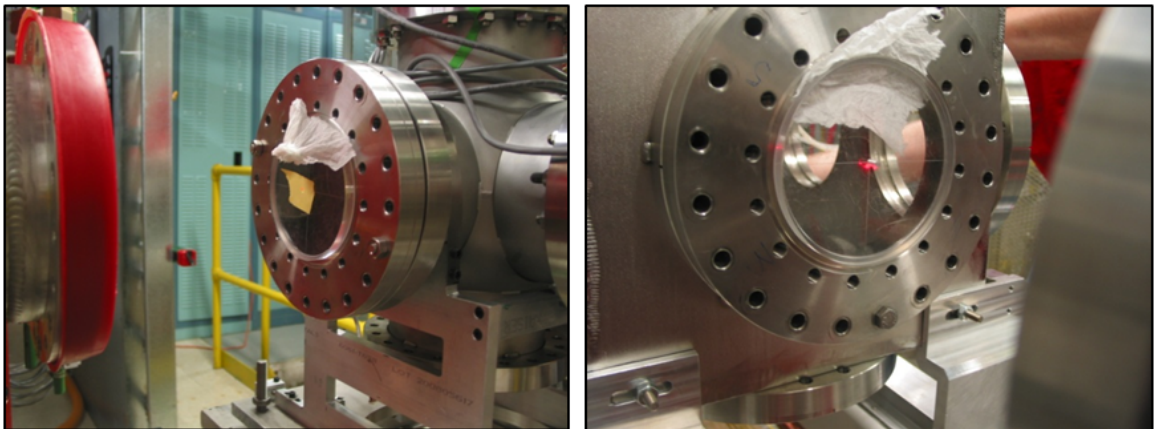


Figure 4.7: Alignment target mounted on the entrance and exit flanges of the diagnostics box connected to the first solenoid. The picture on the left shows the target mounted on the entrance flange of the diagnostics box. The right picture shows target mounted on the exit flange of the diagnostics box and the laser does appear slightly lower than the target. This difference is probably due to the flange been welded too high.

Final Beam Based Alignment of the Solenoids

To further align the first and last solenoids where the beam tube is disconnected from the yoke, a beam based alignment was performed with an $^{40}\text{Ar}^{7+}$ beam at 24 kV ECR extraction voltage using Beam Viewer Application (BVA).

As the beam tube is fixed to the yoke, a centered parallel beam was sent through the middle solenoid. When we changed the current that was fed to that solenoid while the other solenoids were turned off, the change of the beam centroid was negligible as calculated by BVA based on the image captured from the beam viewer at the end of the channel. This assured us that the magnetic axis of the central solenoid was properly aligned with the beam axis defined by its flanges. The centered parallel beam was then used to check the alignment of the other two solenoids.

The same current scan was done for the first and the last solenoids, respectively. If the beam centroid moves with the change of the solenoid current, then it indicates the magnetic axis and beam axis do not coincide. We adjusted the yoke of the solenoid according to the direction where the centroid changed to correct the misalignment. For example, we adjusted the yoke vertically when the centroid moved horizontally. Figure 4.8 shows the result when we were aligning the first solenoid. Only a small residual shift of the centroid to the left and upward was noticed when the solenoid was turned off and fed with 100 A current, illustrating a good alignment of the yoke with respect to the beam axis.

4.2 Software For Commissioning

4.2.1 Beam Viewer Application (BVA)

Beam Viewer Application (BVA) is a Matlab-based real-time beam measurement program developed to analyze the beam images provided by the beam viewers at

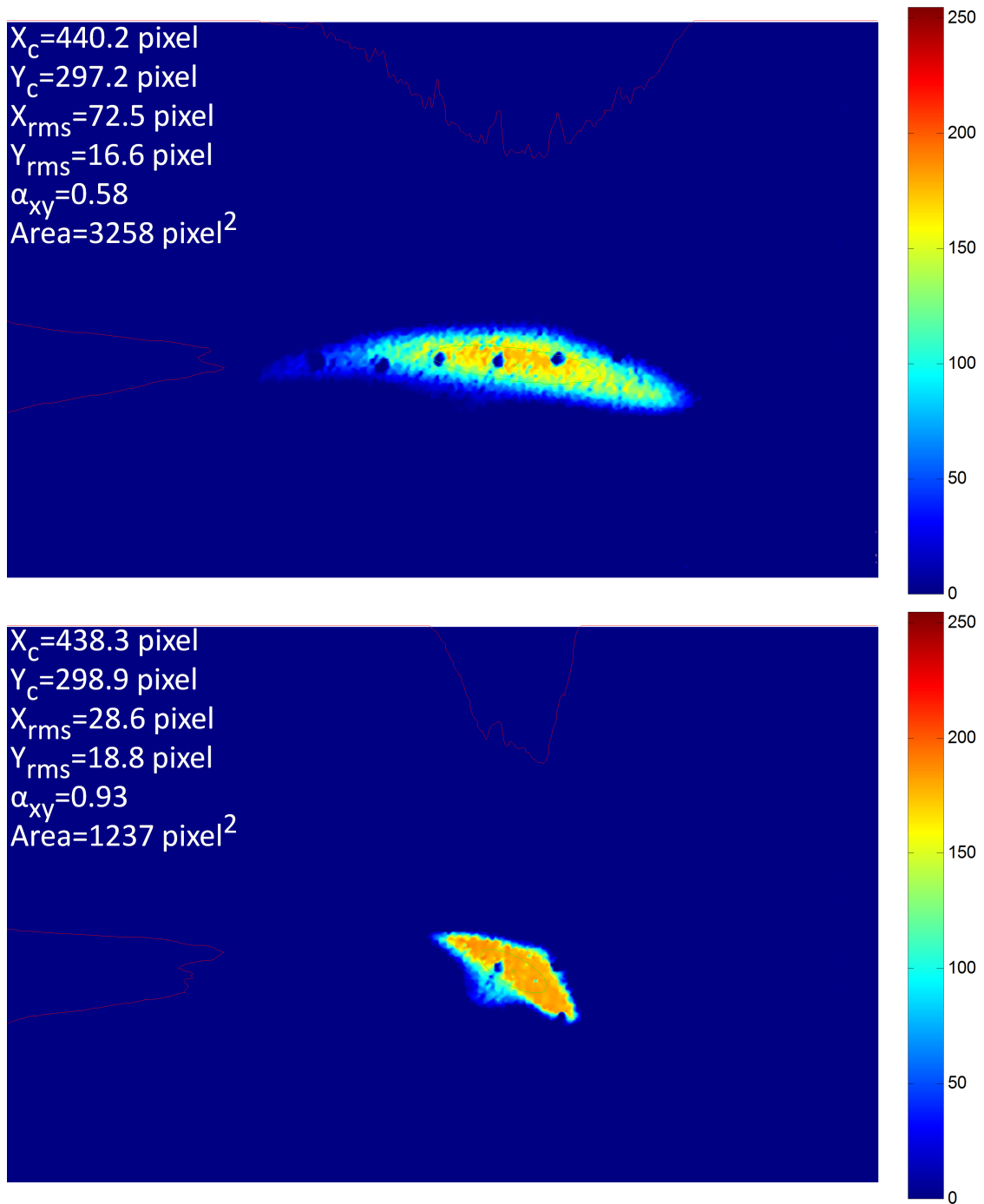


Figure 4.8: Beam based alignment of the first solenoid. Image was processed by BVA, with solenoid turned off (top) and 100 A current fed (bottom). A good alignment was achieved.

NSCL. It integrates the capabilities of displaying, processing and recording images on the beam viewer plates and captured by cameras, to improve the efficiency of measurements and meet the needs of users.

We chose Matlab to develop this program by considering the calculation speed and the commercial availability of multiple tool boxes.

The basic image acquisition scheme of BVA is shown in Figure 4.9. The Video Acquisition Tool Box of Matlab controls the video card in the controlling computer, which is used to capture beam images on the viewer plate by an analogue camera sitting outside the beamline.

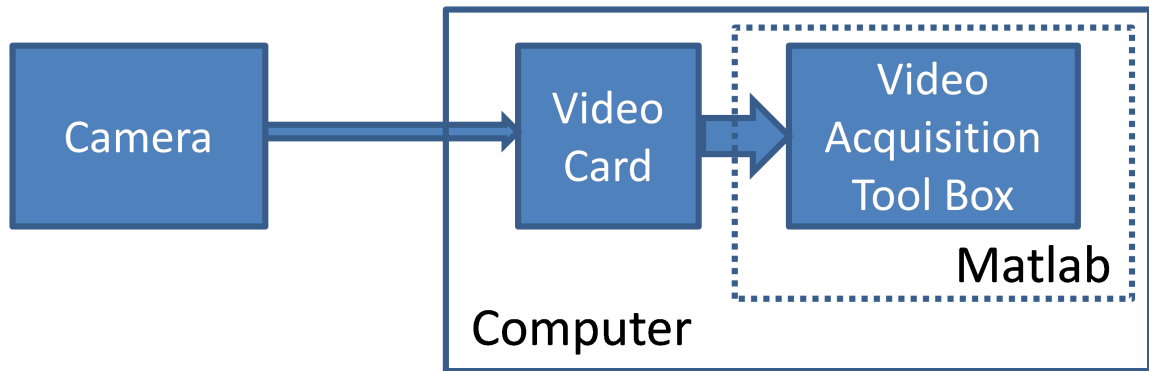


Figure 4.9: Basic image acquisition scheme of Beam Viewer Application.

After proper processing, including for example background subtraction, thresholding, calibration, BVA could extract the basic beam parameters, including TWISS parameters, RMS sizes, centroid location, etc., for both the live images and snapshot images.

The layout of the program is shown in Figure 4.10. It consists of five main modules:

- live image module, to control and display the live images from the camera;
- still image module, to display the snapshots saved from live feed or loaded from hard disk;

- file manipulation module, is to do some basic file manipulations and assign background images from the list of images;
- option module, where image processing options are located;
- information module, which consists of two panels, one to facilitate image calibration and another to display basic beam parameters extracted.

BVA was used extensively during the commissioning of the collimation channel and since then has been used by other projects at the NSCL, for example in the ReA3 Reaccelerator project. In our project, BVA facilitated various tasks from beam-based alignment to beam tuning. It proved to be efficient and convenient to users.

4.2.2 Trace 3D

Trace3D[30] is a free and easy-to-use interactive 6D linear beam-dynamics code capable of calculating envelopes of bunched beams through a transport system defined by users. Trace3D is able to provide an immediate display of beam envelopes through the channel and beam ellipses in phase space. At the same time, Trace3D accommodates several types of fitting and beam-matching options to facilitate beamline design. An example of beam simulation using Trace3D is shown in Figure 4.11.

In our project, Trace3D was used to backtrack beam envelopes in order to assist in improvement of the collimation efficiency for mismatched beams.

4.2.3 Allison Emittance Scanner

The Allison emittance scanner is controlled by a interface built in Labview software. After the measurement, the data is processed by a code package working in Matlab.

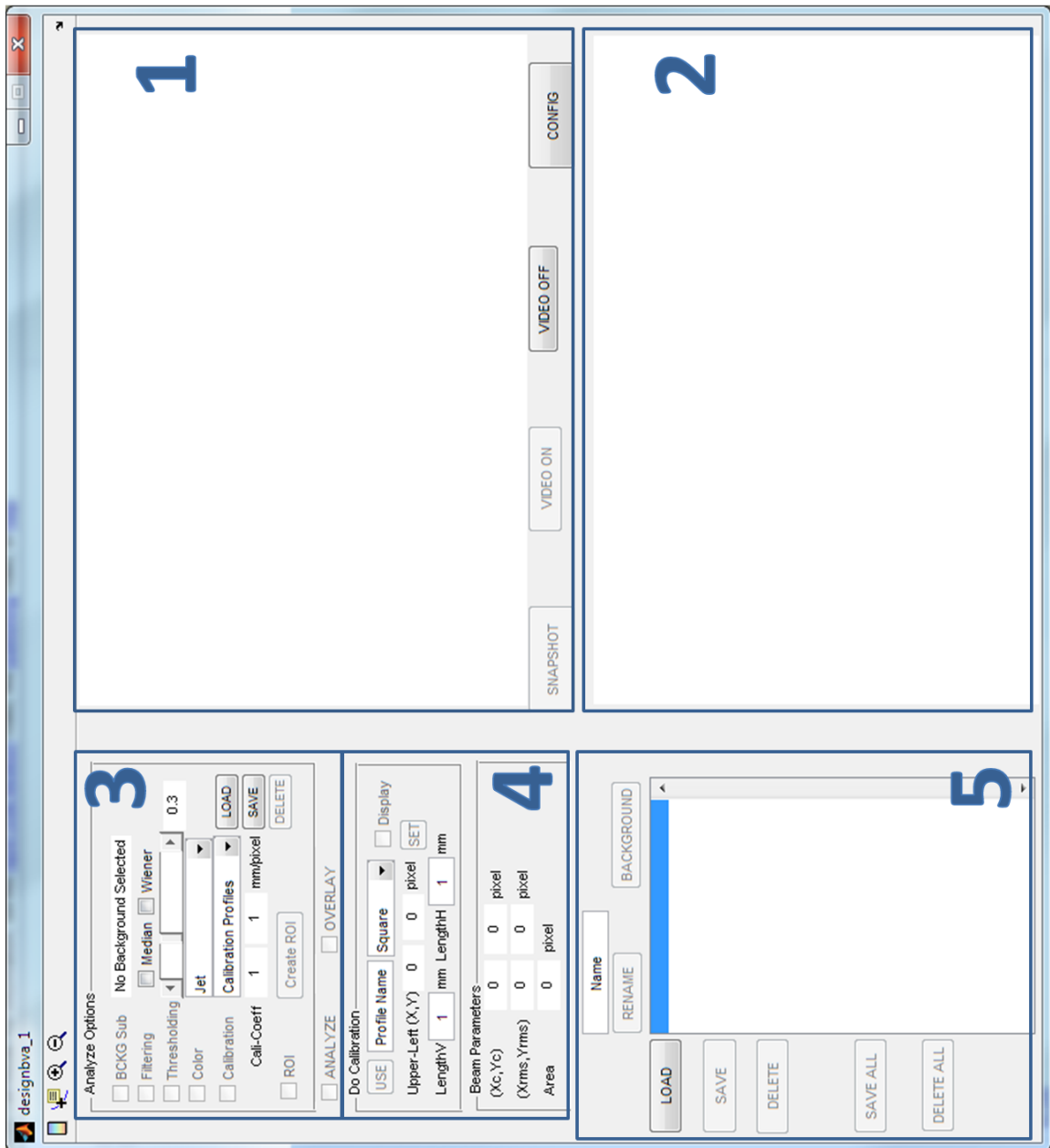


Figure 4.10: Layout of BVA. It consists of five modules, (1), live image module; (2), still image module; (3), file manipulation module; (4), option module; (5), information module.

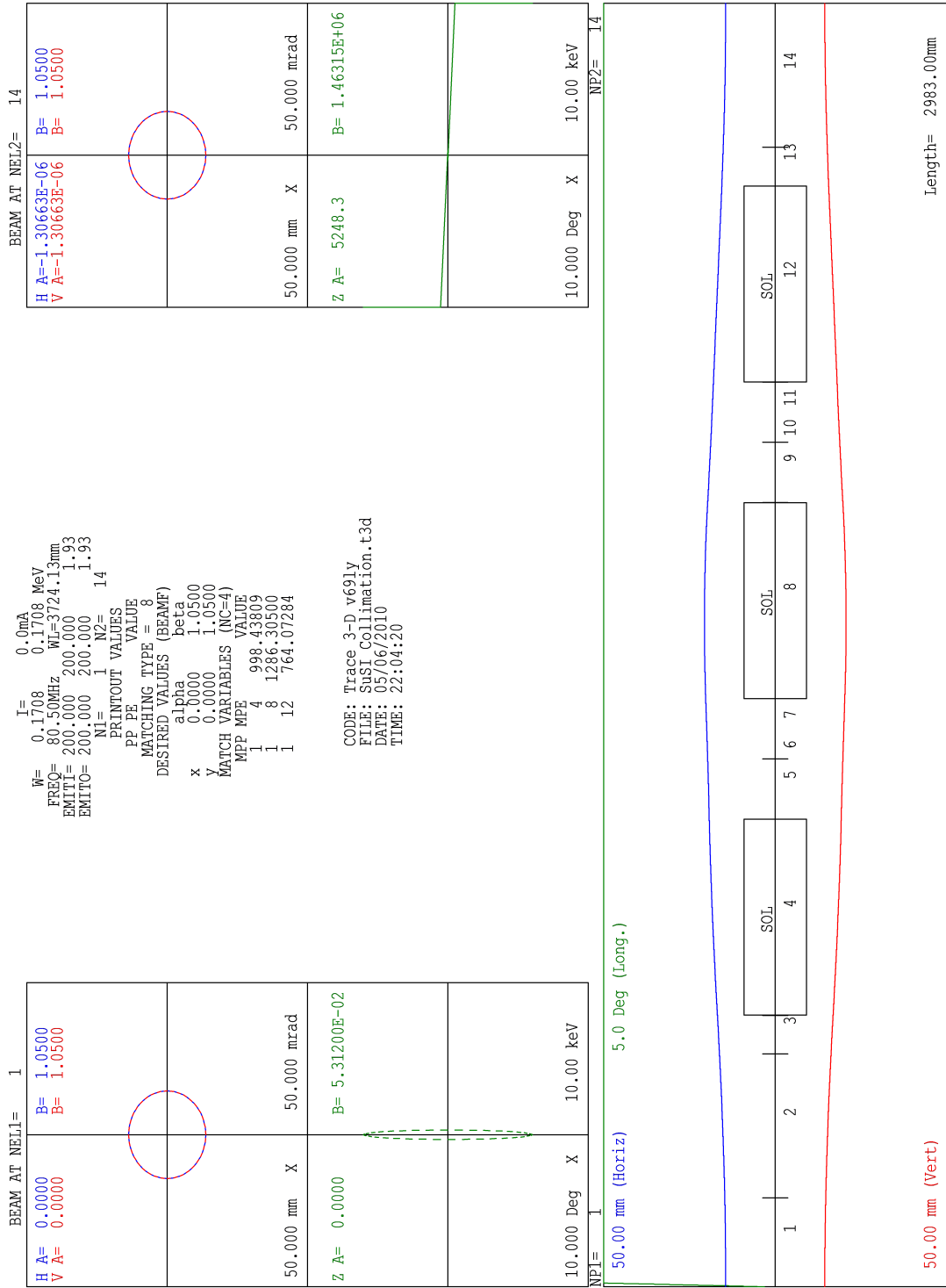


Figure 4.11: An example of beam simulation using Trace3D.

Labview Interface

The Allison emittance scanner is controlled by a interface written by the electronics group using Labview software, shown in Figure 4.12.

Various emittance scan parameters can be defined in this interface, including the unit for current read out from the faraday cup, scan span and step sizes for the position and angle. Once finished scanning, the data file is sent through the network to the interface and a copy is saved on the server.

Post Processor

Further actions, including for example noise reduction and information extraction, are needed to visualize the data and prepare images for documentation. These are done by a Matlab code package called Post Processor, written by Professor Marc Doleans at the NSCL.

Noise reduction is done by setting the threshold level in Post Processor, typically set to 5% of the measured peak current. As a consequence, some of the beam is sacrificed and the calculation of rms Twiss parameters is affected.

Information about the current, i.e. rms Twiss parameters, is extracted from the data and overlaid on the image. The brightness curve is calculated as well, which calculates the brightness for various ellipses with the same rms α and β but different emittances.

An example of the processed image is shown in Figure 4.13, where the upper-left corner displays user input text; upper-right corner, brightness curve data; lower-right corner, current measured and extrapolated; lower-left corner, RMS Twiss parameters and full beam emittance.

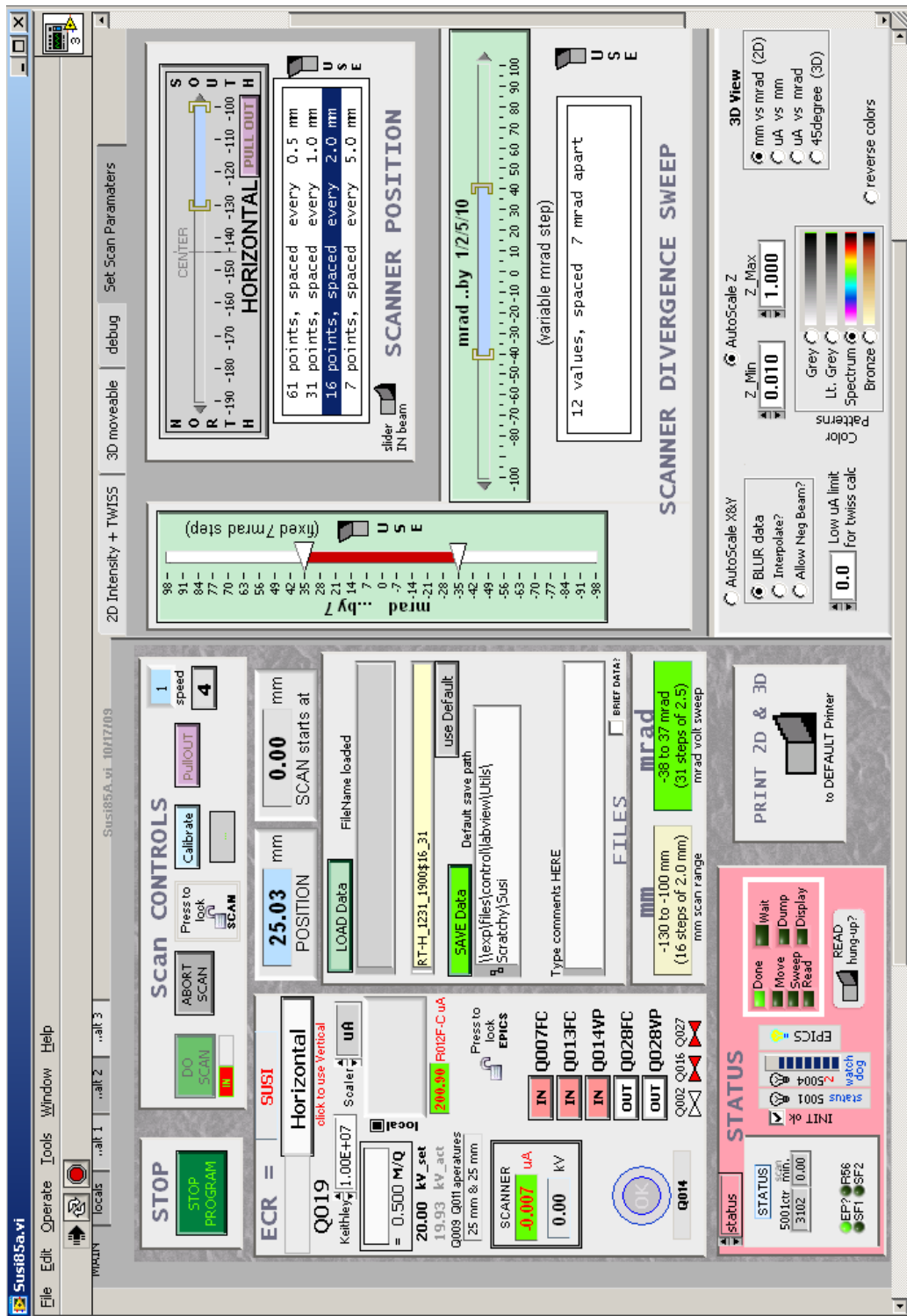


Figure 4.12: Labview interface of the Allison emittance scanner.

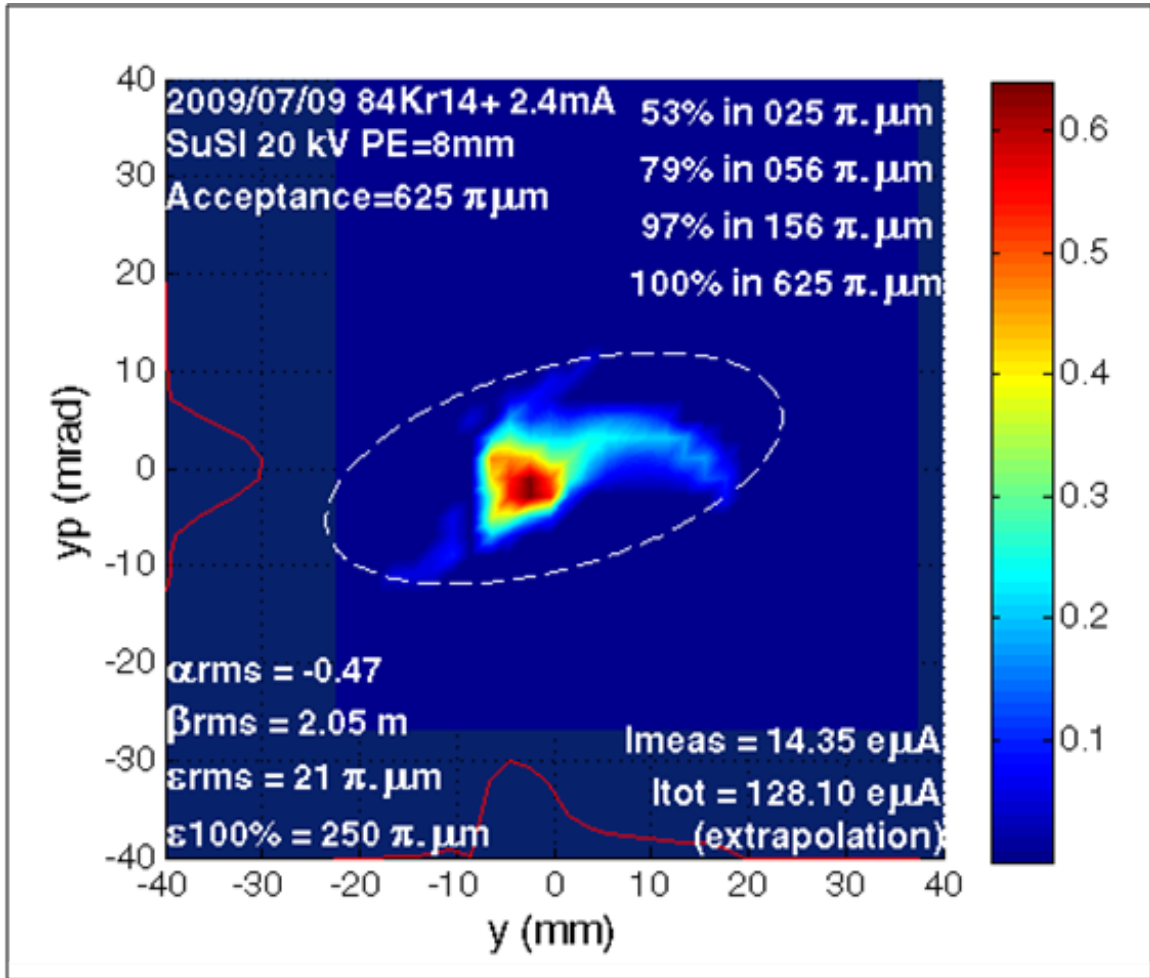


Figure 4.13: Image of emittance scan generated by Post Processor, where the upper-left corner displays user input text; upper-right corner, brightness curve data; lower-right corner, current measured and extrapolated; lower-left corner, RMS Twiss parameters and full beam emittance. The dashed ellipse corresponds to the 100% emittance.

4.3 Beam Experiment

4.3.1 Steering Magnet Calibration

To quantify the angular kick given to a certain beam, the steering magnets need to be calibrated. To do so, we decided to scan the current fed to the steering magnets and measure the relative horizontal and vertical change of the beam centroid on the viewer plate downstream. By measuring the distance from the exit of steering magnet to the

viewer plate, we could figure out the relation between the current and the angular shift of that steering magnet in the horizontal and vertical directions.

BVA was used to capture the images and to extract the change of the centroid. As BVA could only extract distance information in terms of pixels, we first calibrated BVA to find the conversion coefficients between pixels and mm in both the horizontal and vertical directions, which are listed below:

- Horizontally, $10.3\text{pixel}/\text{mm}$,
- Vertically, $8.6\text{pixel}/\text{mm}$.

Following the calibration of BVA, the steering magnet was calibrated. We closed the first 4-Jaw slits to an opening of $5\text{ mm}\times 5\text{ mm}$, and all other apertures to 50 mm to get a small beam spot. The current fed to the steering magnet after the selecting magnet was then varied and the relative change of the centroid on the beam viewer at the end of beamline measured. Since the distance from the exit of steering magnet to the viewer plate was 2.75 m , the angular shift of the beam for a certain current was then calculated in mrad. Results are shown in Figure 4.14 with horizontal direction on the top, and vertical direction the bottom.

A linear relation was established between the shift of the beam and the current (in the range of -0.2 A to 1 A) in both directions. The coefficients were then extracted through a linear fit of the data, and listed below:

- Horizontal, $11.38\text{ mrad}/\text{A}$,
- Vertical, $9.63\text{ mrad}/\text{A}$.

These result are only valid for a $^{40}\text{Ar}^{7+}$ beam with 24 kV ECR extraction voltage, i.e. magnetic rigidity $B\rho = 0.0533\text{ T}\cdot\text{m}$.

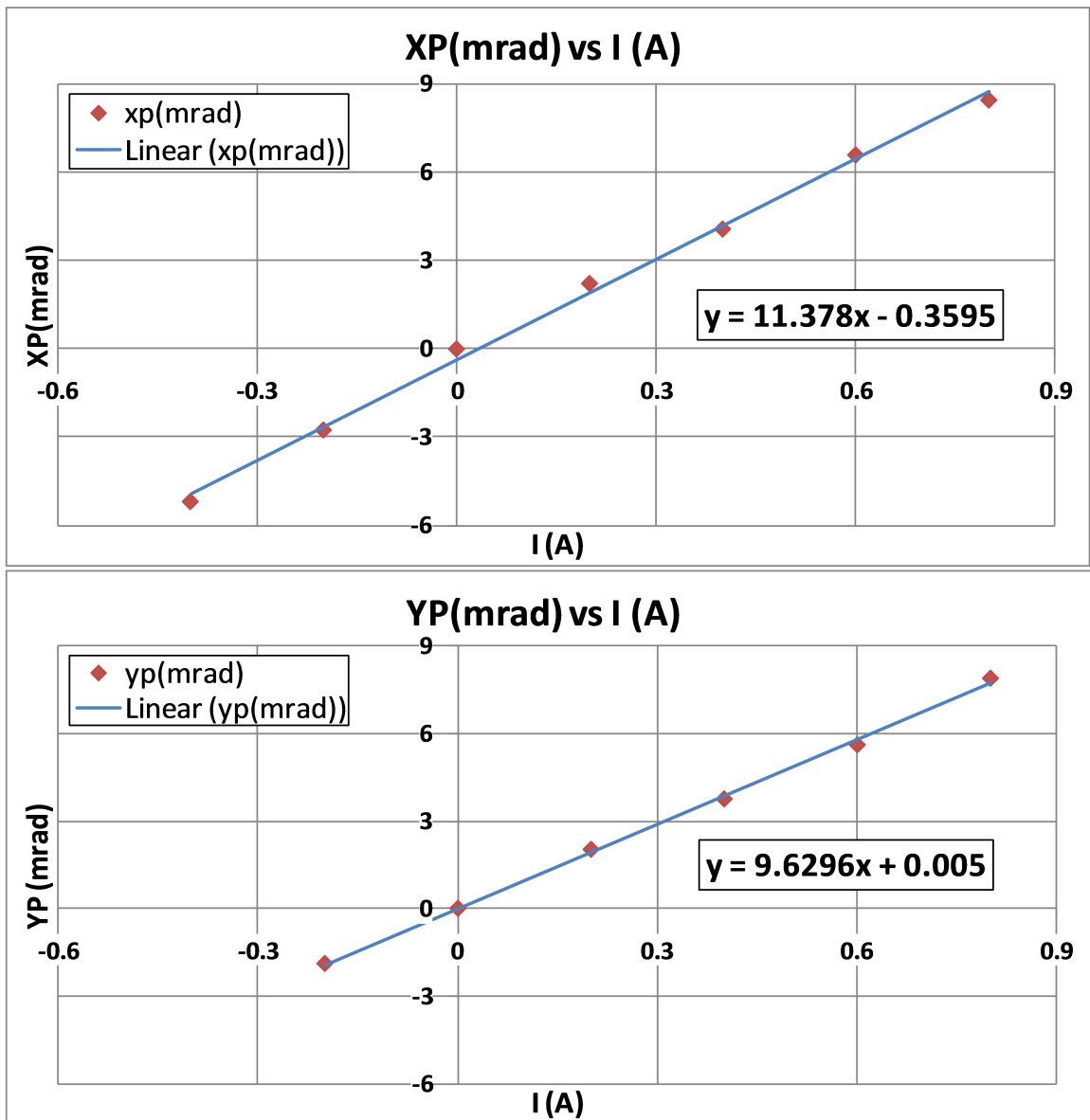


Figure 4.14: Result of steering magnet calibration. Relative changes of centroid in mm were measured and then converted to the corresponding kicks of beam in mrad, provided the distance from the exit of steering magnet to the point of measurement, when we varied the current fed to the steering magnet to give the beam kicks, horizontally (top) and vertically (bottom), respectively.

4.3.2 Solenoid Modeling

A simplified drift hard-edge solenoid drift model for the solenoids was established for efficient beam dynamics computation. The best model was devised based on the precise longitudinal field profile along the beam axis calculated using POISSON[31] according to the actual solenoid geometry.

In POISSON, a 1 m solenoid cell was set up, and the flange-to-flange length of the hardware (0.636 m) was used as the natural boundaries of the field region, which is shown in Figure 4.15.

The field was initially calculated with a total current of 10000 A (15.152 A in the conducting coil), which corresponded to a maximum longitudinal field along the beam axis of $B_{max} = 310 \times 10^{-4}$ T. Then the calculation was done for two longitudinal on-axis field levels, $B_{max} = 0.05$ T and $B_{max} = 0.2$ T, which are maximum on-axis fields for a realistic field profile, with currents in conducting coil scaled to 24.37 A and 97.48 A, respectively. The longitudinal on-axis fields for the two cases were then extracted for optimization in Matlab.

The goal of the optimization was to find certain parameters that minimize the difference between the transfer matrix of the cell from real field profile and that of an equivalent hard-edge model for beams with $B\rho = 0.487$ T·m. Such parameters include:

1. the lengths of the equivalent hard-edge solenoid and the adjacent drifts while constraining the total length to 0.635 m (corresponding to flange-to-flange length of the solenoid in the beamline),
2. the coefficient α used to convert the current in the conducting coil to the effective magnetic field of the hard-edge solenoid, $B_s(T) = \alpha \cdot I_{coil}(A)$.

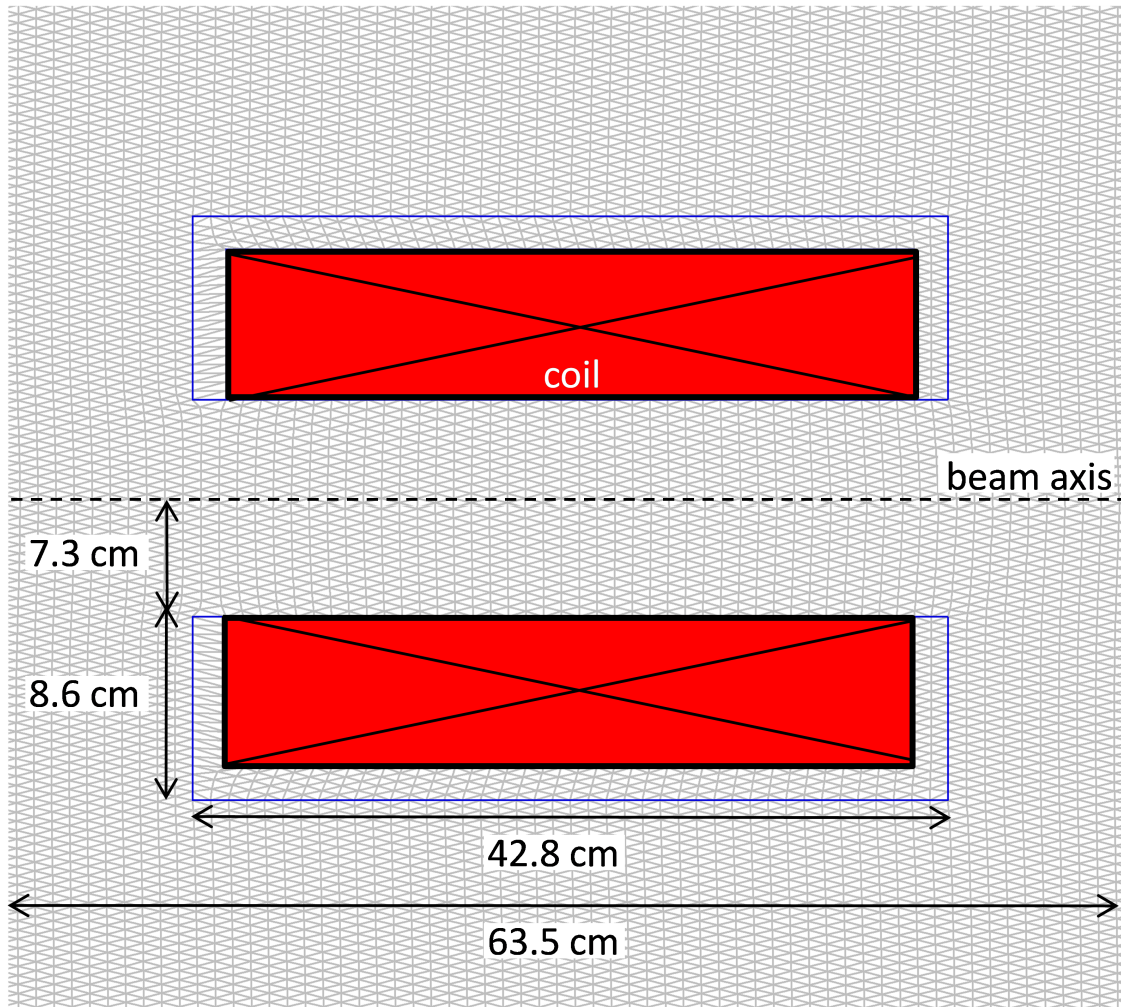


Figure 4.15: Solenoid field region set up in POISSON, truncated from a 1 m cell .

To calculate the transfer matrix of the cell from the real longitudinal field, we divided the solenoid cell into hundreds of small pieces, based on the field profile sampling. Each piece consists of two elements, the entrance where the field changes value and the body where the field stays constant. For the i^{th} piece, the transfer matrices of the entrance (R_i^{entry}) and the body (R_i^{body}) are:

$$R_i^{entry} = \begin{pmatrix} 1 & 0 & 0 & 0 \\ 0 & 1 & \Delta k_i & 0 \\ 0 & 0 & 1 & 0 \\ -\Delta k_i & 0 & 0 & 1 \end{pmatrix},$$

$$R_i^{body} = \begin{pmatrix} 1 & \frac{S_i}{2k_i} & 0 & \frac{1-C_i}{2k_i} \\ 0 & C_i & 0 & S_i \\ 0 & -\frac{1-C_i}{2k_i} & 1 & \frac{S_i}{2k_i} \\ 0 & -S_i & 0 & C_i \end{pmatrix},$$

where

$$\Delta k_i = \frac{B_{i+1} - B_i}{2B\rho},$$

$$k_i = \frac{B_i}{2B\rho},$$

$$C_i = \cos(k_i L),$$

$$S_i = \sin(k_i L),$$

B_i and L are the field strength and the length of the body element. The transfer

matrices for the i^{th} piece R_i^{piece} and the solenoid cell R_{tot} are:

$$R_i^{piece} = R_i^{body} \cdot R_i^{entry} ,$$

$$R_{cell} = \prod_i R_i^{piece} .$$

For the equivalent model, the transfer matrix was calculated as

$$R_{total} = R_{drift} \cdot R_{solenoid} \cdot R_{drift},$$

where R_{drift} is the transfer matrix of drift with length $L(m)$,

$$R_{drift} = \begin{pmatrix} 1 & L & 0 & 0 \\ 0 & 1 & 0 & 0 \\ 0 & 0 & 1 & L \\ 0 & 0 & 0 & 1 \end{pmatrix} ,$$

and $R_{solenoid}$ is the transfer matrix of the hard-edge solenoid with length $L(m)$ and magnetic field $B(T)$,

$$R_{solenoid} = \begin{pmatrix} C^2 & \frac{1}{k}SC & SC & \frac{1}{k}S^2 \\ -kSC & C^2 & -kS^2 & SC \\ -SC & -\frac{1}{k}S^2 & C^2 & \frac{1}{k}SC \\ kS^2 & -SC & -kSC & C^2 \end{pmatrix} ,$$

where

$$k = \frac{B}{2B\rho} ,$$

$$B = \alpha \cdot I_{coil} ,$$

$$C = \cos(kL) ,$$

$$S = \sin(kL) .$$

In Matlab, for each field level case, the transfer matrix from the real field was first calculated. Then by varying both the effective length of the solenoid (Ls) and the effective magnetic field (BB) for the equivalent model, the deviation (δ) of the transfer matrix from that of the real field was recorded for each Ls and BB pair to find the best setting. The deviation was defined as:

$$\delta = \sum_{ij} \left(M_{ij}^{varying} - M_{ij}^{real} \right)^2 ,$$

where $M_{ij}^{varying}$ is the element of the varying matrix, and M_{ij}^{real} is the matrix element calculated from the real field. The best results achieved are shown in Table 4.1.

Bmax(T)	BB(T)	Ls(m)	Ldr(m)	Lcell(m)
0.05	0.0429	0.4625	0.0863	0.6350
0.20	0.1743	0.4560	0.0895	0.6350

Table 4.1: Best result for the two field level cases. Bmax is the maximum on-axis magnetic field, BB and Ls are the effective field strength and effective length of the solenoid in the equivalent drift hard-edge solenoid drift model, Ldr is the effective length of the drift in the model, and Lcell is the total length of the model.

For simplicity, we assumed that the effective magnetic field was linearly related

to the current fed to the solenoid, so we had the generic form:

$$\begin{aligned}
 B_s(T) &= \alpha \cdot I_{coil}(A) \\
 &= \left(\frac{B_{max}}{I_{coil}} \right)_{POISSON} \times \frac{BB}{B_{max}} \times I_{coil}(A) ,
 \end{aligned}$$

and found that:

- $B_s(T) = 0.001760 \times I(A)$, for $B_{max} = 0.05$ T field level case,
- $B_s(T) = 0.001788 \times I(A)$, for $B_{max} = 0.2$ T field level case.

The key parameters for the two field levels are summarized in Table 4.2:

Bmax(T)	$\alpha(T/A)$	Ls(m)	Ldr(m)	Lcell(m)
0.05	0.001760	0.4625	0.0863	0.6350
0.20	0.001788	0.4560	0.0895	0.6350

Table 4.2: Summary of the two equivalent solenoid models.

Then, a particle was transported through one solenoid cell fed with different currents in the simulation and the deviation in response curves of our equivalent model and the real field was calculated for the two field strengths.

In simulation, we used a $^{40}\text{Ar}^{7+}$ particle from 20 kV ECR source ($B\rho = 0.0487$ T·m) with phase space coordinates $(x, x', y, y') = (0, 15\text{mrad}, 0, 0)$. The simulated setup is shown in Figure 4.16.

The deviations in the response curves of our equivalent model and the real field are 10% for the $B_{max} = 0.052$ T case, and 6% for the $B_{max} = 0.2$ T case.

In conclusion, the model using $B_{max} = 0.2$ T was the most accurate one, as summarized below:

- Total cell length, $L_{cell} = 0.635$ m;

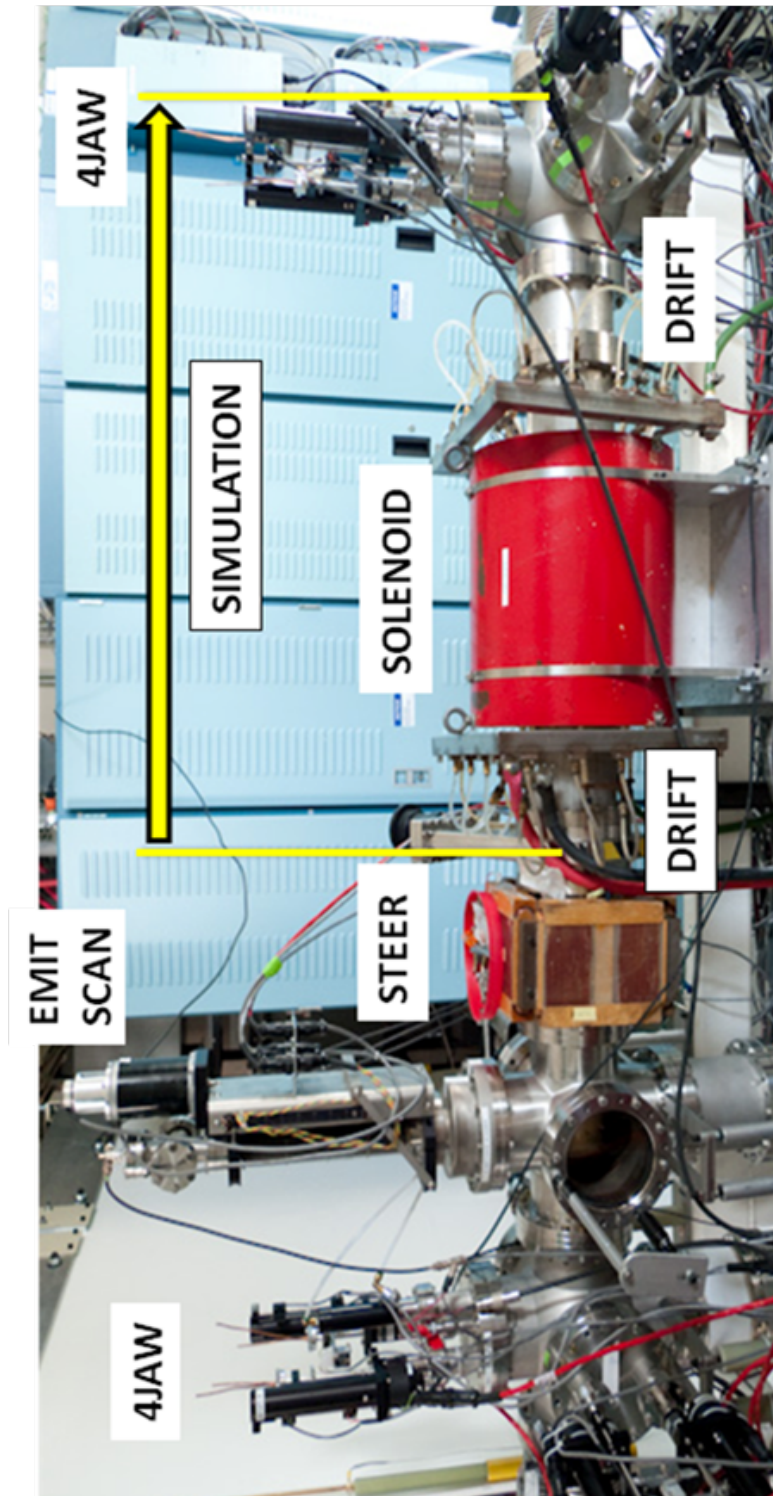


Figure 4.16: Solenoid equivalent model simulation beamline set up.

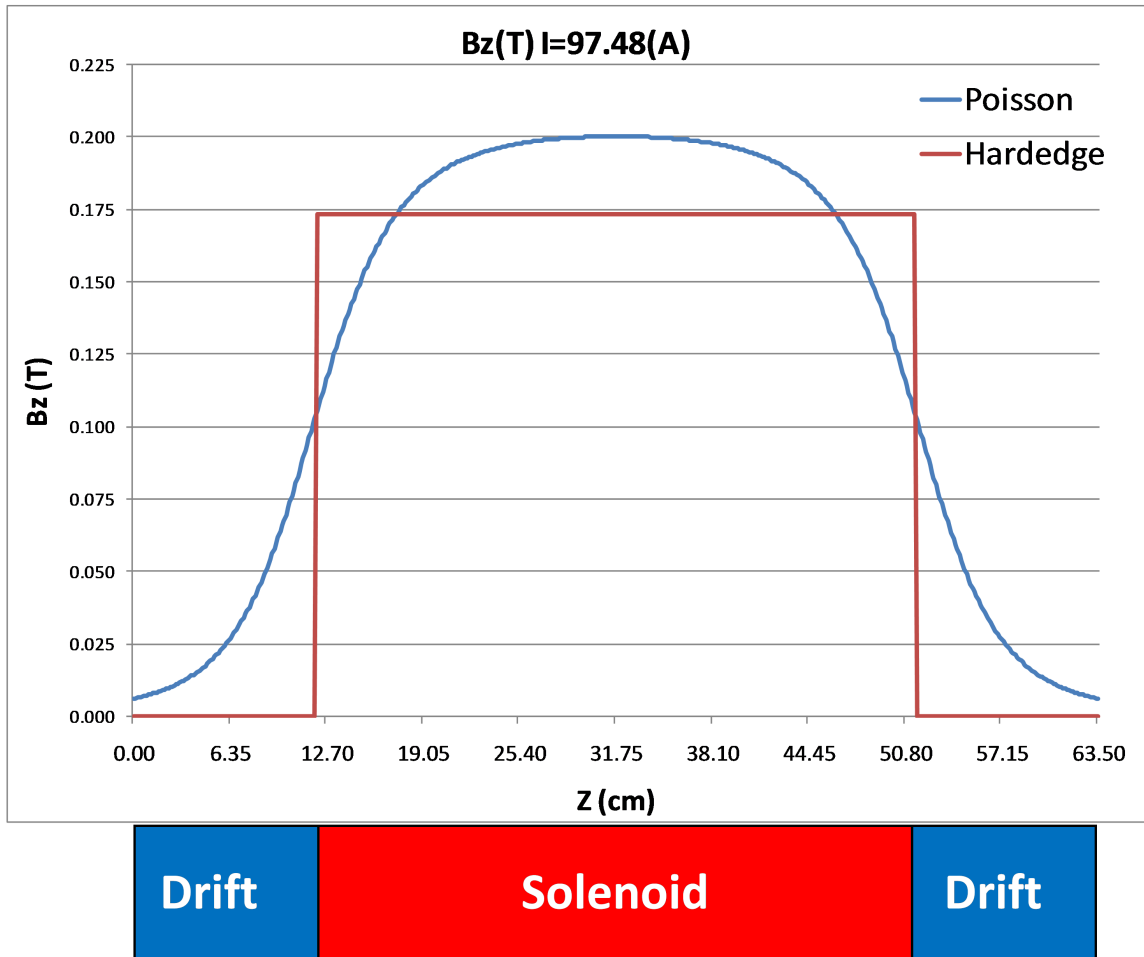


Figure 4.17: The field profiles from the POISSON calculation for $B_{max} = 0.2$ T and the equivalent hard-edge solenoid model.

- Effective solenoid length, $L_{sol} = 0.456$ m;
- Effective drift length, $L_{drift} = 0.090$ m;
- Power supply B-field conversion coefficient, $\alpha = 0.001788$ T/m.

The field profiles from the POISSON calculation for $B_{max} = 0.2$ T and the equivalent hard-edge solenoid model is shown in Figure 4.17.

4.3.3 Experimental Test of Solenoid Model

We did two experiments to check the validity of our solenoid model. Both experiments used a $^{40}\text{Ar}^{7+}$ beam with 24 kV ECR extraction voltage, corresponding to a magnetic rigidity $B\rho = 0.0533 \text{ T}\cdot\text{m}$.

First, we did a simple check of the 90 degree xy rotation of the channel to check the correct functioning of the solenoids. To do so, we set the current of all three solenoids to 60 A, and closed the first pair of 4-Jaw slits to an opening of $5 \text{ mm}\times 15 \text{ mm}$, while all other apertures were set to 50 mm, i.e. fully opened. This gave us a vertical beam profile. When transported through the channel, the placed beam rotated 90 degrees in xy space to become horizontal on the viewer downstream, as shown in Figure 4.18. With all other settings unchanged, we then closed the first pair of 4-Jaw slits to $15 \text{ mm}\times 5 \text{ mm}$, providing a horizontal beam profile. On the viewer downstream, the beam rotated to the vertical direction, reflecting a 90 degree rotation (Figure 4.19).

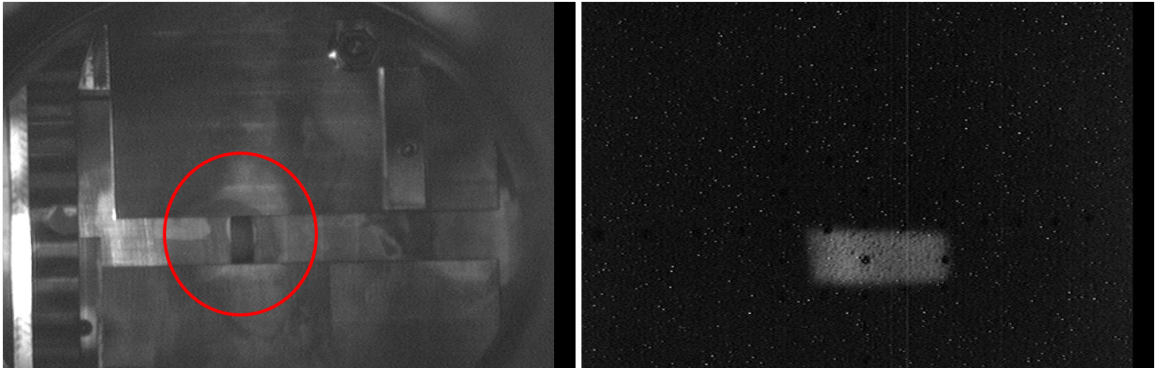


Figure 4.18: Checking solenoid xy rotation with a vertical slice of beam. On the left is a picture of the first pair of 4-Jaw slits, when opened to $5 \text{ mm}\times 15 \text{ mm}$ to achieve a vertically sliced beam; on the right is a picture of the beam viewer downstream, where the beam has rotated to a horizontal slice, reflecting a 90 degree xy rotation.

Next, we compared the response curves of the solenoid with simulations. To do so, we transported the beam with a horizontal angular shift and recorded the relative

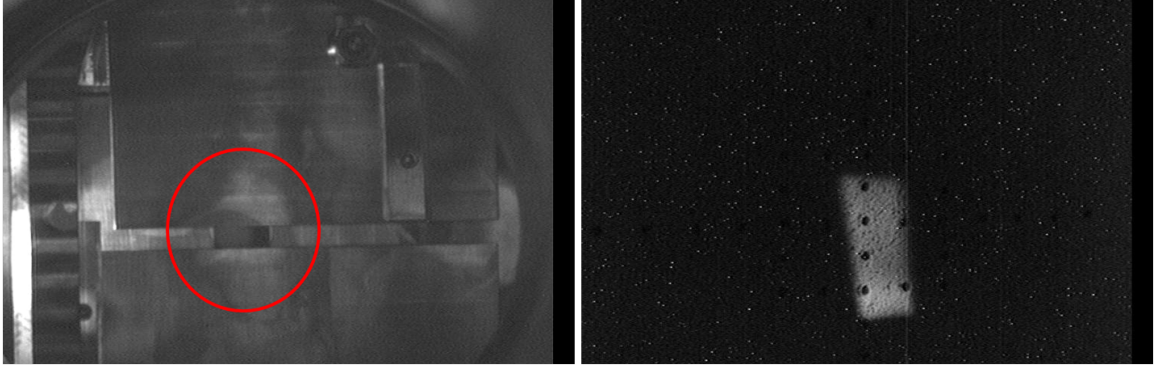


Figure 4.19: Checking solenoid xy rotation with a horizontal slice of beam. On the left is a picture of the first pair of 4=Jaw slits, when opened to 15mm \times 5 mm to achieve a horizontally sliced beam; On the right is picture of the beam viewer downstream, where the beam has rotated to a vertical slice, reflecting a 90 degree xy rotation.

changes of the centroid of beam on the viewer plate downstream, while changing the current of the middle solenoid from 70 to 135 A in steps of 5 A. The first and third solenoids were switched off. The horizontal angular shift was generated by feeding the steering magnet a current of 1.5 A, which corresponded to a 17.07 mrad angular shift. The measurement was repeated using a beam with a similar shift in the vertical direction. The comparisons are shown in Figure 4.20, where the upper plot is for the horizontal case, and the bottom one if for the vertical case. We can see a good match between the experiment and the simulation when the current is near 70 A, which is the range for the nominal operating current.

4.3.4 Beam Collimation Process

Typical Tuning Procedure

To tune the collimation channel, several steps were required:

1. do an initial tune-up of the ion source SuSI with respect to the current measured on the faraday cup at the entrance of the channel,
2. measure the beam transmission at the end of the channel,

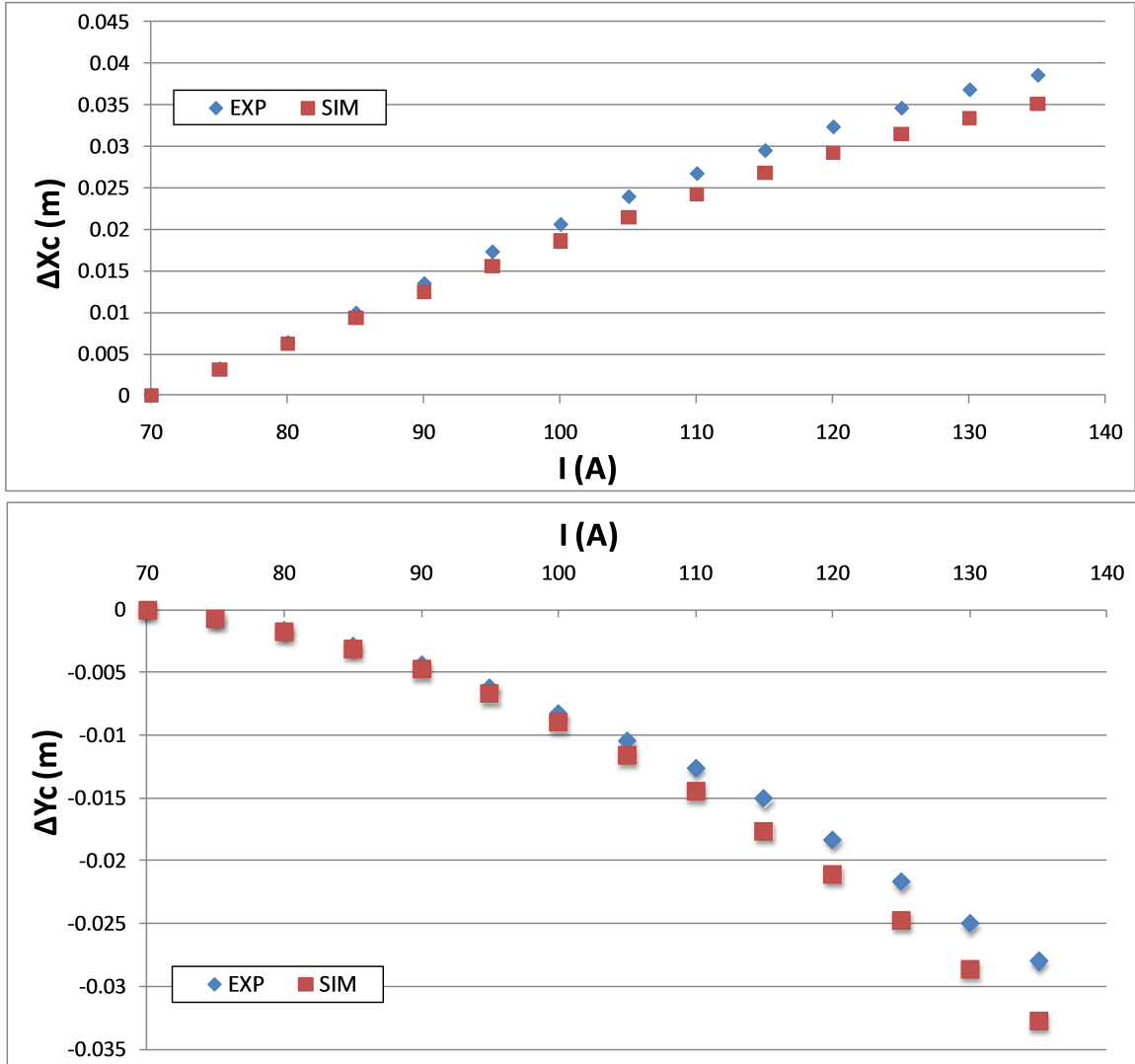


Figure 4.20: The response curves of the solenoid compared with simulations. The upper one corresponds to the horizontal kicked beam, and the bottom one the vertical kicked beam. We could see a good match of the experiment with the simulation in the lower current bound, where the nominal current of our operation lies.

3. set the current of the three solenoids according to the channel recipe mentioned in Section 2.3.2,
4. open all apertures to 50 mm and optimize the current on the faraday cup at the end of the channel by using the selecting magnet and the steering magnets before and after the selecting magnet;
5. use the ECR tune program to measure the transmission on the faraday cup at the end of the channel by scaling all three solenoids simultaneously,
6. measure the transmission again and compare the recent one to the one measured in the second step; similar results should be expected,
7. close all apertures to an opening of 15 mm, which corresponds to a $56 \pi \text{mm}\cdot\text{mrad}$ channel acceptance and believed to be roughly the CCF acceptance,
8. optimize the current measured at the end of the channel by adjusting the steering magnets and the selecting magnet,
9. do a final optimization by adjusting the center of the two 4-Jaw slits by a few mm in the horizontal direction to mitigate the steering effect from the K1200 steering magnetic field,
10. do a Charge State Distribution (CSD) measurement at the end of the channel and measure the transmission,
11. take pictures on the viewer plates at the entrance and exit of the channel using Beam Viewer Application program,
12. measure the emittance at the end of the channel using the Labview interface; if the quality is good, the beam is then ready to deliver to the CCF injection beamline.

Argon Beam Result

The collimation process was checked for a $^{40}\text{Ar}^{7+}$ beam, which was extracted from the SuSI with a 24.43 kV extraction voltage. Emittances in xx' and yy' phase spaces and currents were measured at each channel acceptance. The current was optimized when the aperture opening was adjusted, while the source parameters were kept untouched. The results are shown in Figure 4.21~4.24. It was obvious that when the channel acceptance was decreased, the measured beam emittances in xx' and yy' spaces decreased, and were all within the channel acceptances.

The brightness of the beam was also calculated when the channel was set at different acceptances. A plot showing the beam brightness (blue), beam full emittance (green) and beam current (red) with different channel acceptances are shown in Figure 4.25. From the plot, it can be noticed that when the channel acceptance decreases, the beam current and emittance both decreased, while the beam brightness increased. This clearly demonstrates the effective collimation capability of the channel.

Krypton Beam Result

The collimation process was checked for a $^{84}\text{Kr}^{14+}$ beam, which was extracted from the SuSI with a 20.00 kV extraction voltage. Emittances in xx' and yy' phase spaces were measured at each channel acceptance, as well as the beam current at the end of the channel. The current was optimized when the aperture opening was changed, while the source parameters were kept untouched. The results are shown in Figure 4.26~4.29. It was obvious that when the channel acceptance was decreased, the measured beam emittances in both xx' and yy' spaces both decrease, and are all within the channel acceptances.

The brightness of beam was also calculated when the channel were set at different acceptances. A plot showing the beam brightness (blue), beam full emittance (green) and beam current (red) with different channel acceptances are shown in Figure 4.30.

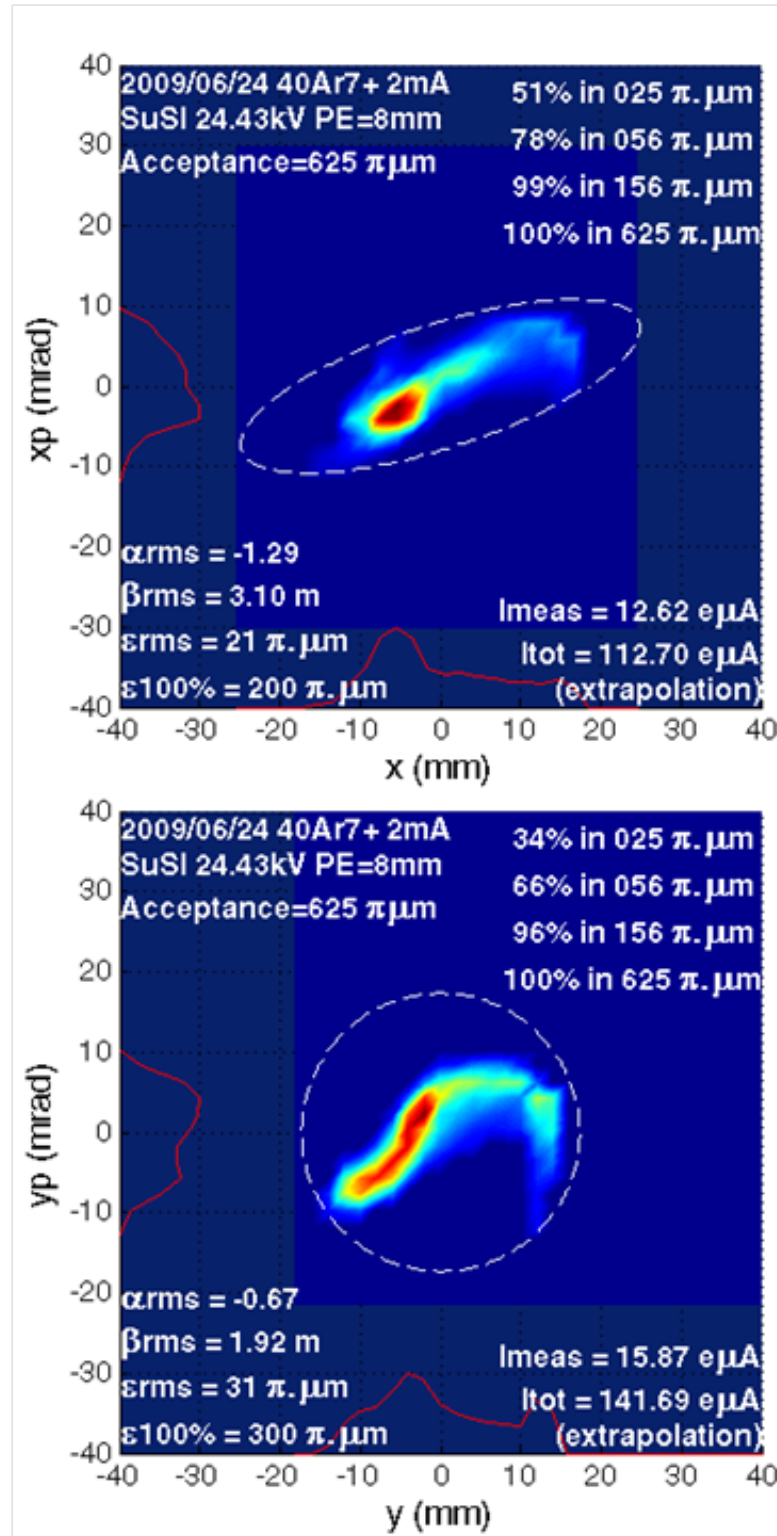


Figure 4.21: Emittances of the $^{40}\text{Ar}^{7+}$ beam measured with $625 \pi\text{-mm}\cdot\text{mrad}$ channel acceptance. Emittances in both xx' phase space (top) and yy' phase space (bottom) are shown. Currents recorded by FC is $96 \text{ e}\mu\text{A}$. All ellipses enclosed 100% of the beam.

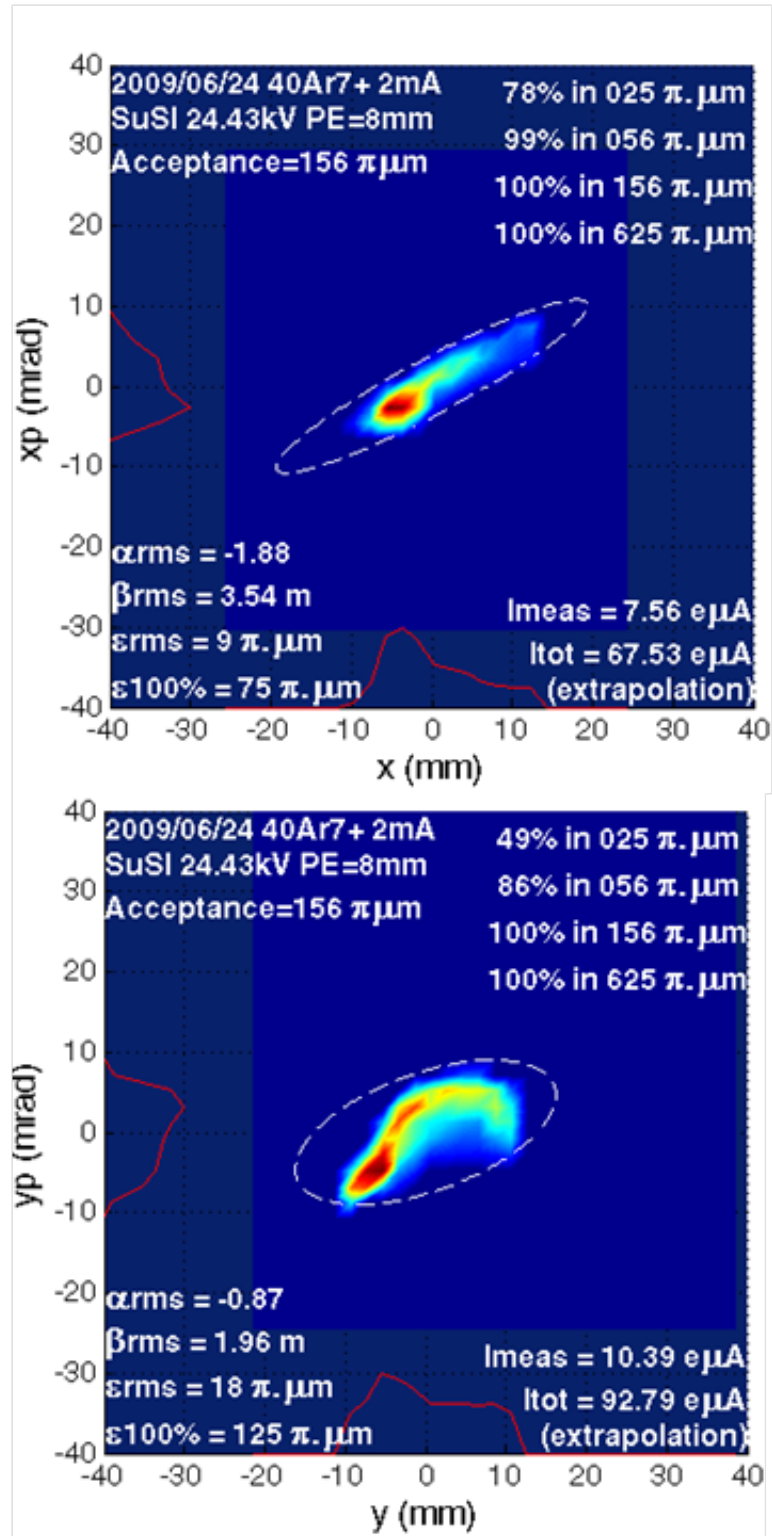


Figure 4.22: Emittances of the $^{40}\text{Ar}^{7+}$ beam measured with $156 \pi\text{-mm}\cdot\text{mrad}$ channel acceptance. Emittances in both xx' phase space (top) and yy' phase space (bottom) are shown. Currents recorded by FC is $96 \text{ e}\mu\text{A}$. All ellipses enclosed 100% of the beam.

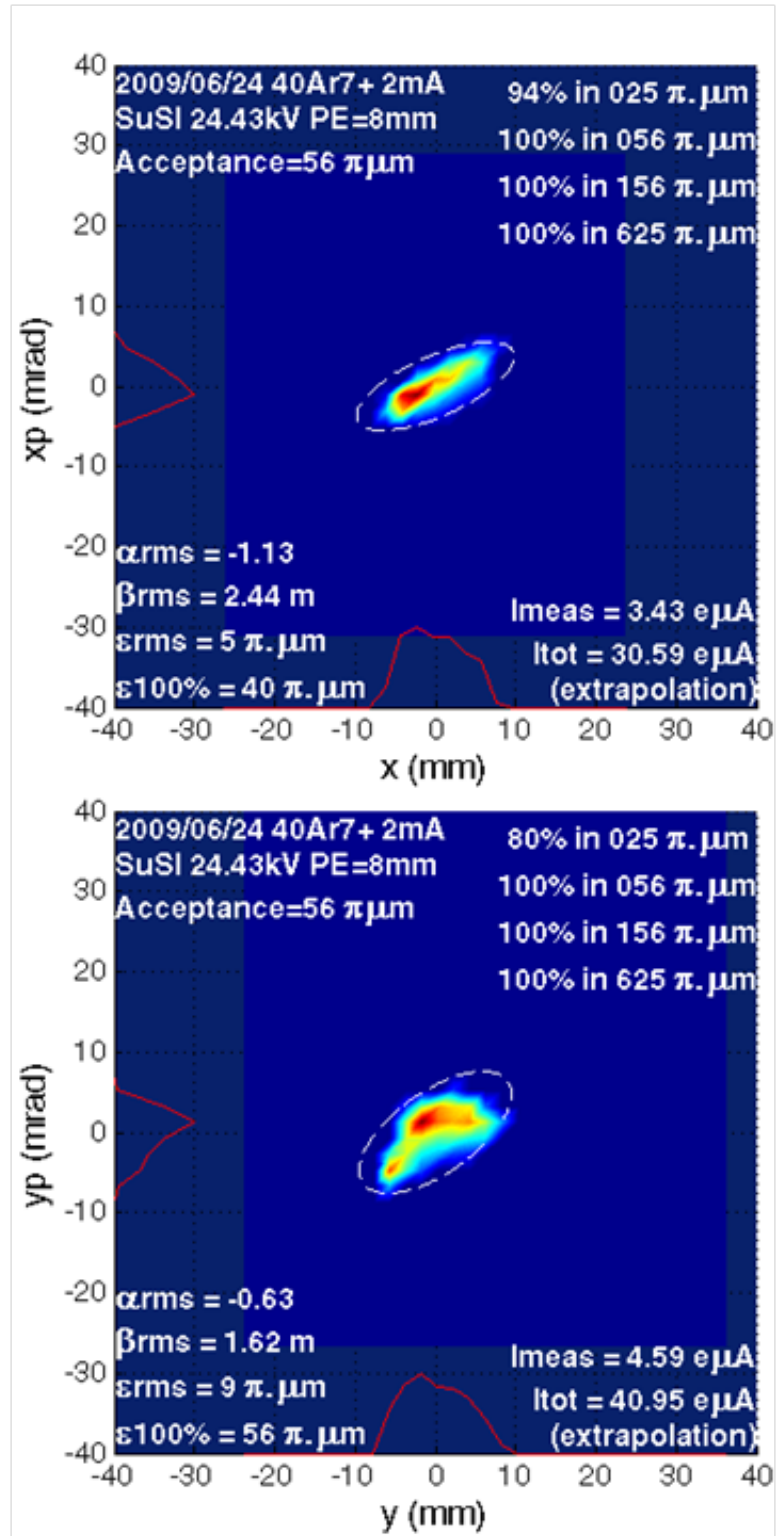


Figure 4.23: Emittances of the $^{40}\text{Ar}^{7+}$ beam measured with $56 \pi\cdot\text{mm}\cdot\text{mrad}$ channel acceptance. Emittances in both xx' phase space (top) and yy' phase space (bottom) are shown. Currents recorded by FC is $43 \text{ e}\mu\text{A}$. All ellipses enclosed 100% of the beam.

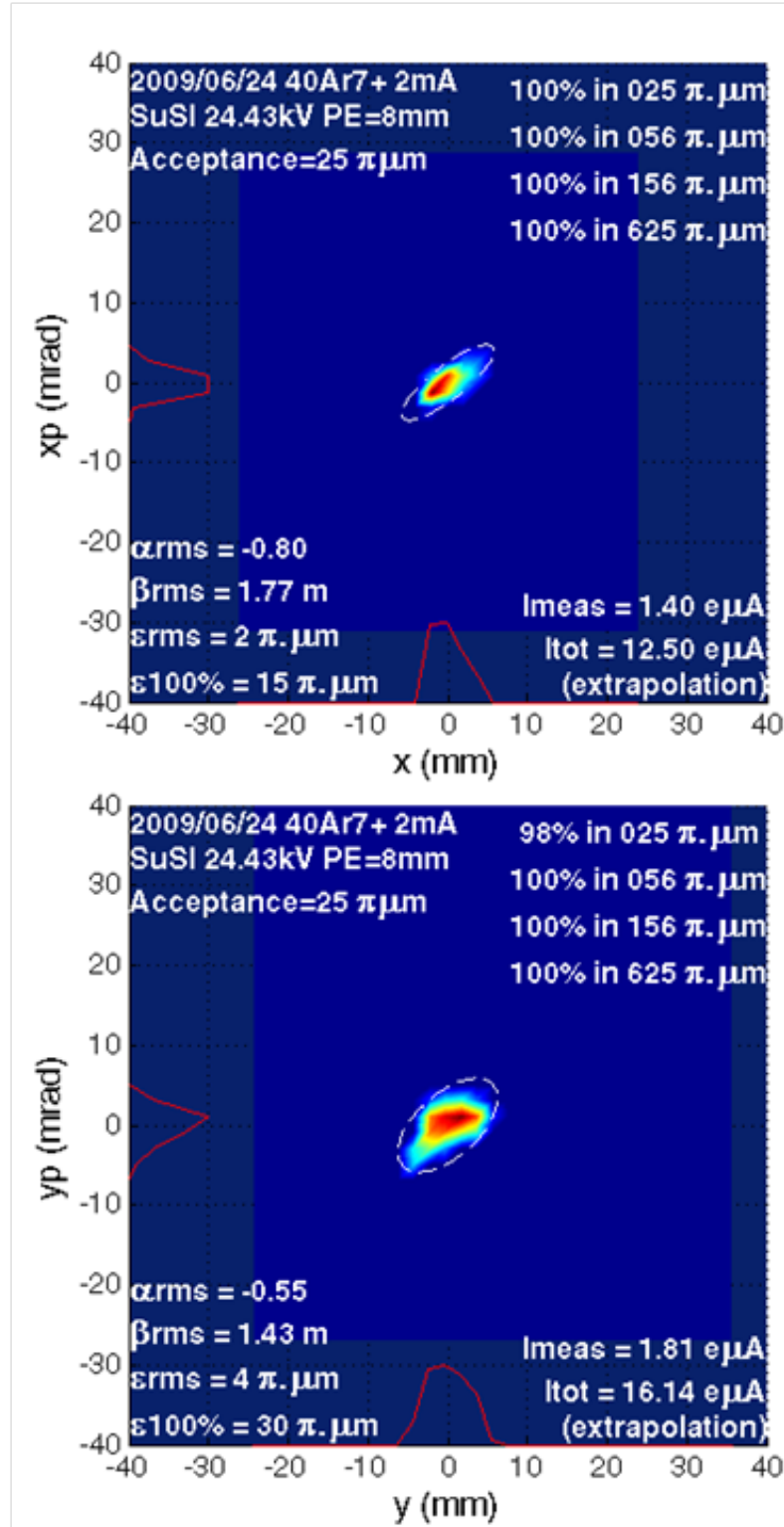


Figure 4.24: Emittances of the $^{40}\text{Ar}^{7+}$ beam measured with $25 \pi \cdot \text{mm} \cdot \text{mrad}$ channel acceptance. Emittances in both xx' phase space (top) and yy' phase space (bottom) are shown. Currents recorded by FC is $17 \text{ e}\mu\text{A}$. All ellipses enclosed 100% of the beam.

06/26/2009 SuSI $^{40}\text{Ar}^{7+}$ 24.43 kV
 PE=8mm DrainCurrent 2mA

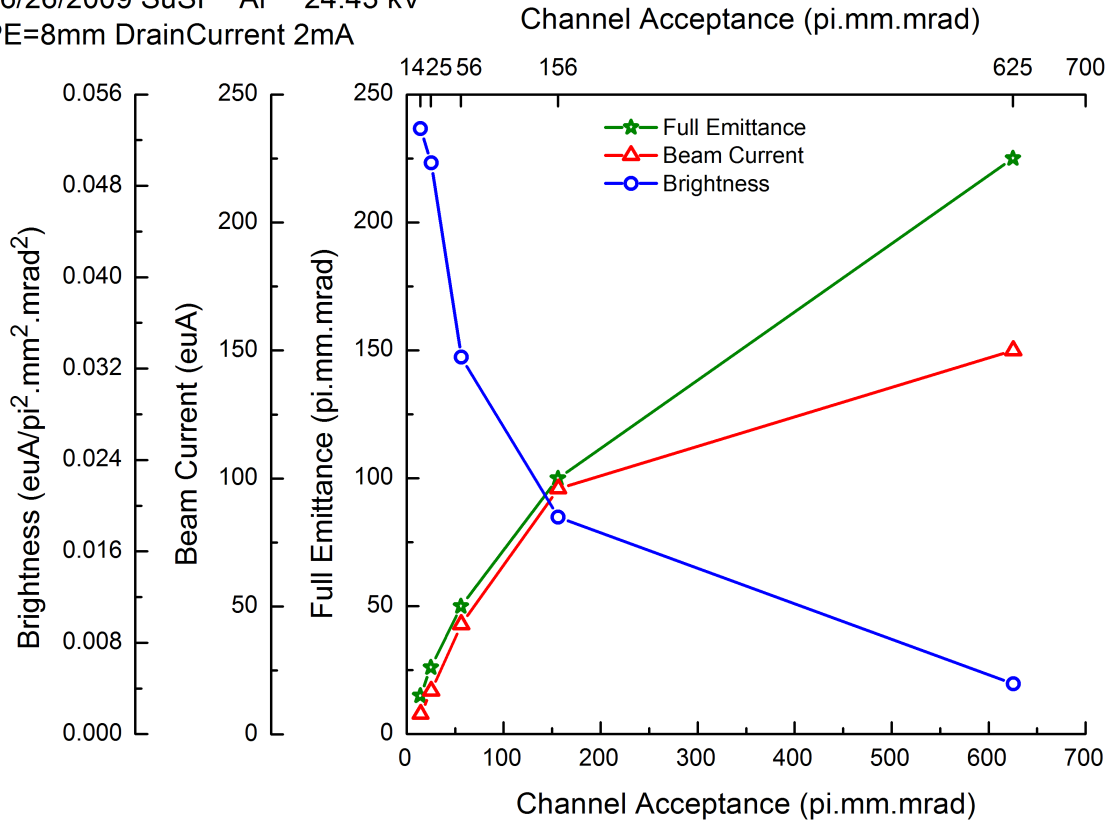


Figure 4.25: Beam brightness (blue) of $^{40}\text{Ar}^{7+}$ at the end of the collimation channel with different channel acceptances. Beam current (red) measured at the end of channel and beam full emittances (green) are shown as well for comparison. Beam full emittances were calculated from emittances in xx' and yy' phase spaces. It can be seen that when channel acceptance decreases, beam current and emittance both decrease, while beam brightness increases. This clearly demonstrates the effective collimation capability of the channel.

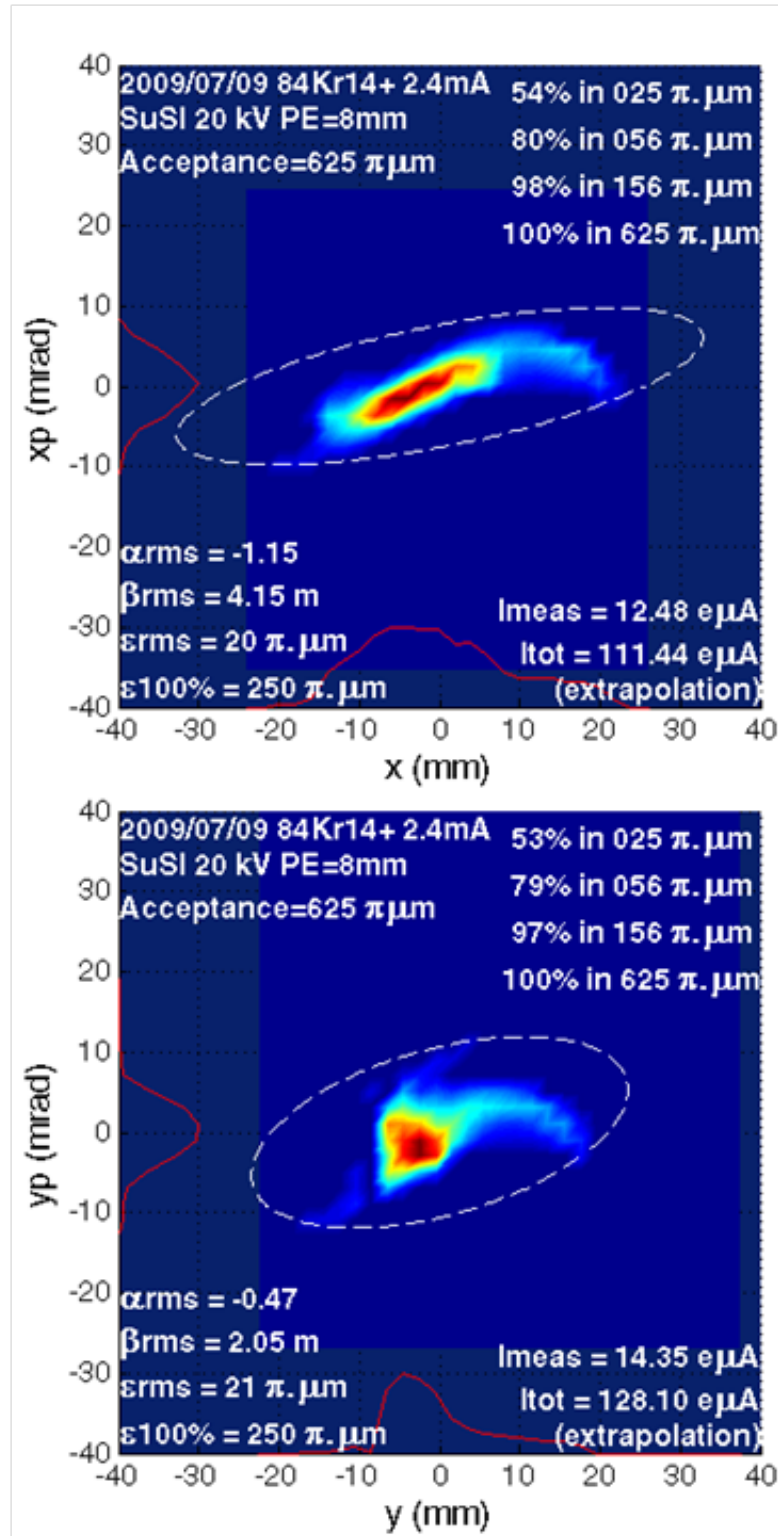


Figure 4.26: Emittances of the $^{84}\text{Kr}^{14+}$ beam measured with $625 \pi \cdot \text{mm} \cdot \text{mrad}$ channel acceptance. Emittances in both xx' phase space (top) and yy' phase space (bottom) are shown. Current recorded by FC is $138 \text{ e} \mu\text{A}$. All ellipses enclosed 100% of the beam.

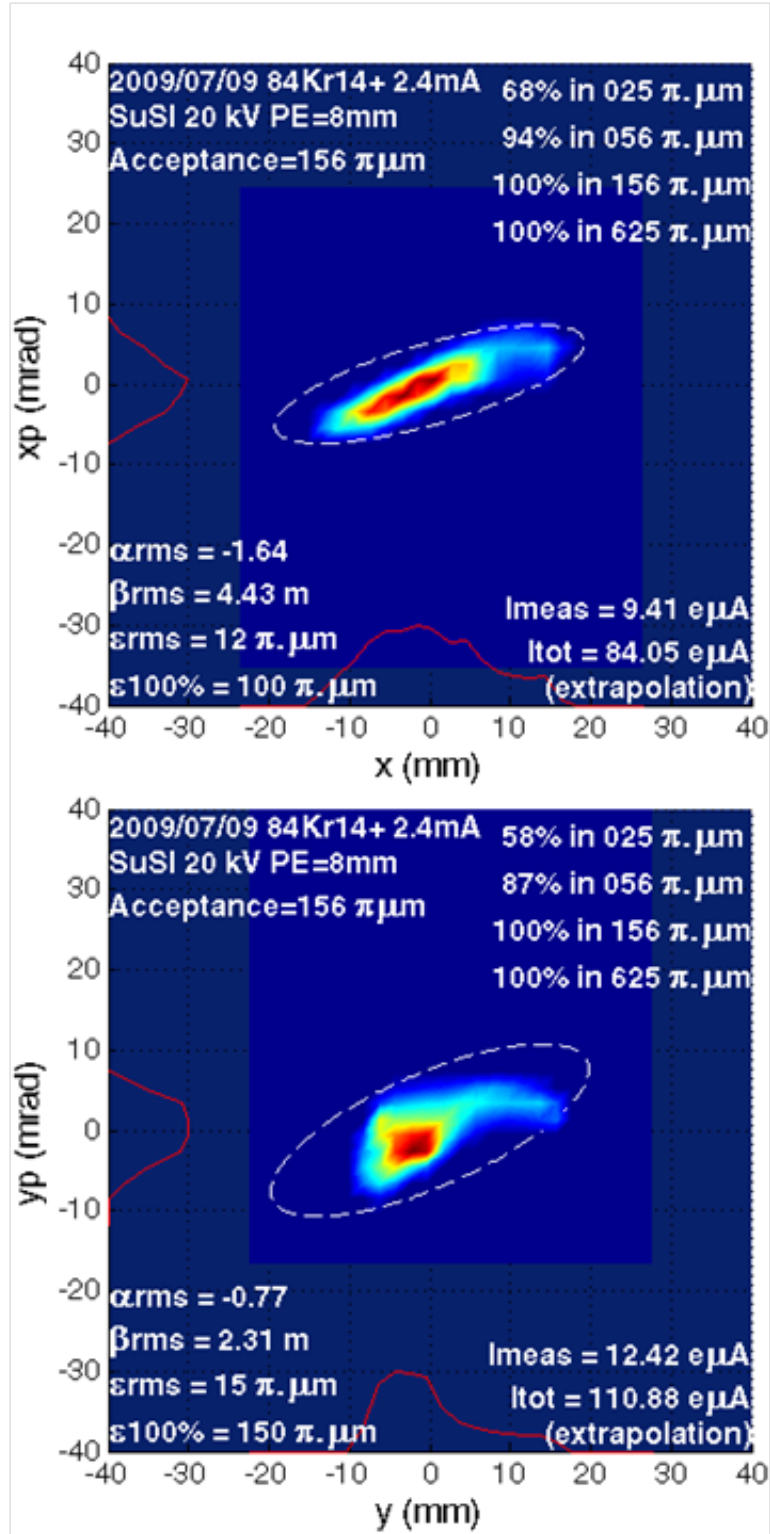


Figure 4.27: Emittances of the $^{84}\text{Kr}^{14+}$ beam measured with 156 π -mm-mrad channel acceptance. Emittances in both xx' phase space (top) and yy' phase space (bottom) are shown. Current recorded by FC is 100 $\text{e} \mu\text{A}$. All ellipses enclosed 100% of the beam.

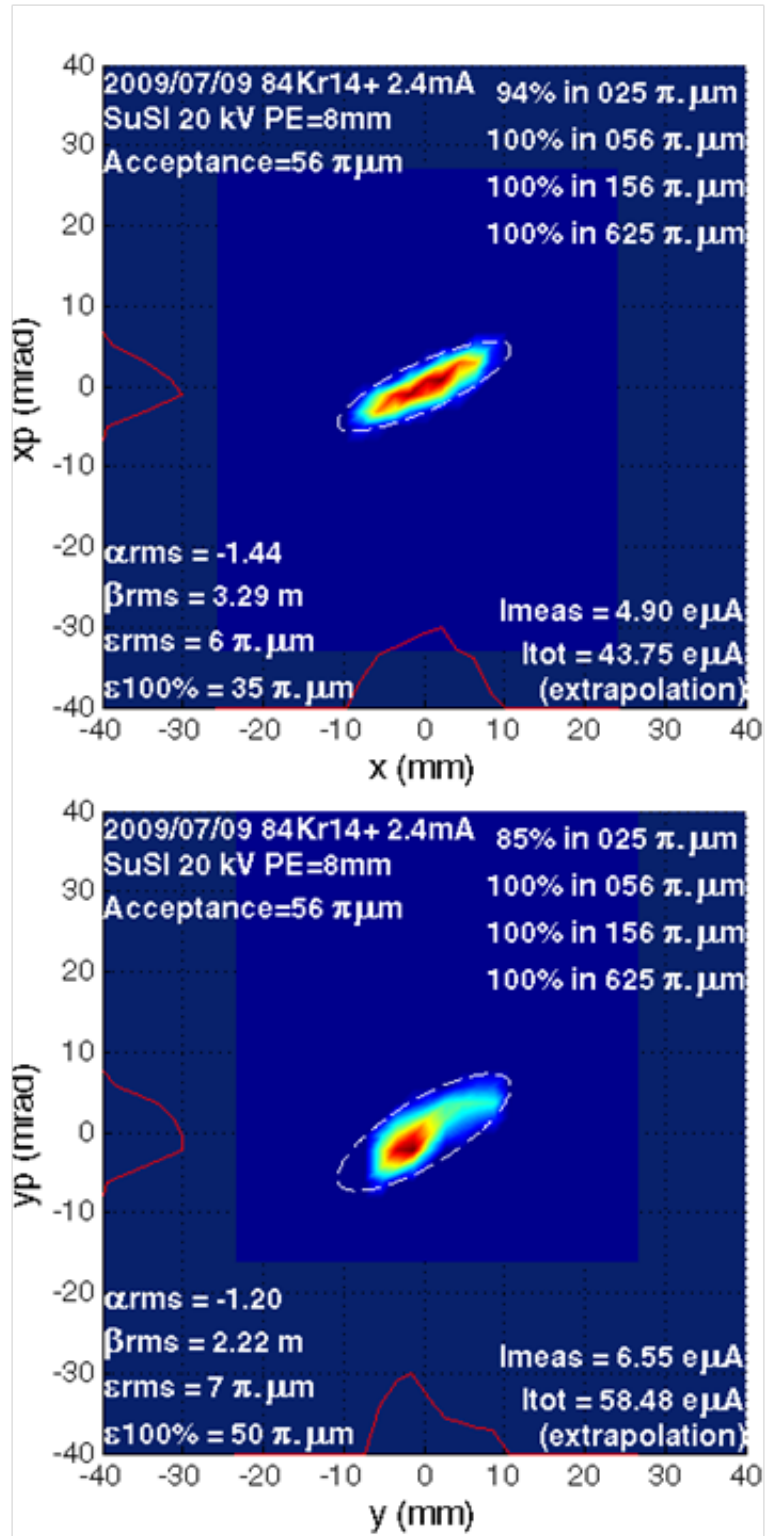


Figure 4.28: Emittances of the $^{84}\text{Kr}^{14+}$ beam measured with 56 $\pi \cdot \text{mm} \cdot \text{mrad}$ channel acceptance. Emittances in both xx' phase space (top) and yy' phase space (bottom) are shown. Current recorded by FC is 55 $\text{e}\mu\text{A}$. All ellipses enclosed 100% of the beam.

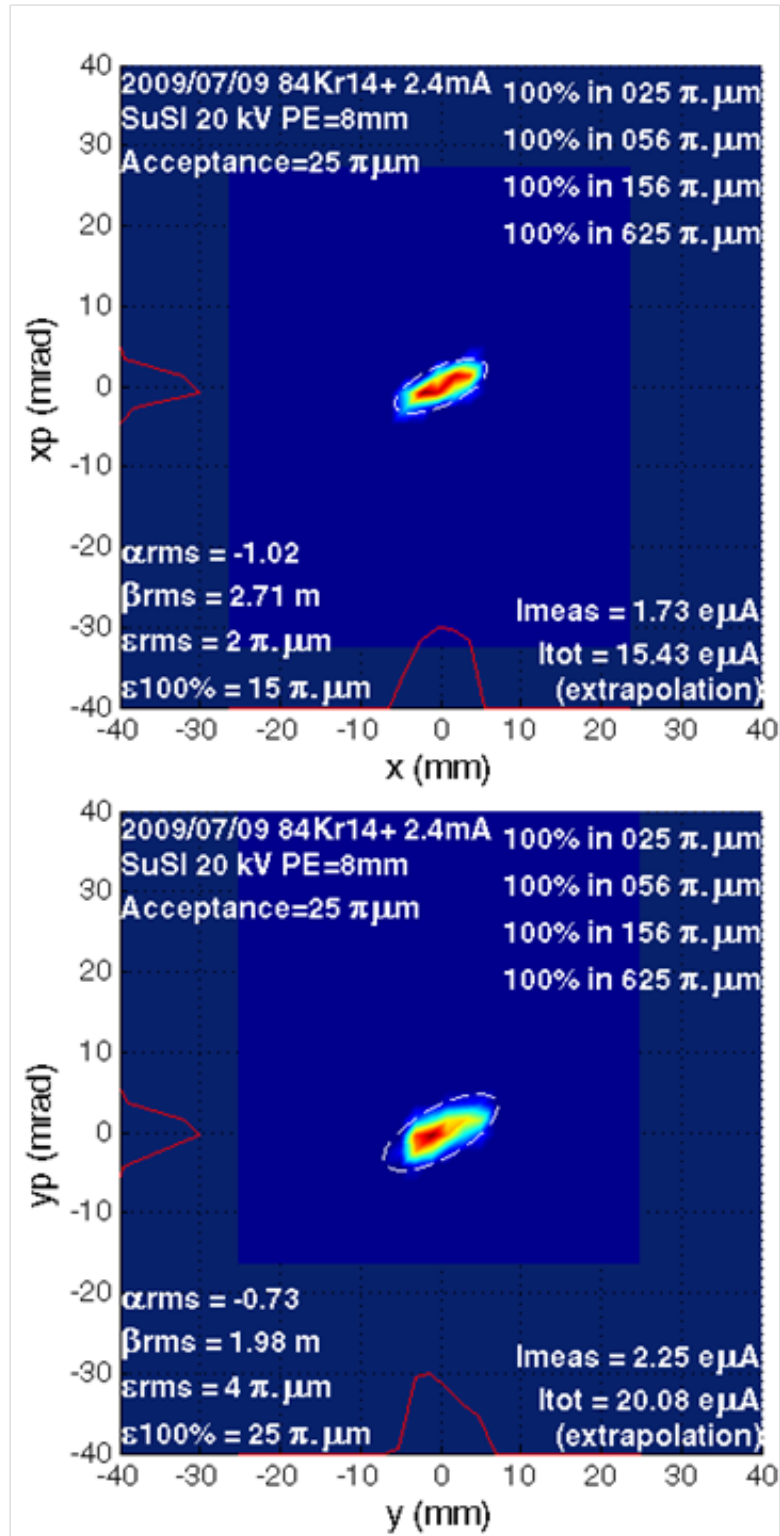


Figure 4.29: Emittances of the $^{84}\text{Kr}^{14+}$ beam measured with $25 \pi \cdot \text{mm} \cdot \text{mrad}$ channel acceptance. Emittances in both xx' phase space (top) and yy' phase space (bottom) are shown. Current recorded by FC is $19 \text{ e}\mu\text{A}$. All ellipses enclosed 100% of the beam.

From the plot, it can be noticed that when channel acceptance decreases, beam current and emittance both decreased, while beam brightness increased. This clearly demonstrates the effective collimation capability of the channel, again.

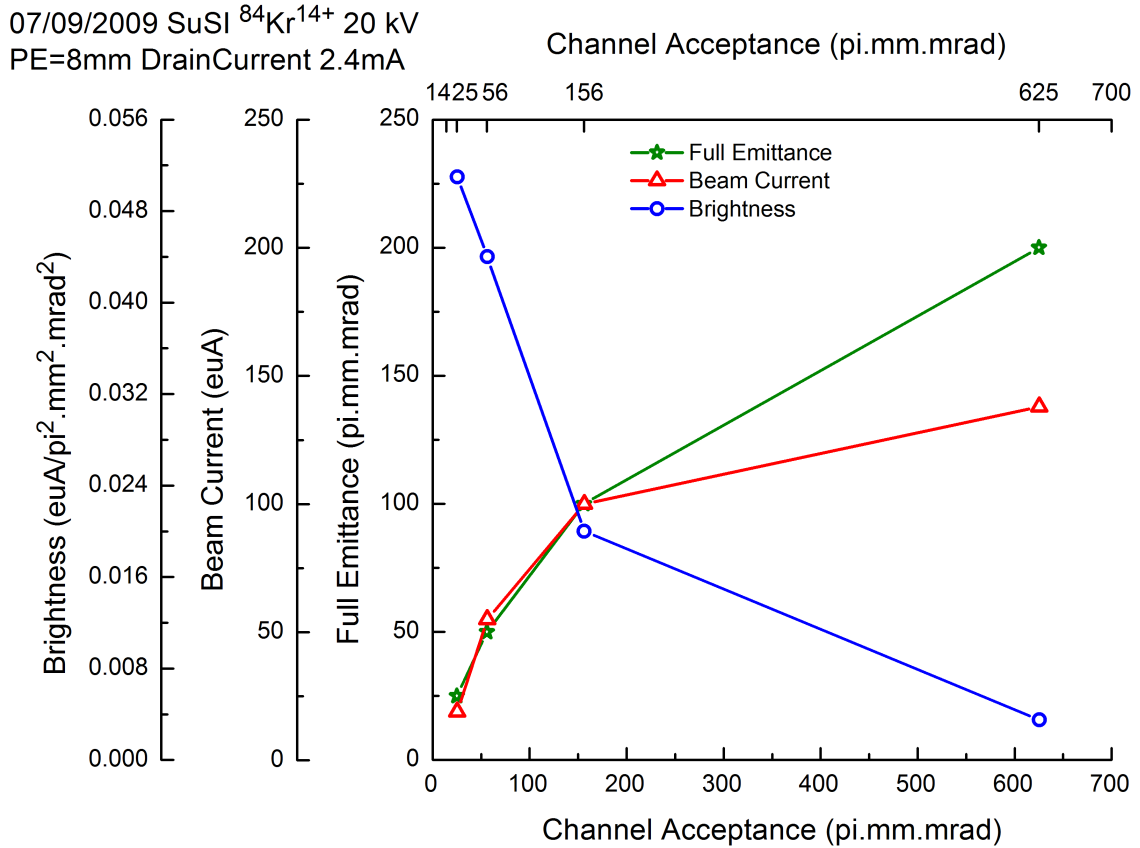


Figure 4.30: Beam brightness (blue) of $^{84}\text{Kr}^{14+}$ at the end of the collimation channel with different channel acceptances. Beam current (red) measured at the end of channel and beam full emittances (green) are shown as well for comparison. Beam full emittances were calculated from emittances in xx' and yy' phase spaces. It can be seen that when channel acceptance decreases, beam current and emittance both decrease, while beam brightness increase. This clearly demonstrates the effective collimation capability of the channel.

To show the effectiveness of the collimation process for a poor quality beam, the emittances were measured with the $^{84}\text{Kr}^{10+}$ beam which was more distorted in xx' and yy' phase spaces by space charge effects from beams with higher Q/A. The measured emittances along with the current at the end of the channel and the channel

acceptances are shown in Figures 4.31 and 4.32. The distortion in phase space of the $^{84}\text{Kr}^{10+}$ beam is shown with a channel acceptance at $625 \pi \cdot \text{mm} \cdot \text{mrad}$; however, the beam emittances after collimation with the channel acceptance set to $56 \pi \cdot \text{mm} \cdot \text{mrad}$ became similar to the ones from $^{84}\text{Kr}^{14+}$ beam. Thus, the capability of effective collimation even for a more distorted beam is clearly illustrated.

4.3.5 Emittance Collimation Channel For ECR Tuning

Motivation

The collimation channel can also be used to tune the ECR source itself and help increase the beam brightness. Before the collimation channel was designed, operators tended to tune the source by optimizing the current on a downstream faraday cup, without much information about the beam emittance of each tune before doing the time consuming emittance scan.

Now, with the collimation channel, the operators are assured that the emittance at the end of the channel is constrained to a certain level depending on the aperture settings. They have the freedom to change source parameters without worrying about the beam quality at the end. Also, studies of the effect of some ECR parameters on beam brightness can be conducted effectively using the collimation channel.

Example

When commissioning the collimation channel, we did an experiment to measure the current at the faraday cup at the end of the channel with different positions of the injection baffle of the ECR plasma chamber. The source was running a $^{40}\text{Ar}^{7+}$ beam with 24 kV ECR extraction voltage. All the apertures were set at 15 mm openings, corresponding to a $56 \pi \cdot \text{mm} \cdot \text{mrad}$ channel acceptance. The current was optimized when the baffle was at -40 mm. We then scanned the baffle position from 50 mm

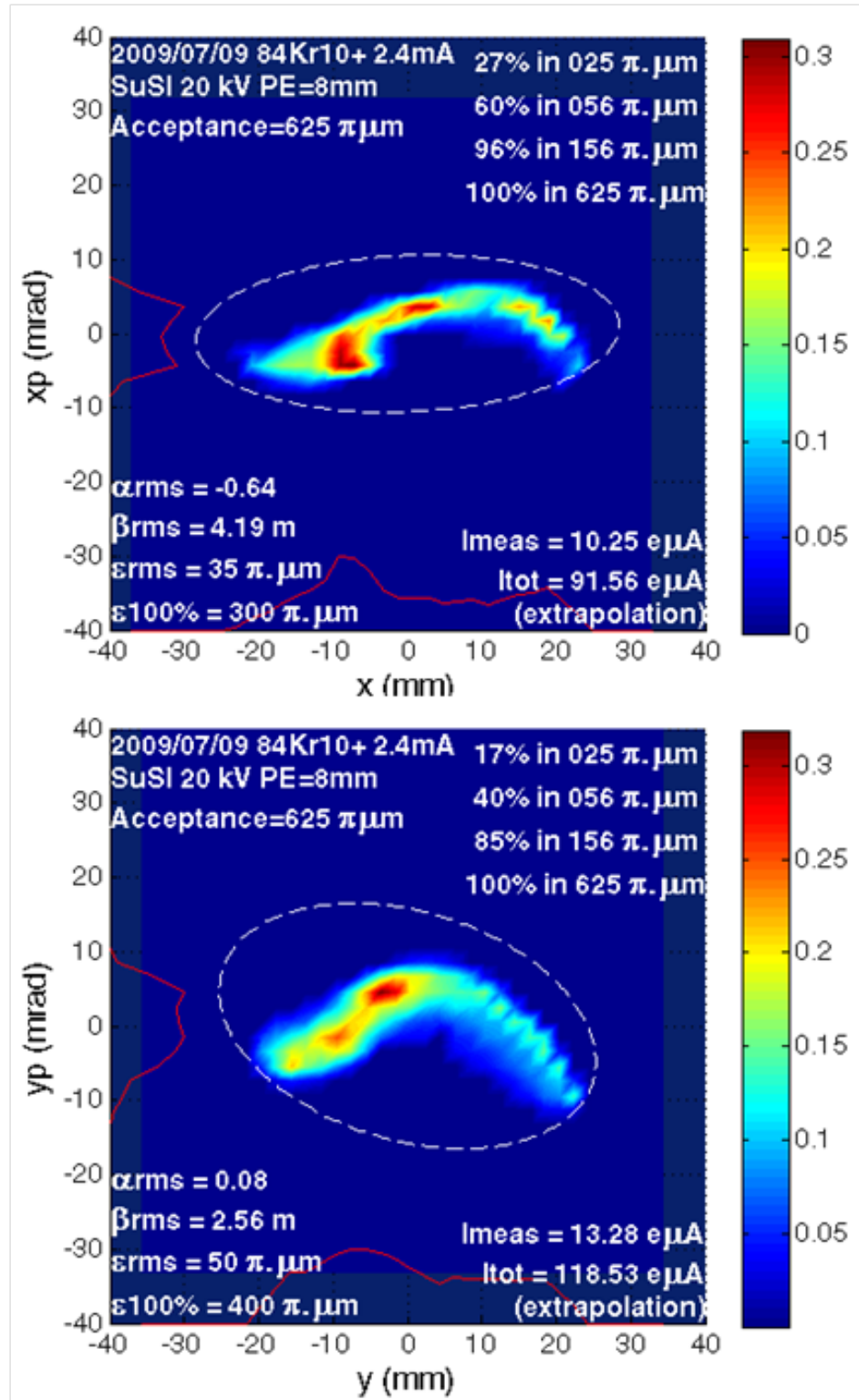


Figure 4.31: Emittances of the $^{84}\text{Kr}^{10+}$ beam measured with $625 \pi\text{-mm}\cdot\text{mrad}$ channel acceptance. Emittances in both xx' phase space (top) and yy' phase space (bottom) are shown. Current recorded by FC is $100 \text{ e}\mu\text{A}$. All ellipses enclosed 100% of the beam.

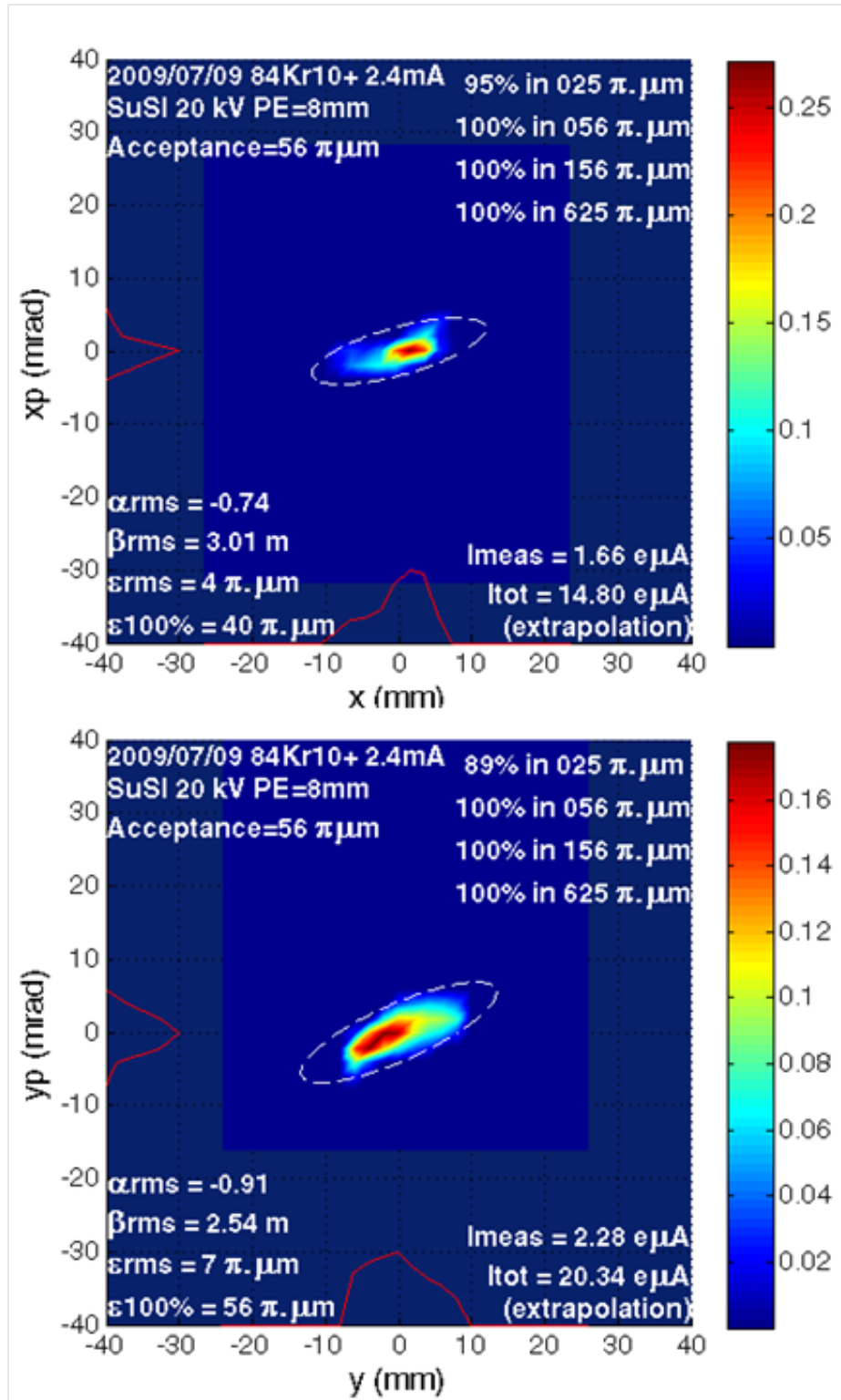


Figure 4.32: Emittances of the $^{84}\text{Kr}^{10+}$ beam measured with 56 π ·mm·mrad channel acceptance. Emittances in both xx' phase space (top) and yy' phase space (bottom) are shown. Current recorded by FC is 18 e μ A. All ellipses enclosed 100% of the beam.

to -50 mm and measured the current at the end of channel. The result is shown in Figure 4.33, and notches can be observed at various baffle positions. Further research will be initiated to investigate the effect of various ECR parameters, such as baffle positions, on beam brightness.

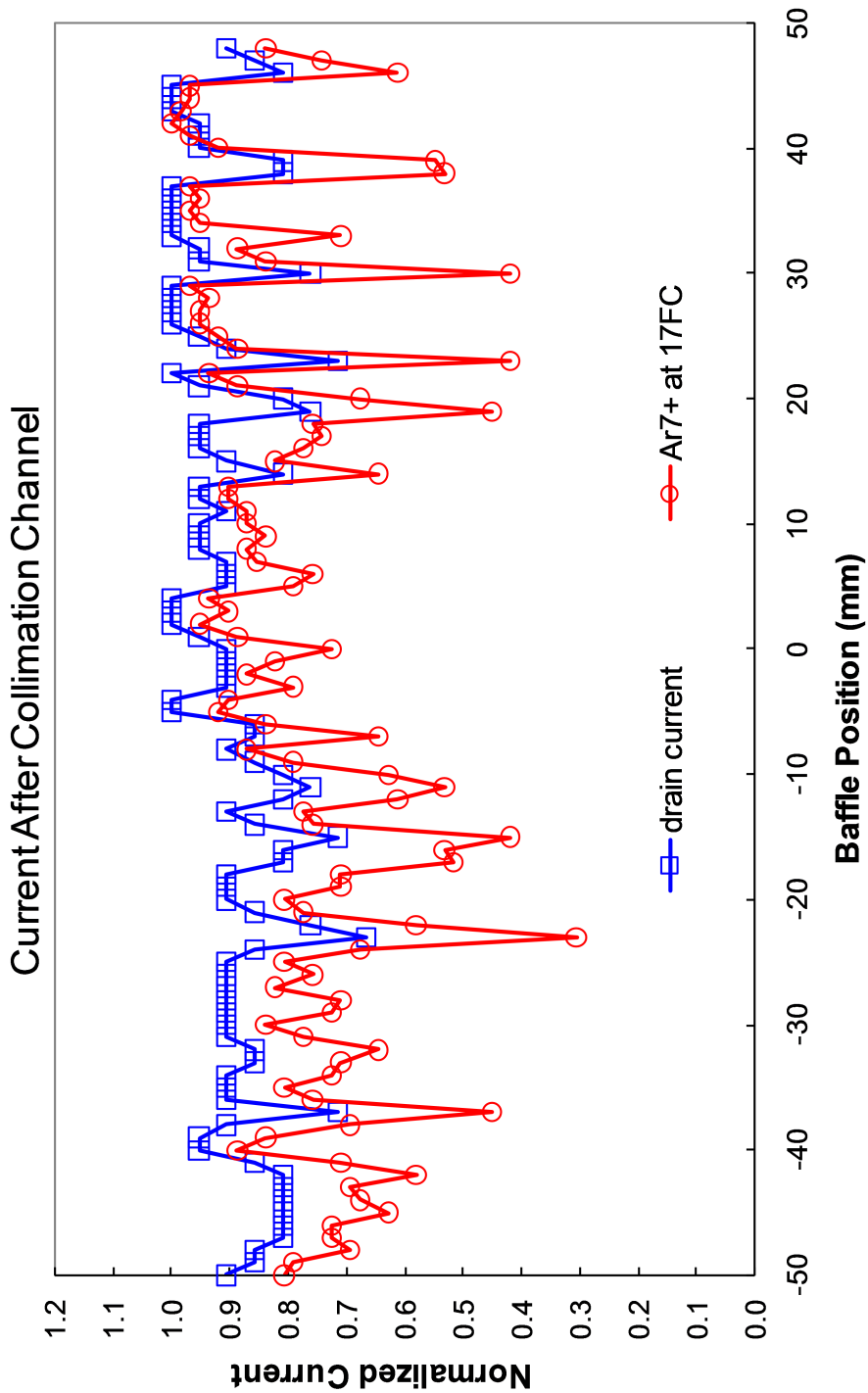


Figure 4.33: Measurement of current at end of collimation with different baffle positions. Drain current (blue) and $^{40}\text{Ar}^{7+}$ beam current (red) are both shown for comparison. The current at the end of the channel was first optimized when baffle was at -40 mm position, and then measured when baffle changed from 50 mm to -50 mm.

Chapter 5

CONCLUSION

The goal of this thesis was to design an extraction beam line that connects our newly designed superconducting ECR ion source SuSI to the CCF injection beam line. In addition to the increase of beam current provided by SuSI, a multistage collimation scheme was used to improve the quality of the beam injected into the CCF, particularly to improve the extraction efficiencies in the K500 and K1200 cyclotrons where large losses on the deflectors are an issue. This ultimately increases the extraction efficiency of the K500 cyclotron. The collimation channel was designed, installed and commissioned. The channel was able to meet the design goals.

The collimation channel uses four collimation stages and three solenoids in between to rotate the beam transversely in phase spaces. The design of the channel was constrained by space considerations in the CCF ECR area and a solution using three solenoids was chosen because it offered a compact layout and could reuse three solenoids already available at NSCL. Nonetheless, a design with an even number of solenoids (e.g. four) would have been better since the geometric rotation induced by the solenoid optics can conveniently be canceled by reversing the field orientation of consecutive solenoids.

Beam simulations have shown that the proposed design can efficiently collimate

beams from SuSI under various scenarios (e.g. different beam input parameters). We have commissioned the collimation channel with SuSI in the test area prior to its installation in the CCF ECR area. Experiments with Krypton and Argon beams have confirmed the effective collimation capability observed in beam simulation.

For beams that are mismatched to the channel, the collimation efficiency is not at its optimum. To recuperate the efficiency, a mitigation strategy is proposed to adapt the channel apertures to the beam size through the channel.

There is still much work that can be done in the future to improve the performance of the channel. As the middle two apertures are circular openings with limited size range, a possible upgrade would be to replace those apertures with two 4-Jaw slit systems that offer tunable aperture sizes to increase the flexibility of altering the channel acceptance. A 4D emittance scan is also necessary in the future to fully understand the behavior of the extracted beam from the SuSI ECR. In addition, further research can be done to develop and test other mitigation strategies in order to recover the collimation efficiency for mismatched beams. Also, source tuning should be investigated to better match the beam to the channel.

The experience gained in this thesis about the design and operation of the transverse emittance collimation channel could also benefit the FRIB project, where a similar transverse collimation system is part of the front end design and where a longitudinal emittance collimation scheme is proposed to meet the requirement of 400 kW beam power[32]. In that scheme, the same transverse collimation channel design could be applied between two emittance exchangers which exchange transverse and longitudinal emittances.

BIBLIOGRAPHY

- [1] H. W. Zhao, L. T. Sun, X. Z. Zhang, X. H. Guo, Y. Cao, W. Lu, Z. M. Zhang, P. Yuan, M. T. Song, H. Y. Zhao, T. Jin, Y. Shang, W. L. Zhan, B. W. Wei, and D. Z. Xie, *Rev. Sci. Instrum.* 79(2), 02A315 (2008).
- [2] S. Snyder, "Study and Redesign of the NSCL K500 Injection, Central Region and Phase Selection Systems", PhD Dissertation, Department of Physics and Astronomy, Michigan State University, East Lansing, Michigan, 1995.
- [3] H. G. Blosser, *Nuclear Science, IEEE Transactions on* 26(2), 2040-2047 (1979).
- [4] J. A. Nolen, T. A. Antaya, T. S. Kuo, F. Marti, B. M. Sherrill, A. G. Zeller, and H. G. Blosser, "Commissioning Experience With the NSCL K1200 Superconducting Cyclotron", in *Proceedings of 12th International Conference on Cyclotrons and Their Applications*, May 8-12, 1989, Berlin, Germany.
- [5] P. Miller, F. Marti and D. Poe, "Commissioning of the Coupled Cyclotron Facility at Nscl". in *Proceedings of 19th Particle Accelerator Conference (PAC01)*, June 18-22, 2001, Chicago, Illinois, USA.
- [6] M. Doleans, S. Chouhan, D. Cole, G. Machicoane, F. Marti, P. Miller, J. Moskaliuk, M. Steiner, J. Stetson, X. Wu, P. Zavodszky, A. Zeller and Q. Zhao, "Optics Improvements of the K500 Axial Injection Line", in *Proceedings of 8th International Conference on Cyclotrons and Their Applications*, September 30-October 5, 2007, Giardini Naxos, Messina, Italy.
- [7] <http://www.nsl.msui.edu/exp/propexp/beamlist>
- [8] O. Kester, D. Bazin, C. Benatti and J. Bierwagen, "The Msu/Nscl Re-Accelerator Rea3". in *Proceedings of 14th International Conference on RF Superconductivity (SRF2009)*, September 20-25, 2009, Berlin, Germany.
- [9] R. C. Yock, G. Bollen, C. Compton, A. C. Crawford, M. Doleans, T. Glasmacher, W. Hartung, F. Marti, J. Popielarski, J. J. Vincent, J. Wlodarczak, X. Wu, A. Zeller and Q. Zhao, "Frib: A New Accelerator Facility for the Production of

- Rare Isotope Beams". in Proceedings of 14th International Conference on RF Superconductivity (SRF2009), September 20-25, 2009, Berlin, Germany.
- [10] F. J. Currell. The Physics of Multiply and Highly Charged Ions, Kluwer Academic Publishers, Norwell, Massachusetts, 2003.
 - [11] G. Machicoane, "Beam Experiments and Measurements at the NSCL - Ion Sources", U.S. Particle Accelerator School, lecture notes, East Lansing, Michigan, June 4-15, 2007.
 - [12] G. Machicoane, D. Cole, J. Ottarson, J. Stetson and P. Zavodszky, Rev. Sci. Instrum 77(3), 03A322 (2006).
 - [13] E. B. Holzer, "Particle counting in Hyperellipsoids Figure of Merit for the Cooling experiment", NFWG meeting, February 20, 2002.
 - [14] E. D. Courant and H. S. Snyder, Annals of Physics 281(1-2), 360-408 (2000).
 - [15] M. Doleans, "Beam Experiments and Measurements at the NSCL - Beam Dynamics", U.S. Particle Accelerator School, lecture notes, East Lansing, Michigan, June 4-15, 2007.
 - [16] N. Pichoff, "Transverse Beam Dynamics in Accelerators", Joint University Accelerator School, lecture notes, East Lansing, Michigan, January, 2004.
 - [17] P. M. Lapostolle, Nuclear Science, IEEE Transactions on 18(3), 1101-1104.
 - [18] F. J. Sacherer, Nuclear Science, IEEE Transactions on 18(3), 1105-1107.
 - [19] D. Hitz, A. Girard, G. Melin, S. Gammino, G. Ciavola and L. Celona, Rev. Sci. Instrum. 73(2), 509-512 (2002).
 - [20] P. A. Zavodszky, B. Arend, D. Cole, J. DeKamp, G. Machicoane, F. Marti, P. Miller and J. Moskalik, "Design, Construction and Commissioning of the Susi Ecr ". in Proceedings of 22nd Particle Accelerator Conference (PAC07), June 25-29, 2007, Albuquerque, New Mexico, USA.
 - [21] P. A. Zavodszky, B. Arend, D. Cole, J. DeKamp, G. Machicoane, F. Marti, P. Miller, J. Moskalik, J. Ottarson, J. Vincent and A. Zeller, Nucl. Instr. Meth. B 241(1-4), 959-964 (2005).
 - [22] P. A. Zavodszky, B. Arend, D. Cole, J. DeKamp, G. Machicoane, F. Marti, P. Miller, J. Moskalik, J. Ottarson, J. Vincent, A. Zeller and N. Y. Kazarinov, Rev. Sci. Instrum. 77(3), 03A334-334 (2006).
 - [23] Y. Higurashi, T. Nakagawa, M. Kidera, T. Aihara, M. Kase and Y. Yano, Rev. Sci. Instrum 73(2), 598-600 (2002).

- [24] G. Machicoane, C. Benatti, D. Cole, M. Doleans, O. Kester, F. Marti, X. Wu, P. A. Zavodszky and C. Zhang, "Performance Investigation of the Nscl 18 Ghz Superconducting Ecr Ion Source Susi". in Proceedings of 23rd Particle Accelerator Conference (PAC09), May 4-8, 2009, Vancouver, Canada.
- [25] M.A. Leitner, D.C. Wutte and C. M. Lyneis, "Design of the Extraction System of the Superconducting Ecr Ion Source Venus". in Proceedings of 19th Particle Accelerator Conference (PAC01), June 18-22, 2001, Chicago, Illinois, USA.
- [26] D. Wutte, M. A. Leitner and C. M. Lyneis, *Physica Scripta* 2001(T92), 247 (2001).
- [27] S. Kondrashev, A. Barcikowski, B. Mustapha, P. N. Ostroumov and N. Vinogradov, et al., *Nucl. Instr. Meth. A* 606(3), 296-304 (2009).
- [28] N. Y. Kazarinov, *Rev. Sci. Instrum* 75(5), 1665-1666 (2004).
- [29] M.A. Leitner, "Emittance Scanner Specification for the 88 Injection Beamlines", Technical Note, LBNL.
- [30] K. Crandall and D. Rusthoi, "TRACE 3-D Documentation", Third Edition, LA-UR-97-886, 1997.
- [31] J.H. Billen and L.M. Young, "SUPERFISH/Poisson Group Of Codes", Report LA-UR-96-1834, 1996.
- [32] M. Doleans, "Emittance Collimation Scheme for Ion Beams", Nuclear Seminar, Michigan State University, East Lansing, Michigan, January 20, 2010.